Colloidal synthesis and characterizations of metal, metal- oxide, and semiconductor nanoparticles by inductive heating method

by

Pratikshya Sharma

B.Sc., Tribhuvan University, Nepal, 2014
M.Sc., Tribhuvan University, Nepal, 2017

AN ABSTRACT OF A DISSERTATION

Submitted in partial fulfillment of the requirements for the degree

DOCTOR OF PHILOSOPHY

Department of Chemistry
College of Arts and Sciences

KANSAS STATE UNIVERSITY
Manhattan, Kansas

2021

Abstract

The goal of this thesis is to develop a faster, safer, and industrial-level scale-up methodology for the synthesis of diverse nanomaterials applying the inductive heating methodology. This thesis discusses the size control magnetic inductive heating synthesis of iron, iron- oxide, manganese, manganese/iron alloys, and germanium nanoparticles (NPs) in different chapters. Background in the magnetic heating methodology and how it can be used for nanomaterial synthesis is discussed in Chapter 2. Chapter 3 describes the synthesis and characterization of colloidal insulating iron-oxide NPs. Fe_2O_3 and Fe_3O_4 NPs were prepared by inductive heating. Their morphological and magnetic properties were studied in detail. The effect of different solvents and heating times on the size of NPs was explored. Furthermore, this chapter discusses how the inductive heating methodology can be utilized for the use of solid precursors to prepare monodispersed, phase pure γ- Fe_2O_3 NPs. Chapter 4 is aimed to describe the synthesis of air-stable metallic iron NPs with their size tuning. TEM, HRTEM, PXRD, and elemental analysis were carried out to confirm the formation of iron NPs and their particle size distributions. SQUID was used to investigate the magnetic properties of thus synthesized NPs. Chapter 5 focuses on achieving greater control over the size distribution in the solution synthesis of semiconducting germanium NPs. The effect of concentration of precursor and heating time was explored. This chapter will also discuss the possible defects present in as-synthesized NPs. Various spectroscopic characterizations such as transient absorption and UV-Vis-NIR were performed to identify the quality of crystals. Finally, Chapter 6 describes the use of the inductive heating methodology for the synthesis of manganese oxide and iron-manganese oxide alloy nanoparticles, a potential material for fossil-free ammonia synthesis by step catalysis. One-pot inductive heating-assisted method promises a scalable and low-cost production of highly crystalline NPs by overcoming the traditional disadvantages of long reaction times, high temperature and pressure, complicated precursor preparation, and exhaustive post-synthetic purification steps.

Colloidal synthesis and characterizations of metal, metal- oxide, and semiconductor nanoparticles by inductive heating

by

Pratikshya Sharma

B.Sc., Tribhuvan University, Nepal, 2014
M.Sc., Tribhuvan University, Nepal, 2017

A DISSERTATION

Submitted in partial fulfillment of the requirements for the degree

DOCTOR OF PHILOSOPHY

Department of Chemistry
College of Arts and Sciences

KANSAS STATE UNIVERSITY
Manhattan, Kansas

2021

Approved by:

Major Professor
Prof. Viktor Chikan

Copyright

Abstract

The goal of this thesis is to develop a faster, safer, and industrial-level scale-up methodology for the synthesis of diverse nanomaterials applying the inductive heating methodology. This thesis discusses the size control magnetic inductive heating synthesis of iron, iron- oxide, manganese, manganese/iron alloys, and germanium nanoparticles (NPs) in different chapters. Background in the magnetic heating methodology and how it can be used for nanomaterial synthesis is discussed in Chapter 2. Chapter 3 describes the synthesis and characterization of colloidal insulating iron-oxide NPs. Fe_2O_3 and Fe_3O_4 NPs were prepared by inductive heating. Their morphological and magnetic properties were studied in detail. The effect of different solvents and heating times on the size of NPs was explored. Furthermore, this chapter discusses how the inductive heating methodology can be utilized for the use of solid precursors to prepare monodispersed, phase pure γ- Fe_2O_3 NPs. Chapter 4 is aimed to describe the synthesis of air-stable metallic iron NPs with their size tuning. TEM, HRTEM, PXRD, and elemental analysis were carried out to confirm the formation of iron NPs and their particle size distributions. SQUID was used to investigate the magnetic properties of thus synthesized NPs. Chapter 5 focuses on achieving greater control over the size distribution in the solution synthesis of semiconducting germanium NPs. The effect of concentration of precursor and heating time was explored. This chapter will also discuss the possible defects present in as-synthesized NPs. Various spectroscopic characterizations such as transient absorption and UV-Vis-NIR were performed to identify the quality of crystals. Finally, Chapter 6 describes the use of the inductive heating methodology for the synthesis of manganese oxide and iron-manganese oxide alloy nanoparticles, a potential material for fossil-free ammonia synthesis by step catalysis. One-pot IH-assisted method promises a scalable and low-cost production of highly crystalline NPs by overcoming the traditional disadvantages of long reaction times, high temperature and pressure, complicated precursor preparation, and exhaustive post-synthetic purification steps.

Table of Contents

Table of Contents vi

List of Figures ix

List of Tables xiii

Acknowledgments xiv

Dedication xvi

Chapter 1 - Introduction 1

- 1.1 Background 1
    - 1.1.1 Top-down method 2
    - 1.1.2 Bottom-up method 3
- 1.2 Colloidal synthesis of NPs 5
- 1.3 Hot-injection method 14
- 1.4 Limitations of existing methods and motivation to this work 16
- 1.5 Goals of the dissertation 19

Chapter 2 - Experimental techniques 20

- 2.1 Fundamentals of induction heating 20
    - 2.1.1 Faraday's law of electromagnetic induction 20
    - 2.1.2 Magnetic hysteresis 21
    - 2.1.3 Penetration depth or skin effect 22
- 2.2 Experimental set-up and heating mechanism 24
- 2.3 Unique characteristic of IH and its possibility in the scale-up synthesis 26

Chapter 3 - Size controlled synthesis of iron oxide nanoparticles by inductive heating 32

- Abstract 32
- 3.1 Introduction 33
- 3.2 Materials and methods 36
    - 3.2.1 Chemicals 36
    - 3.2.2 Method of synthesis 36
    - 3.2.3 Characterization of IONPs 38
- 3.3 Results and discussions 39
    - 3.3.1 Synthesis of IONP from $Fe(CO)_5$ in oleylamine and trioctylamine 40

3.3.2 Comparison of magnetic properties of IONPs 45
3.3.3 Synthesis of γ-Fe_2O_3 from acetylferrocene 46
3.4 Conclusion 52
Chapter 4 - Colloidal synthesis and characterization of air-stable iron nanoparticles 53
Abstract 53
4.1 Introduction 54
4.2 Materials and methods 56
4.2.1 Chemicals 56
4.2.2 Method of synthesis 56
4.2.3 Characterization of Fe NPs 57
4.3 Result and discussions 57
4.4 Conclusions 61
Chapter 5- Colloidal synthesis of air-stable germanium nanoparticles with tunable sizes using the inductive heater 62
Abstract 62
5.1 Introduction 62
5.2 Materials and methods 65
5.2.1 Chemicals 65
5.2.2 Inductive heating synthesis 65
5.2.3 Characterization 66
5.3 Result and discussion 67
5.3.1 Effect of GeI_2 concentration on size of NPs 67
5.3.2 Effect of GeI_2/ GeI_4 concentration on size of NPs 68
5.3.3 Effect of reaction time on the size of NPs 69
5.3.4 Spectroscopic characterization of NPs 69
5.4 Conclusions 71
Chapter 6- Synthesis of manganese oxide and iron/manganese alloy nanoparticles by magnetic heating 72
Abstract 72
6.1 Introduction 72
6.2 Materials and methods 74

6.3 Result and discussion 75
Chapter 7- Summary and outlook 79
References 81
Appendix A - Supporting information from Chapter 3 94
Appendix B - Supporting information from Chapter 4 95
Appendix C - Supporting information from Chapter 5 96
Appendix D - Supporting information from Chapter 6 97
Appendix E - List of publications 98

List of Figures

Figure 1.1 Top-down and Bottom-up synthesis of NPs 3

Figure 1.2 Dependence of nucleation and growth rate of monomer supersaturation S (S = 1 is the solubility of the monomer at any given temperature)[38]. In this example, a higher supersaturation environment for rapid the formation of new nuclei via homogeneous nucleation. Once monomer concentration decreases, slow growth can take over the process, which can lead to size focusing under diffusion control reaction conditions**.** 8

Figure 1.3 Schematic of LaMer diagram indicating three different stages of nucleation and growth of NPs as discussed above. 11

Figure 1.4 (A) Growth rate vs NP radius for a single NP for K=1, **(B)** Temporal evolution of size distribution of NP ensemble during the Ostwald ripening under diffusion-controlled reaction (K= 10^{-3})... 12

Figure 1.5 Representation of the simple synthetic apparatus employed to prepare monodisperse NPs/QDS by HI method... 15

Figure 2.1 Schematics showing the illustration of Faraday's law of electromagnetic induction indicating the direction applied magnetic field, induced magnetic field, applied current, and induced current... 21

Figure 2.2 Magnetic hysteresis.[75] (A) Illustration of ferromagnetic domains at the varied magnetic field. (B) Illustration of hysteresis loop indicating the dependence of magnetic field strength with magnetic flux density. (C) Picture showing hysteresis effect in copper *vs* steel. 22

Figure 2.3 Skin Effect on a conductor. (A) Skin depth δ is the depth at which the current density is approximately 37% of the value at the surface. RF current doesn't stop at the dashed line but decreases logarithmically concerning depth in the conductor. (B) Graph showing the dependence of the skin depth with frequency. 23

Figure 2.4 Typical induction heating setup consisting of AC power supply, heat station, induction coil, and feedback system. 24

Figure 2.5 (A) Inductive heater used in this dissertation and (B) The reactor setup in the IH system. 26

Figure 2.6 A Comparison of heating rate by induction heating, microwave, and heating mantle 27

Figure 2.7 TEM images of IONPs produced by using 0.8M Fe $(CO)_5$, and oleylamine at reaction times 5 sec, by a different person (A) Sharma and (B) Holliger. C and D are the particle size distribution plots, respectively 28

Figure 2.8 Pictures of (A) a continuous reactor and (B) batch reactors used in IH setup at our laboratory. The larger reactor is designed to provide extra space for boiling solvent in case of longer heating times. 29

Figure 2.9 Illustration of continuous synthesis setup. 29

Figure 3.1 Inductive heating reactor filled with the precursor and the solvent (left), the same reactor after the reaction (middle), and magnetic IONPs after purification (right). 38

Figure 3.2 Transmission electron microscopy (TEM) images of IONPs produced using 0.8 M Fe $(CO)_5$ and OA at different reaction times (A) 5 s, (B) 7 s, (C) 10 s, and (D) 14 s (7 + 7 s). (E)–(H) are the particle size distribution plots, respectively 41

Figure 3.3 High-resolution TEM (HRTEM) images of IONPs produced using 0.8 M Fe $(CO)_5$ and OA at different reaction times (A) 7 s, (B) 10 s, and (C) 14 s (7 + 7 s), indicating (032), (117), and (022) lattice planes of γ-Fe_2O_3 nanoparticles, respectively 42

Figure 3.4 TEM images of IONPs produced using 3.35 M $Fe(CO)_5$ and OA at different reaction times (A) 5 s and (B) 10 s. (C) and (D) are the particle size distribution plots, respectively 42

Figure 3.5 TEM images of IONPs produced using 7.5 M $Fe(CO)_5$ and OA at different reaction times (A) 5 s and (B) 10 s. (C) and (D) are the particle size distribution plots, respectively 43

Figure 3.6 TEM images of IONPs produced using 0.8 M $Fe(CO)_5$ and TOA at different reaction times (A) 5 s, (B) 7 s, (C) 10 s, and (D) 14 s (7 + 7 s). (E)–(H) are the particle size distribution plots, respectively 44

Figure 3.7 HRTEM images of IONPs produced using 0.8 M $Fe(CO)_5$ and TOA at different reaction times (A) 7 s, (B) 10 s, and (C) 14 s (7 + 7 s), indicating (222), (025), and (026) lattice planes of γ-Fe_2O_3 nanoparticles, respectively. 45

Figure 3.8 Magnetization *vs* magnetic field plot for IONPs produced using 0.8 M (A) $Fe(CO)_5$ and OA (B); $Fe(CO)_5$ and TOA at 5, 7, 10, and 7 +7 s heating time. 46

Figure 3.9 TEM images of γ-Fe_2O_3 NPs produced by using 0.8 M acetylferrocene and OA at different reaction times (A) 5 s, (B) 7 s, (C) 10 s, and (D) 14 s. (E–H) are the particle size distribution plots, respectively. 47

Figure 3.10 HRTEM images of γ-Fe_2O_3 NPs produced by using 0.8 M acetylferrocene, and oleylamine at different reaction times (A) 5 s, (B) 7 s, (C) 10 s, and (D) 14 s. (A) indicates (222) lattice planes, (B) indicates (026), (222) lattice planes, (C) indicates (026) lattice planes, and (D) indicates (112), (222) lattice planes of γ-Fe_2O_3 NPs. 48

Figure 3.11 PXRD of γ-Fe_2O_3 NPs synthesized using 0.8 M acetylferrocene and OA at A) 10 s, and B) 14 s heating. 49

Figure 3.12 Magnetization *vs.* magnetic field plot for γ-Fe_2O_3 NPs produced using 0.8 M acetylferrocene and oleylamine 5 s, 7 s, 10 s, and 14 s heating time. 49

Figure 3.13 TEM images of IONPs produced by using 0.8 M acetylferrocene and trioctylamine at different reaction times A) 5 s, B) 7 s, C) 10 s, and D) 14 s. (E, F, G, and H) are the particle size distribution plots, respectively. 50

Figure 3.14 HRTEM images of γ-Fe_2O_3 NPs produced by using 0.8M acetylferrocene, and TOA at different reaction times A) 5 s, B) 7 s, C) 10 s and D) 14 s indicating (115), (016), and (022) lattice planes of γ-Fe_2O_3 51

Figure 3.15 PXRD of γ-Fe_2O_3 NPs synthesized using 0.8 M acetylferrocene and trioctylamine at 14 s heating. 51

Figure 4.1 TEM images of Fe NPs produced using 0.8 M $Fe(CO)_5$ and 1- ODE at different reaction times (A) 5 s, (B) 7, (C) 10 s, and (D) 14 s (7 + 7 s). (E)–(H) are the particle size distribution plots, respectively. 58

Figure 4.2 HRTEM images of iron NPs produced using 0.8 M $Fe(CO)_5$, and 1-ODE at different reaction times (A) 7 s, (B) 10 s, and (C) 14 s (7 + 7 s), indicating (011), (011), and (002) lattice planes of Fe NPs, respectively. 59

Figure 4.3 PXRD of iron NPs synthesized using 0.8 M $Fe(CO)_5$ and 1- ODE at A) 10 s and B) (7 + 7) s heating time. 59

Figure 4.4 Magnetization vs magnetic field plot for Fe NPs produced using 0.8 M Fe $(CO)_5$ and 1-ODE at 5, 7, 10, and 7 +7 s heating time. 60

Figure 5.1 TEM images of Ge NPs produced using **(A)** 0.025M GeI_2, **(B)** 0.05M GeI_2, **(C)** 0.075M GeI_2, and **(D)** 0.1M GeI_2 at 5 s heating time. The size distribution plots are presented in supporting information **Figure 5.S2** 67

Figure 5.2 Effect of precursor ratio on the size of NPs. (A) GeI_2/GeI_4=100/0, (B) GeI_2/GeI_4=75/25, (C) GeI_2/GeI_4= 50/50. (D-F) are corresponding size distribution plots. 68

Figure 5.3 Effect of reaction time on the size of NPs. (A) 5 s, (B) 5*2 s, (C) 5*3 s, and (D-F) are corresponding size distribution plots 70

Figure 5.4 Spectroscopic characterization of Ge NPs. (A) UV-Vis-NIR absorption and (B-D) are transient absorption spectra of corresponding NPs 71

Figure 6.1 TEM images of MnO produced using 0.3M $Mn_2(CO)_{10}$ and oleylamine at 5 s heating time at different scale bars 75

Figure 6.2 EDX spectra of MnO produced by 0.3M $Mn_2(CO)_{10}$ and oleylamine at 5 s heating. 76

Figure 6.3 TEM images of MnO produced using 0.3M $Mn_2(CO)_{10}$, OA, and 1-ODE at 5 sec heating time at different scale bars. 76

Figure 6.4 EDX spectra of MnO produced using 0.3M $Mn_2(CO)_{10}$, OA, and 1-ODE at 5 s heating time. 77

Figure 6.5 HRTEM images of single MnO NPs. Individual crystal domains are outlined in red along with their respective calculated d-spacings. 77

Figure 6.6 (A) TEM images of Fe/Mn Oxide NPs produced using $Mn_2(CO)_{10}$ powder and Fe (CO_5) and 1-ODE at 7 s heating time (B) Corresponding EDX spectra. 78

Figure 7.1 Illustration of n-type Bi doping in Ge NPs 80

Figure 7.2 Schematic illustration of the inductive heating assisted Bi doping of Ge NPs 80

List of Tables

Table 1.1 A comparative study of heat-up and HI method of colloidal NPs synthesis. 18

Table 2.1 Table indicating the synthesis of various NPs, precursors, and solvents used, resulting size of NPs that will be discussed in various chapters of this dissertation. 31

Acknowledgments

I would like to express my sincere gratitude to my doctorate advisor, Professor Viktor Chikan, for the opportunity given to work under his guidance. I feel very proud of being his student. I greatly appreciate the freedom and opportunity he has given to pursue my research in my way. By providing a friendly and informal atmosphere, he made hard work seem much easy. I owe much of my confidence to him. I would like to thank him for his encouragement, guidance, and research training during my Ph.D. research. The research knowledge and skills I have learned from him are the most valuable achievements of my Ph.D. degree.

My cordial thanks to my graduate committee members, Professor Jun Li, Professor Bin Liu, Professor Santosh Aryal for their continuous support and guidance throughout my graduate study. Thank you Professor Supreme Das for being the external chairperson of my defense. A special thanks to Professor Christer B. Aakeroy and Professor Daniel Higgings for the opportunity to attend graduate school at K-State. I would also like to thank our collaborators of the DOE project, Professor Bin Liu at Kansas State University, Professor Peter Heinz Pfromm at Washington State University for their guidance and support. I would like to extend my sincere thanks to Professor Christoper Elles at the University of Kansas for the Transient Absorption study of germanium nanoparticles. Thanks to Professor Tendai Gadzikawa for XRD's help and support.

I greatly appreciate Michael Hinton and Tingting Liu for their help in completing my teaching responsibility. I’d like to thank the staff at the Chemistry Department, Ron Jackson, Tobe Eggers, Mary Dooley, and Kimberly Ross, for their technical and administrative assistance. Special thanks to our glass bowler, Jim Hodgson for designing a specialized reactor for inductive heating synthesis.

With the most sincerity, I would like to acknowledge the past and current members of the Chikan's lab- Dr. Naween Dahal, Dr. George Podaru, Dr. Hongfu Luo, Basanta Acharya, Omid Shafee, Noah Holliger, and REU student Tyler John Felske. Thank you, everyone, for being a part of my Ph.D. and making my stay in Manhattan much memorable.

I acknowledge the Department of Energy for award #EC9980 for providing funding for my research, Johnson Cancer Research Center of KSU for a summer research fellowship, and the Department of Chemistry at KSU.

My sincere thanks to my parents (Bishnu Prasad Paudel and Laxmi Kumari Paudel) for their unconditional love and sacrifice to raise and educate me. Thanks to my brother, Gaurab, and sisters, Pratigya and Prativa for their love and support. I would like to extend huge respect and thanks to my in-laws, especially my mother-in-law (Laxmi Marasini) for coming overseas and supporting me while my husband was far away from me. A deep appreciation to my beloved husband, Dr. Ramesh Marasini for being my best friend and sometimes behaving like my guardian and taking care of me, guiding, and pushing me hard to achieve my goals! He has always encouraged me to pursue my dream and supported me during my good and hard times. I will be always grateful for those countless sleep hours that he has sacrificed to help me prepare for TOEFL examinations, proofreading my manuscripts, thesis, organizing my presentations, and listening to me while practicing presentations, and providing valuable suggestions. My Ph.D. research would not have been possible without his love, help, guidance, and encouragement. An enormous amount of thanks to my dear son Eric Marasini. His arrival has made my days a little shorter and nights a little longer! But he is my motivation to work hard every day. Thank you, son, for making me a cheerful and hard-working mom!

Dedication

To my beloved husband

Dr. Ramesh Marasini

To my Ph.D. advisor

Dr. Viktor Chikan

(Without them this work would never have been accomplished)

Chapter 1 - Introduction

1.1 Background

Since Nobel prize winner, Richard Feynman's famous talk titled "There's Plenty of Room at the Bottom", nanotechnology has become an important area of research and development: One of the important building blocks in nanotechnology are so called nanoparticles (NP). In general, NPs are a class of nanomaterials acting as a bridging link between the atomic/molecular structures and nanomaterials.[1] NPs are particles between 1 and 100 nanometers in size and can be made up of a variety of materials such as carbon, metal, metal oxides, or semiconductors. These particles can exist in various physical states such as in solids, colloidal solutions, or gas-phase and can take various forms, shapes, and sizes based on the specific application requirements.[2] For instance, they can be spherical, cylindrical, tubular, conical, hollow core, spiral, flat, or irregular. Their surface can be uniform or irregular with surface variations.[3–5] From the fundamental physics point of view, a NP can be classified according to the quantum mechanical charge carriers in solids, where electrons are confined, and their relation to their free movement in various dimensions.[6] A zero-dimensional (0D) NP where the particles inside the material are confined in all three dimensions such as the case for so called semiconducting quantum dots. So, the remaining dimensional freedom is zero.[7] A one-dimensional (1D) NP such as nanowires, the charge carriers can freely move in one dimension but confined in the other two remaining dimensions such as the case for CdSe or silicon nanowires.[6–8] Similarly, a 2D charge carrier can freely move in two dimensions as it happens in graphene, carbon nanotubes or multi-layered semiconducting materials such as GaAs quantum wells sandwiched between AlGaAs, or InGaAs.[9–12]

NPs have gained prominence in technological advancements due to their tunable physicochemical characteristics such as melting point, wettability, electrical and thermal conductivity, catalytic activity, light absorption, and scattering resulting in enhanced performance over their bulk counterparts.[13,14] They possess a large surface area to the volume ratio, increased reactivity, or stability in a chemical process, and enhanced mechanical strength compared to their bulk counterparts.[4,15] Depending upon their origin and synthesis methods employed, NPs possess unique physicochemical, structural, and morphological characteristics, which are important in a wide variety of applications concomitant to electronic, optoelectronic, optical, electrochemical, environment, and biomedical fields.[13,10,16,17,5] For example, Ge NPs prepared using metathesis reaction between germanium chloride ($GeCl_4$) and germanium zinc salts such as sodium germanide (NaGe) showed strong quantum confinement which finds an application in optoelectronic applications.[18]

Numerous synthesis methods exist or are under development to synthesize NPs. In general, two main approaches for nanoparticle synthesis are utilized based on either the top-down or the bottom-up approach.[19] A simplified representation of the process is presented in **Figure 1.1.**

1.1.1 Top-down method

In the top-down approach, large pieces of material are systematically broken down into smaller pieces to generate the required nanostructures. In this process, the bulk materials are used as the starting materials and treated by physical means such as mechanical milling, nanolithography, laser ablation, sputtering and thermal decomposition, etc. to synthesize nanomaterials.[20] The goal of these processes is to break the chemical bonds holding together the bulk material. The top-down approach can be used to fabricate a wide variety of devices with high reliability and high integrity therefore, this approach is common in the semiconductor device industry.[21] Many of the novel nanostructures, like nanowires and nanopores, may be fabricated with top-down approaches.[22,23] For instance, Stern *et al.* reported silicon nanowires fabricated by the top-down approach that were used to detect biological samples without any labeling.[23] Although the top-down approach has been playing a vital role in the fabrication of nanostructures but at very small scales (less than 100 nm), it has several limitations such as the development of imperfections in processed materials, high cost (lithographic processes), the requirement of high surface finished materials, longer etching times, etc. Such imperfections have a significant impact on the physical and chemical properties of nanostructures and nanomaterials.[14,23–25] The particles synthesized by this method generally have a broad size distribution. The NPs synthesized by this method are typically larger and cannot be reproduced resulting in irreproducible catalytic activity.[13,19] In addition, breaking down materials by mechanical means will cost more and more energy as creating new surface in the material cost energy and the resulting material can contain lots of undesired defects as well degrading the property of the material. Some of these problems/challenges can be circumvented as we will show in the next approach which is the bottom-up method.

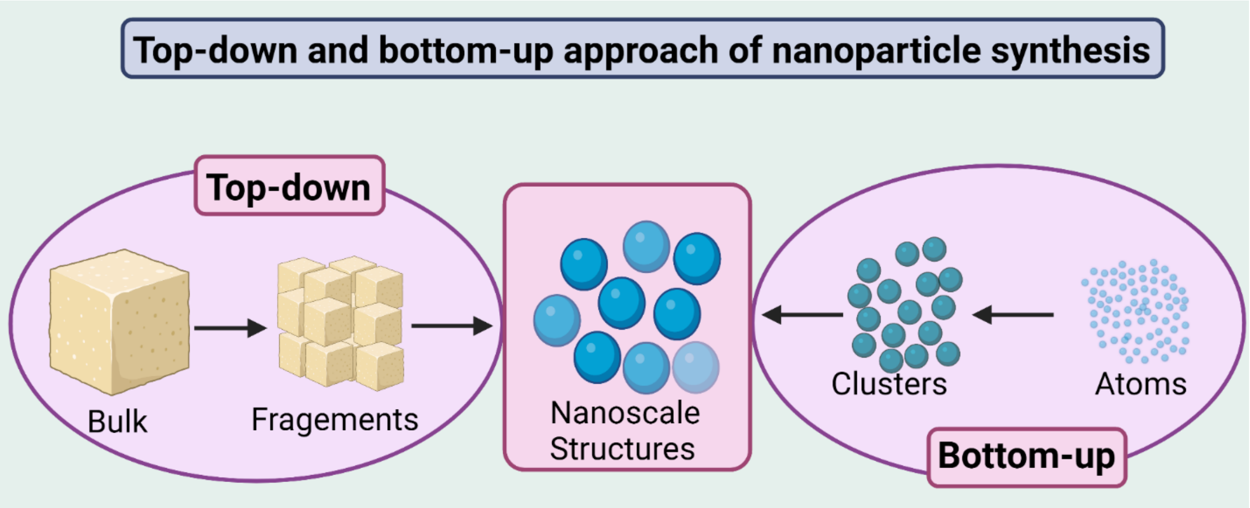

Figure 1.1 Top-down and Bottom-up synthesis of NPs

1.1.2 Bottom-up method

A bottom-up synthesis is a method where the nanostructures are synthesized from the basic constituents of the bulk material such as molecules and atoms, ions. This regime represents an area where the traditional chemistry toolbox plays an important role. The atoms are stacked together, which gives rise to crystal planes, crystal planes further stack onto each other, resulting in the formation of larger structures in the nanometer size range. The bottom-up synthesis method is often termed the “wet” method since it involves batches of solvents and other chemicals. In the bottom-up process, the single atoms or ions are allowed to grow into clusters or nanoparticles using wet chemical synthetic methods such as chemical reduction of metal salts, and the decomposition of precursors using thermal, photolytic, or sonochemical treatment. In general, two basic methods are utilizing the bottom-up approach, i.e., gas-phase synthesis and liquid-phase formation.[10,12,13] Some of the methods used in the bottom-up approach include plasma arcing, chemical vapor deposition process, metal-organic decomposition, laser pyrolysis, molecular beam epitaxy, sol-gel method, wet synthesis, and self-assembly processes. The particles synthesized by this method can achieve narrow size distribution particles and high crystallinity, which is essential for well-defined and controlled physical properties.[14] The unique advantage of the bottom-up approach is the potential to assemble nanostructures where the top-down approach fails. Even with sophisticated photolithography, it is not easy to fabricate nanostructures at a size of a few nanometers due to the diffraction limit of the light used in the process. Recently, the XUV nanolithographic methodology developed by ASML can reach wavelengths of 13.5 nm, which can produce 5 and 3 nm Logic nodes and leading-edge DRAM nodes which are below the 7 nm diffraction limit. This process allows mass production of chips, however, required very complicated and expensive machinery to produce light at 13.5 nm. Self-assembly is an ideal approach, which can produce structures much faster, cheaper with larger throughput.[21] For instance, the recent development of wet-chemistry (bottom-up approach) for colloidal synthesis and surface modifications of QDs such as InP have excelled in many commercial applications such as light-emitting diodes that are very appealing.[26] The particles synthesized by this method have narrow size distribution.[14] Therefore, the bottom-up approach is more beneficial and favored in NPs synthesis due to many merits such as fewer defects, more homogenous chemical composition, and better ordering. The bottom-up approach also utilizes chemical methodologies and is more suited for chemical industries to achieve good process control of the material qualities.[27] Bottom-up approach is also well suited to address problems such as global electricity needs (~25000 TWh in 2021) via constructing quantum dot/conductive polymer solar cells at a large scale.[2,3]

1.2 Colloidal synthesis of NPs

Colloidal NPs or quantum dots (semiconducting particles exhibiting quantum confinement) are considered very important in fundamental science. In nanoscale dimension, the size control can be fully exploited to engineer the properties of the material, plus the very large surface to volume ratio ensure more efficient use of expensive and rare materials. As we enter an age where sustainable practices will take more importance to ensure manufacturing and synthesis, practices are in line with their environmental impact. Spatial confinement effects become increasingly important as the dimensions of NPs decrease below a certain critical limit, which leads to size- and shape-dependent electronic structure.[28,29] Furthermore, as the NPs size decreases, the number of atoms is reduced from a few thousand to a few hundred, and therefore the surface to volume ratio increases dramatically (e.g., from 5% to 50% for a reduction from 20 to 2 nm in diameter).[28,29] Therefore, the contribution of the surface to the total free energy of a NPs becomes significant and increases with decreasing size, making the interaction between the surface atoms and surfactant molecules extremely important.[30] As a result, NPs become easily dispersible in solvents (somewhat comparable in size to molecules) thereby making fabrication and processing in solution possible, which is an essential advantage of colloidal NPs over nanomaterials prepared by other techniques such as molecular beam epitaxy.[30] Their properties can be tailored concerning parameters such as chemical composition, ligand coating, size, and shape.[31] These versatile properties of colloidal NPs make them potential candidates in different fields such as biomedical applications and energy conversions.[32] In particular, control over the NPs size and morphology has been an important challenge in materials chemistry. To overcome these challenges, great efforts have been made in recent decades to attain accurate control through the development of synthetic protocols that now enables access to particles with specific shapes.[31,33] In particular, the change of temperature, the choice of precursors, catalysts, surfactants, and their relative concentration ratios have been demonstrated to strongly influence the growth of NPs during colloidal synthesis and their resulting morphology.[1,31,34,35]

Without using expensive equipment, the preparation of NPs by colloidal synthesis can be conducted in the laboratory. Due to the flexibility in selecting different reducing agents, capping agents, solvent systems as well as synthetic conditions; colloidal synthesis can be utilized to produce NPs in a variety of compositions, shapes and sizes, and surface chemistry.[29,36] Additionally, they can be used as building blocks for complex nanostructures, such as NPs superlattices.[28] Therefore, colloidal synthesis is an important tool in the toolbox of chemists to develop new nanomaterials for the demands of today's industries.[37] A key disadvantage of the lab-scale methodologies currently available are not easily scalable for industrial production due to limited mass and heat, which will be addressed later in this dissertation.[38]

The colloidal synthesis generally involves several consecutive steps including nucleation, growth, and isolation of the particles to achieve the desired size from a reaction solution.[26] The development of reliable and reproducible methods for the production of monodispersed colloidal NPs has been very challenging in materials chemistry.[39] The most important pre-requisite for the preparation of particles with narrower size distribution is the good separation of nucleation and growth under diffusion-controlled reaction conditions.[17,40] Typically, nucleation and growth of nanoparticles occur in the solution phase in the presence of surfactant molecules.[38]

The classical theory of nucleation and growth considers particles as bulk material. Generally, the two different terms determine the growth rate of the particles: one responsible for the formation of new bonds, and the other the energy required to form new interfaces between different phases.[41] These two terms compete with each other in the equation of free energy of the system, and therefore a maximum could be found. And since these terms are expressed as functions of particle radius, a so-called critical radius could be determined, where the particle size is thermodynamically favored.[41,42] Simply, the free energy is expressed as

$\Delta G = -4/3\ \pi r^3\ |\Delta G_V| + 4\pi r^2 \gamma$ ....equation 1.1

where ΔG_V is the unit volume free energy difference between two phases, γ is unit area surface free energy, r is the particle radius. From equation 1, it is clear particles are assumed to be spherical.[43] Therefore, the main concern is to find out the state of related parameters when $\mathrm{d}\Delta G/\mathrm{dr}=0$. To achieve this, several assumptions and approximations need to be made regarding the chemical potential of absorbing/dissolving a monomer, flux of monomers towards/away from the nuclei, and initial monomer saturation. The theory utilized in Talapin et al.'s simulation could be adopted, which gives $dr/dt \propto S$, with S being the dimensionless initial supersaturation ratio.[44] Finally, another assumption can be made regarding the rate of nucleation in the solution described by Nielsen as follows [44]

$J_N = B_N \exp(-\Delta G^{\ N/RT})$...............equation 1.2

$\Delta G_N = (16\pi\gamma^3 V_M{}^2)/3(RT\ln S)^2$.........equation 1.3

where ΔG_N is the activation energy for nucleation, γ is the specific surface energy, and V_M is the molar volume. With these relations, we could see (**Figure 1.2**) within the regime of $1 < S < 1000$, the nucleation rate increases more rapidly compared to the growth. As the heating rate increases, the precursor molecules decompose more quickly, providing more monomers, which could either end up forming new nuclei or grow onto other existing nuclei. But since the increase of nucleation rate is greater than that of growth, it is reasonable to believe that by increasing the heating rate and therefore the initial saturation *S*, the solution will end up with more nuclei.[38,44] Most importantly, nucleation is strongly dependent on the supersaturation, therefore, at higher supersaturation of monomers, nucleation becomes prominent than growth. On the other hand, at lower supersaturation growth of particles becomes more rapid than the nucleation of new seed particles. This variance allows good separation of nucleation and growth, which can lead to the narrow size distribution of particles and therefore narrow physical characteristics of the particles a desirable quality in material science. [38,41]

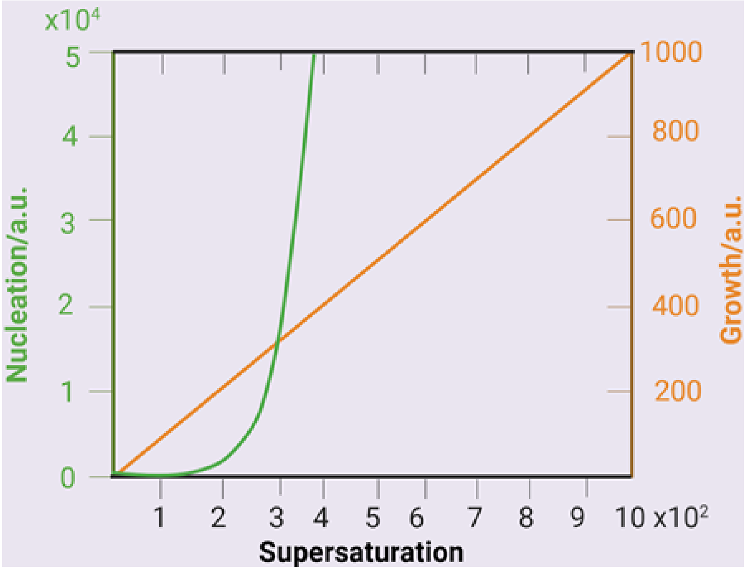

Figure 1.2 Dependence of nucleation and growth rate of monomer supersaturation S (S = 1 is the solubility of the monomer at any given temperature)[38]. In this example, a higher supersaturation environment for rapid the formation of new nuclei via homogeneous nucleation. Once monomer concentration decreases, slow growth can take over the process, which can lead to size focusing under diffusion control reaction conditions**.**

Up to date, two broad strategies have been used for preparing narrow size distributions NPs in colloidal synthesis. In the first case, nucleation and growth of nanoparticles are allowed to take place over an extended period of time at a moderate temperature (180−300 °C), which yields a NPs with broader size distribution.[41,45] An alternative to the nucleation/growth scheme is one in which a particular nanocrystal size or shape is thermodynamically stabilized by the surfactant molecule as it is realized chemical processes such as the digestive ripening of metal particles.[46] It involves heating a colloidal suspension at or near the solvent boiling point in the presence of a surface-active ligand. Digestive ripening is a unique process in colloidal synthesis that can enable the direct conversion of polydisperse nanoparticles into monodisperse ones. However, such a strategy usually relies on strongly coordinating ligands such as alkyl thiols to initiate etching and stabilize the surfaces and thus affords nanoparticles with hydrophobic and passivated surfaces.[46,47]

Literature reports suggest that digestive ripening significantly reduced the average particle size and polydispersity.[47] Leff *et al.* have presented a synthesis for Au particles in which nanocrystal size is completely controlled by surfactant concentration over a broad size range (1.5—20 nm diameter).[48] In addition, they have described the statistical thermodynamic theory for surfactant control of particle size as it works only for the few systems like giant Cu_2Se clusters and certain CdS nanocrystals.[49] In their model they have assumed gold NPs the spherical drops that are established by the thiols. The number of gold atoms n_{out} at the interface of the nanocrystal, and adjacent to thiol molecules, is obtained by

$$n_{out} = \left(\frac{4\pi}{3\vartheta_g}\right)\left[(R-\partial)^3 - (R-\partial-2.38)^3\right] \quad \text{............. Equation 1.4}$$

and the number of thiols surrounding the n- sized nanocrystal is given by,

$$n_{thiol} = 4\pi\ (\frac{(R-\delta)^2}{(21.4\ \text{Å}^2)} \qquad \text{............ Equation 1.5}$$

where R is the radius reaching from the center of the crystal to the end of the surfactant chain, δ is the length of the surfactant, and (R- δ) makes the radius of the gold portion of the nanocrystal.[48]

The second approach involves the separation of nucleation from growth by injecting precursor solution rapidly at higher temperature (350 °C) to induce nucleation and then reducing the temperature during the growth phase yielding particles of one size.[38,41,44] But, this approach precisely relies on the kinetics of the initial nucleation and growth.[41,50] The surfactant molecules play a key role to determine the kinetics of nucleation and growth.[41,50–54] Generally, theories like LaMer burst nucleation have been used to describe the nucleation and growth of NPs in solution.[38,55–57] This theory have been discussed exclusively below.

Mechanism of nucleation and growth in colloidal synthesis

The LaMer model (**Figure 1.3**) for the growth of monodisperse colloids, developed in the 1950s for colloidal sulfur, offers a simple conceptual framework to consider the formation of NPs.[58,59] In qualitative terms, while initiating a reaction, there is a build-up of precursors creating a degree of supersaturation as shown in **Figure 1.3,** Stage I.[60] When the level of supersaturation surpasses the critical nucleation threshold, "burst-nucleation" occurs (**Figure 1.3,** Stage II), reducing the degree of supersaturation. If the rate of nucleation outstrips the rate of precursor formation, the precursor concentration will drop back below the nucleation threshold. NP growth may then proceed by several pathways: i) monomer addition, in which additional precursor units deposit onto the preformed nuclei from solution; ii) Ostwald ripening, whereby energetically disfavored small nuclei redissolve and deposit onto more thermodynamically favorable larger nuclei; and iii) coalescence, in which multiple nanoparticles come together and fuse (**Figure 1.3,** Stage III).[41,55–61] This framework allows us to consider methods by which both size and size distribution may be controlled.

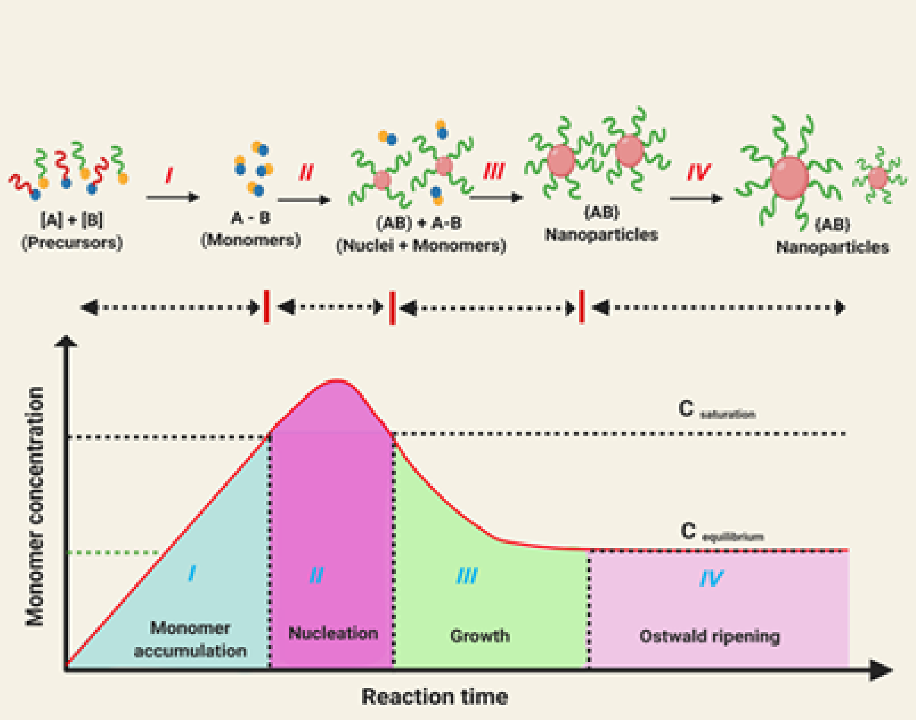

Figure 1.3 Schematic of LaMer diagram indicating three different stages of nucleation and growth of NPs as discussed above.

The growth and Ostwald ripening of NPs of diffusion-controlled reaction (**Figure 1.3**, Stage III and IV) can be theoretically explained by the work of Talapin *et al.*[44] The size distribution decreases when the supersaturation increases and Ostwald ripening occurs when supersaturation drops down **(Figure 1.4 A). Figure 1.4 B** shows the temporal evolution of the particle size distribution during diffusion-controlled Ostwald ripening (K = 0.001). It is seen that size “focusing” occurs initially (when K= 0.1 or 0.2) then as K increases Ostwald ripening takes over. This is better explained by the following equation,

$$\frac{\delta r^*}{\delta \tau} = \frac{S - exp\,[\frac{1}{r^*}]}{r^* + K\ exp\,[\frac{\alpha}{r^*}]} \text{ ....Equation 1.6}$$

K is a dimensionless parameter describing the type of control of the process (the ratio between diffusion and reaction rate constants for a flat interface); *S* is a dimensionless parameter describing the oversaturation of the monomer in solution.[44]

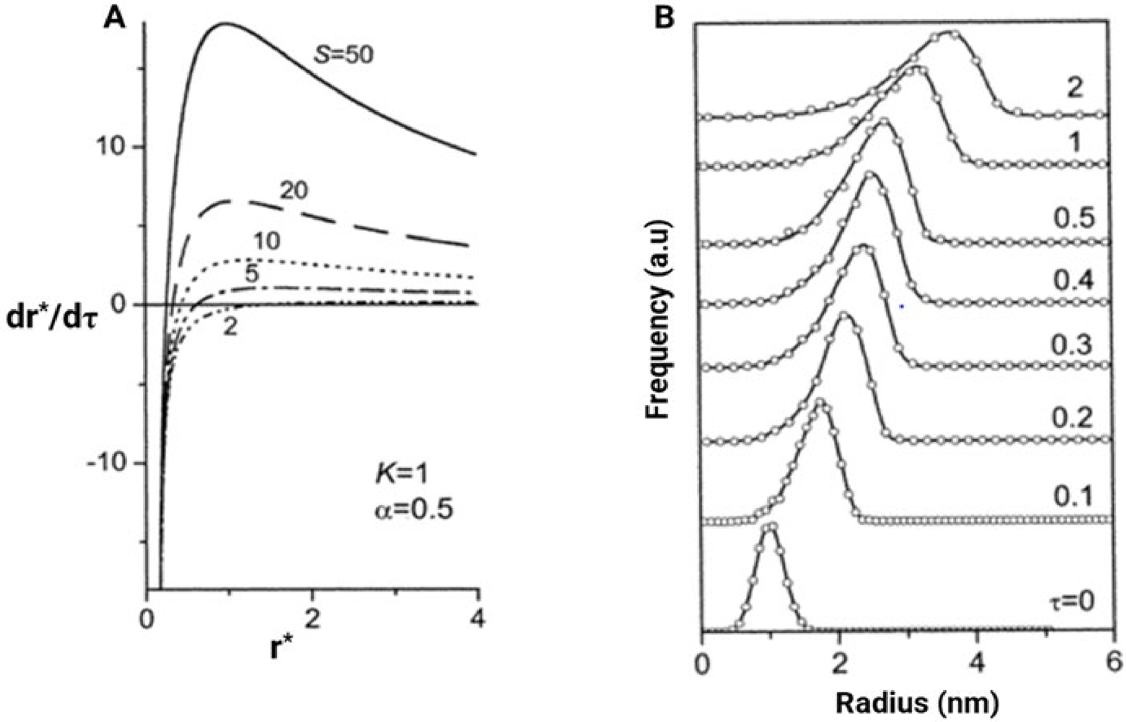

Figure 1.4 (A) Growth rate vs NP radius for a single NP for K=1, **(B)** Temporal evolution of size distribution of NP ensemble during the Ostwald ripening under diffusion-controlled reaction (K= 10^{-3}).[44] (Reprinted with permission from ref. 41. Copyright © 2001, *American Chemical Society.*)

In most batch reactions involving sol-gel or conventional hydrothermal or solvothermal reaction, precursor formation occurs over a long period owing to slow heating rates. Consequently, the precursor concentration is often maintained above the critical nucleation threshold for extended periods, and nucleation occurs continuously and concurrently with growth which gives rise to broad particle size distributions.[51,55,60,61] If enough reaction times are allowed, then particle size will 'focus'. Focusing occurs when nuclei formed throughout the reaction grow by addition from solution, giving initially a polydisperse sample.[41,44,56,60] Sugimoto *et al.* have suggested that the rate of diffusion-limited growth will vary with particle radius in such a way that small particles will grow faster than larger ones.[62] When this effect is combined with Ostwald ripening and coalescence, this leads to the focusing effect—a narrowing of the size distribution, with the formation of larger particles at the expense of smaller, less stable nuclei.[41,42,44,57] Thus, while the particle size distribution may narrow, the actual size increases significantly. Careful selection of the solvents, reagents, capping agents, and micelles to control the kinetics of both nucleation and growth can mitigate these size increases while maintaining a narrow size distribution, though this adds further complications and the need for long reaction times remains.[17,38,63]

An alternative strategy that can tremendously decrease the required reaction times is the temporal separation of the nucleation and growth stages.[41,44,55] In this case, nucleation must effectively happen only once, through a "burst nucleation" step.[38,57,60] This can be achieved by the extremely fast generation of the precursor such that the critical nucleation threshold is passed quickly. Rapid nucleation then relieves the supersaturation. This initial nucleation step must be sufficient to bring the precursor concentration back below the critical point, and without the addition of further precursor, no new nuclei may be formed. By achieving this fast burst of nucleation, there are minimal size discrepancies, thus limiting Ostwald ripening.[41,44,51,55,56,64] This leads to nuclei of similar size, which grow almost exclusively by diffusion. This gives a narrow size distribution, with the possibility of size control by varying reaction times and the addition of further precursors while maintaining the concentration below that required for nucleation to occur.[38,51,55,57,61,65] This approach has been used extensively in hot-injection processes for the growth of monodisperse metal, metal oxide, and semiconductor QDs quantum dots, where small sizes and narrow size distributions are critical.[17,26,37,52,63] To prevent growth and to limit the nanoparticle size to near that of the initially formed nuclei, it is possible to induce the nucleation burst and then immediately stop any further reaction. This can be achieved by limiting the available precursor, either by ensuring that the initial nucleation consumes all available precursors, by quenching the reaction mixture, or by removing any driving force necessary for further growth such as temperature.[41,55,60,66] Therefore, surfactant molecules play a key role to determine the kinetics of nucleation and growth.[41,50–54] For instance, faster nucleation produces bulk material and slow, the reaction simply produces small molecular clusters. Therefore, the balancing of these different mechanisms is challenging.[55] This could be addressed by choosing a good combination of surfactants, solvents, reaction conditions, and concentration of precursor molecules.[56] Achieving a reproducible synthetic condition with desired shape, morphology, size, and composition is very important to implement a material for practical applications. In this dissertation, we utilized the synthetic approach having several reducing agents/solvents/binding ligands such as oleylamine, trioctylamine, 1-octadecane, etc. All of the reactants are mixed in a nitrogen atmosphere and synthesis is carried out in an inert atmosphere of argon thus preventing exposure to moisture. Different strategies are applied to tune the size of the nanoparticles during synthesis. Before going to the details of the synthesis methodology employed, it is worth discussing the most commonly used important methods of colloidal synthesis of NPs and QDs and their limitations.

1.3 Hot-injection method

With the development of colloidal synthesis methodologies for nanomaterial, it has been realized that the size distribution of nanoparticle solutions will broaden over time due to Ostwald ripening. The hot-injection (HI) method was developed to tackle the challenge associated with Ostwald ripening process naturally taking place in colloidal solutions. Now, HI methodology is well-established synthetic strategy to synthesize monodisperse colloidal NPs and quantum dots (QDs).[38,45,67] Bawendi and co-workers first introduced the hot-injection method in their synthesis of cadmium chalcogenide nanocrystals.[24] This method is based on the work of LaMer and Dinegar, who described how the production of monodisperse colloids is dependent on rapid nucleation followed by the controlled growth of the existing nuclei (**Figure 1.3**). This method is one of the most common methods to control monomer supersaturation effectively colloidal synthesis there by, separating the nucleation and growth steps.[38,45] The HI method separates nucleation and growth by rapid injection of a solution of a monomer precursor followed by immediate decomposition.[53] At the initial stage, the temperature drops further increase supersaturation favoring nucleation over crystal growth.[53] But later the monomer supersaturation rapidly drops, and crystal growth takes over. At this stage, the monomer supersaturation remains relatively high, which can achieve efficient size focusing.[41,55] As the growth progresses, Ostwald ripening occurs, in which the larger particles continue to grow while the smaller particles dissolve due to their higher chemical potential. Until the point of saturation (**Figure 1.3**), the average particle size increases, and the concentration of the particle decreases.[38,41,50] To this date, a diverse set of NPs such as iron oxide nanoparticles (IONPs), CdS, CdSe, CdTe QDs are being synthesized using the HI method.[41,45,67] The reaction solution used during this process also contains surfactant molecules/ligands to prevent QDs and NPs from agglomerating. The ligands that are typically employed include alkylphosphine and alkyl phosphine oxides (e.g., trioctylphosphine and trioctylphosphine oxide), long-chain carboxylic acids (e.g., oleic acid,), and long-chain amines (e.g., oleylamine). [13,33,61,64,67] The HI method is particularly effective because it offers a high level of control over the size of the particles and size distribution by allowing rapid nucleation separated from the growth stage. By varying the temperature, concentration of the surfactants, and reaction time, it is possible to obtain particles of various sizes.[26,38,55]

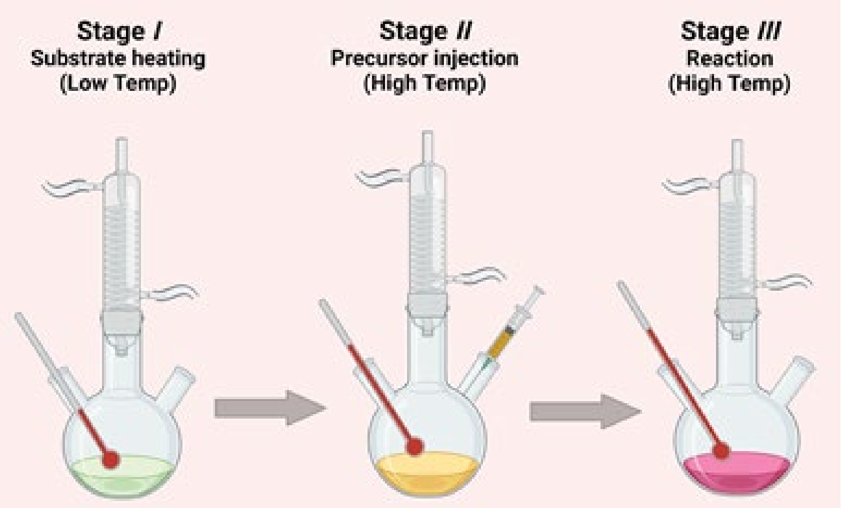

Figure 1.5 Representation of the simple synthetic apparatus employed to prepare monodisperse NPs/QDS by HI method.

1.4 Limitations of existing methods and motivation to this work

Although lots of work is presented in the literature using the HI method, this method is essentially a batch reaction developed for small-scale production with limited scalability due to heat and mass transport requirements. In the first step of the HI method, the precursor mixing in the initial step takes some time to form a homogeneous mixture of precursors. Therefore, it's very challenging to maintain reproducibility as the timescale of mixing is similar to the growth and nucleation of the colloidal nanomaterials.[38,41,51] In addition, precursor molecules are usually miscible liquids that can ensure high concentration in the solution after injection causing solid precursors to having limited use in the HI method due to solubility limits in the injected volume.[37,52] Therefore, the HI technique is suitable only for small-scale exploratory research, providing typically less than 1g of NPs products, and it will be not practical to reach the industrial level production of nanomaterials.[38,50,55,64] For example, four-junction solar cells utilizing various types of semiconducting QDs for solar cells would require hundreds of tons of QD produced to address global electricity needs.[68]

The induction heating (IH) method described in **Chapter 2** could resolve some of the shortcomings of existing methodologies. IH synthesis of nanomaterials can achieve high heating rates(100-300°C/sec) i.e., 6,600 times faster than using a typical heating mantle (1°C per minute). thus producing similar outcomes as expected for HI methods.[38] IH-assisted NPs synthesis has the potential to produce materials rapidly and in industrial quantities. **Table 1.1** discusses the comparative study of the hot-injection method and inductive heating method of colloidal NPs synthesis, and the detail of experimental set-up is presented in **Chapter 2** of this dissertation.

	Hot-injection method	**Inductive heating method**
Definition	It is defined as the method of NPs synthesis which involves the production of homogeneous nuclei via the rapid injection of precursor reagents into a hot solvent under diffusion-controlled reaction conditions.	It is the process of rapid heating of the precursor molecules and solvents to produce NPs indirectly mediated by magnetic field heating of ferromagnetic material placed into the solution.
Environment	HI synthesis does not have a reductive environment during synthesis so, separate reducing agents are required in NPs synthesis.	The steel ball used in the IH specialized reactor provides the reductive atmosphere to produce a reduced state of metal. **(Chapter 4)** But there may be a potential issue due to contamination from the steel ball used in synthesis.
Time	This method takes a longer time (on the scale of several minutes or hours) to produce NPs. It is limited by heat transfer from the heating mantle via poor thermal conductor glass in the lab environment.	This method produces NPs within a few seconds (as short as 2 sec). It is limited by heat transfer from hot steel balls to the solution.

Precursor	The HI method limits the use of solid-precursors in synthesis. Precursor amount is limited that can be dissolved in the solution to be injected. Large volumes could yield too much temperature drop yielding amorphous materials.	The IH method uses both solid and liquid precursors in synthesis (**Chapter 3** and **Chapter 4**). The amount of precursor can be increased to reach new synthetic conditions and higher supersaturation conditions.
Reproducibility	The time taken to inject a reagent often varies between users and from batch to batch. This leads to small differences in the initial reaction kinetics, which hinders reproducibility. Also, a potential issue with atmospheric oxygen and water during the injection.	As all reagents and solvents are mixed in the same vessel, it does not hinder the reproducibility. No atmospheric water and oxygen are present since mixing can take place in the glove box at low temperatures.
Scalability	The HI method works very well at a laboratory scale, but it poses a serious problem during scale-up due to limited heat and mass transport requirements.	It can potentially be scaled-up as it provides temperature control allowing sufficient heat and mass transport. The reactor can be operated in continuous or batch mode.

Table 1.1 A comparative study of heat-up and HI method of colloidal NPs synthesis.

1.5 Goals of the dissertation

The key goal of this dissertation is to (1) demonstrate that induction heating methodology can be used for nanomaterial synthesis in the laboratory. To achieve this goal, **Chapter 2** describes how the practical aspects of the theory of induction heating setup used in experimental protocols. Also, we wanted to show that (2) induction heating methodology will provide comparable size and size distribution of nanomaterials as HI methodology. This is described in **Chapter 3** where we explore the synthesis of traditional iron oxide nanomaterial. Furthermore, (3) not only the size, but important physical properties are also very well controlled in the IH methodology such as magnetic properties of nanomaterials produced. Additionally, we aimed to demonstrate that (4) with this methodology one can produce nanomaterials that are difficult to produce in the HI method due to the oxygen sensitivity of the precursors. This is described in **Chapter 4**, where we discuss the synthesis of iron nanoparticles, which are difficult to produce in reduced form and maintain their reduced form. Literature has shown that certain materials such as Germanium can be only produced slowly due to a slow disproportioning reaction.[69,70] In **Chapter 5** we show that (5) one can accelerate the nanomaterial synthesis utilizing the induction heating method. Finally, (6) we have explored the use of induction heating methodology for alloy and doped nanomaterials. We demonstrated this by alloying Fe and Mn first time to the best of our knowledge in **Chapter 6**.

Chapter 2 - Experimental techniques

2.1 Fundamentals of induction heating

In general, induction heating (IH) is the process of heating an electrically conducting object (usually a metal) by magnetic induction, through heat generated in the object by eddy currents (which are loops of electrical current induced within conductors by a changing magnetic field in the conductor, due to Faraday's law of induction) and/or hysteresis loss.[52,71] Here, heat is generated within the conductive material without making direct contact with the source. IH provides contactless, fast, and efficient heating of conductive materials. It involves a complex combination of electromagnetic energy and heat transfer that passes through an induction coil, creating an electromagnetic field within the coil to melt down materials. Materials such as Steel, Copper, Brass, Graphite, Gold, Silver, Aluminum, and Carbide can be heated for a range of applications like hardening, annealing, and so on. To understand the heating mechanism and circuit diagram of IH, it is noteworthy to understand three important phenomena i.e., Faraday's law of electromagnetic induction, magnetic hysteresis, and skin effect or penetration depth.

2.1.1 Faraday's law of electromagnetic induction

When an electrically conducting material (such as a metal) is placed within a time-varying magnetic field, an electric current (called an "eddy current") is induced in the part producing a second magnetic field that opposes the applied field (**Figure 2.1**). The reason behind this phenomenon is that a time-varying magnetic field disturbs the relaxed environmental condition of the electrically conducting material. As a result, the material tries to oppose this change by producing another magnetic field to cancel the imposed field.[72]

Mathematically, $\varepsilon = -N\left(\frac{\Phi B}{dt}\right)$ ………Equation 2.1

Where Ɛ is the electromotive force (EMF) in volts, Φ_B is magnetic flux in webers, N is the number of loops of the wire or number of coils.

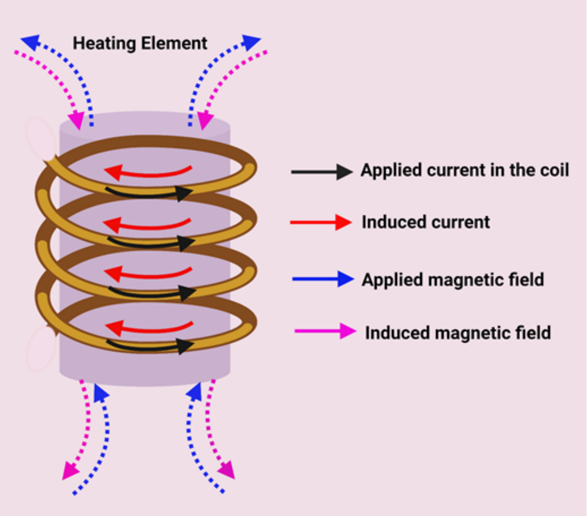

Figure 2.1 Schematics showing the illustration of Faraday's law of electromagnetic induction indicating the direction applied magnetic field, induced magnetic field, applied current, and induced current.

2.1.2 Magnetic hysteresis

In general, hysteresis is characterized as a lag of magnetic flux density (B) behind the magnetic field strength (H). It is a property of ferromagnetic materials like iron, nickel, and cobalt. The phenomenon of hysteresis in ferromagnetic materials is the result of two effects: rotation of magnetization and changes in size or number of magnetic domains.[73]

When an external magnetic field is applied in the ferromagnetic materials, the ferromagnetic domains (**Figure 2.2 A**) align to match the field. But, the ferromagnetic domains are so strong that–once they are aligned–they reinforce each other and stay aligned even after the applied magnetic field is turned off.[71] In fact, the ferromagnetic domains will retain their alignments even in the presence of an opposite applied magnetic field up to a point. Once the negative applied magnetic field is strong enough to realign the domains, B will have the opposite value. Now, if we apply a positive field again, the magnet will again switch. Cycling between positive and negative applied magnetic fields creates a hysteresis loop (**Figure 2.2 B**). The left and right ends of the loop (**a** and **d**) are called the saturation points. At this point, all the domains are aligned, so there is no more hysteresis effect. As long as H remains higher than the saturation point, there is only one value of B for one value of H–the previous value of H no longer matters. The point where B intersects the y-axis (**b** and **e**) is called remanence, retentivity, or residual magnetism. This implies how much magnetism is generated by the material itself once the external field is removed. Specifically, remanence is the value of residual magnetism which occurs if H is taken to the saturation point. The point where B intersects the x-axis (**c** and **f**) is called coercivity. The coercive force is the force required to remove the residual magnetism and return the inductivity to zero. The slope of the B-H curve is called permeability. This tells you how easy it is for the material to magnetize (how easily the domains align). The opposite of permeability is reluctance. The area within the hysteresis curve is the energy spent, or work done, by each cycle. The work depends on the remanence, saturation point, and coercivity of the material.[73,74]

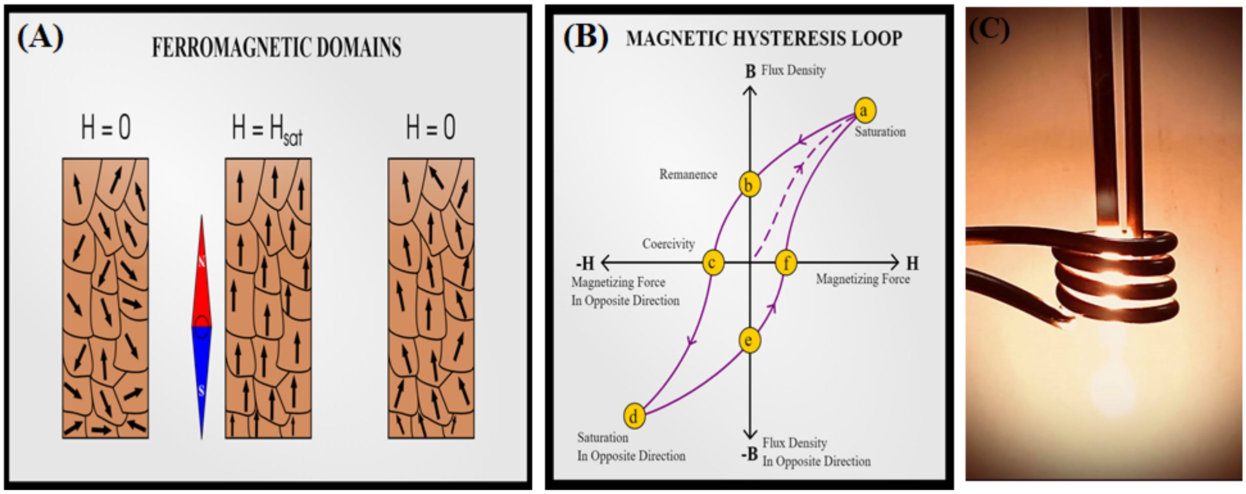

Figure 2.2 Magnetic hysteresis.[73] (A) Illustration of ferromagnetic domains at the varied magnetic field. (B) Illustration of hysteresis loop indicating the dependence of magnetic field strength with magnetic flux density. (C) Picture showing hysteresis effect in copper *vs* steel.

2.1.3 Penetration depth or skin effect

Skin effect is defined as the tendency of an eddy current to become distributed within a conductor in such a way that current density is largest near the surface of the conductor and decreases exponentially with greater depths in the conductor.[75] The electric current flows mainly at the "skin" of the conductor i.e. between the outer surface and a level called the skin depth. The alternating current (AC) density I of the conductor decreases exponentially from its value at the surface I_s according to the depth from the surface as $I = I_s e^{-t/\delta}$ ……… Equation 2.2

Therefore, the skin depth is a depth below the surface of the conductor at which the current density I decay to 1/e i.e., 37% of the density of the surface I_s (**Figure 2.3 A**).The mathematical expression for the calculation of skin depth, $\delta = \frac{1}{\sqrt{\pi f \sigma \mu}}$ ………… Equation 2.3

where δ is skin depth, *f* is the frequency in Hz, σ is the conductivity of the material (S/m), and μ is the absolute magnetic permeability of the material (H/m).[76] Hence, the skin depth depends on the frequency of the AC field, the electrical resistivity, and the relative magnetic permeability of the workpiece. The skin depth decreases with higher frequency and increases with higher temperature. **Figure 2.3 B** shows the dependence of skin depth with frequency.

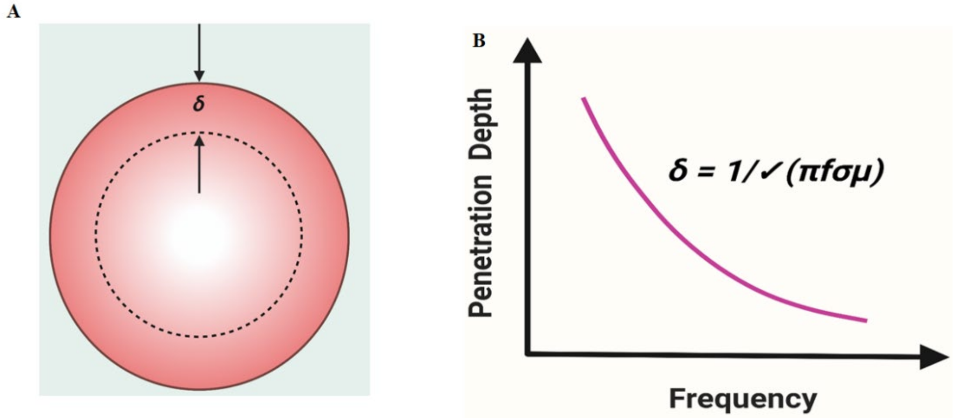

Figure 2.3 Skin Effect on a conductor. (A) Skin depth δ is the depth at which the current density is approximately 37% of the value at the surface. RF current doesn't stop at the dashed line but decreases logarithmically concerning depth in the conductor. (B) Graph showing the dependence of the skin depth with frequency.

Using high frequencies in the induction heating industry (usually 10kHz to 700kHz) implies very thin penetration depths in metals (typically less than 1mm).[71,77] Passing high current density through that shallow depth results in high power. Consequently, a higher amount of electrical energy is converted into heat energy.

2.2 Experimental set-up and heating mechanism

The setup used for the induction heating process consists of a resonance frequency (RF) power supply to provide the AC to the circuit (**Figure 2.4**). A copper coil is used as an inductor and current is applied to it. The material to be heated is placed inside the copper coil. By altering the strength of the applied current, one can control the heating temperature. As the eddy current produced inside the material flows opposite to the electrical resistivity of the material, heating is observed in the metal object. Besides eddy current, heat is also generated due to hysteresis in magnetic parts. The electrical resistance offered by a magnetic material, towards the changing magnetic field within the inductor, causes internal friction. This internal friction creates heat. The schematics of a typical inductive heating setup are shown in **Figure 2.4** below.

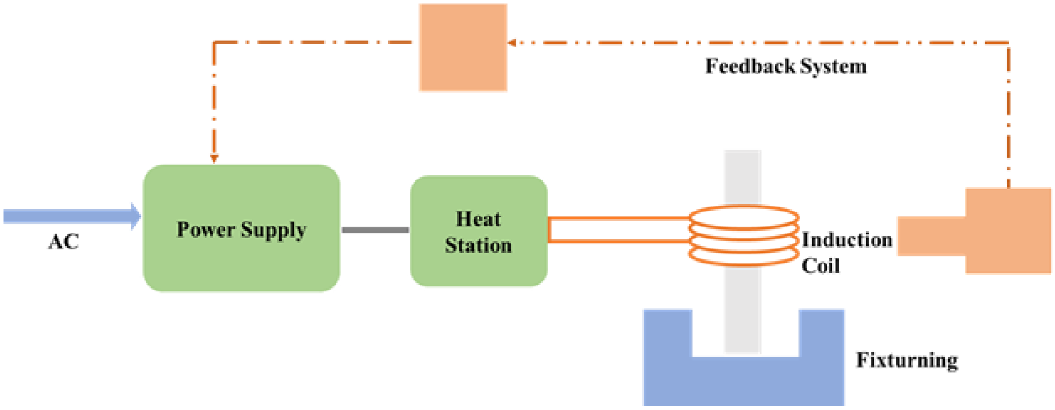

Figure 2.4 Typical induction heating setup consisting of AC power supply, heat station, induction coil, and feedback system.

When AC is passed through the coil of an inductive heater, an alternating magnetic field is generated around the electromagnet due to Faraday’s law. When the material placed inside the inductor comes in the range of this alternating magnetic field, an eddy current is generated within the material resulting in Joule heating. In addition to eddy current generation, ferromagnetic materials such as steel balls can produce heat as well and more efficiently in the presence of alternating magnetic fields because of the movement/friction of magnetic domain walls i.e., hysteresis loss. The increased temperature of the inductor forms a positive feedback loop where the heating rate increases with time.[38,52,63] **Figure 2.5 A** is the picture of the inductive heater used in our lab. Inductive heating can result in a temperature rise over 1000°C within a few seconds, thereby creating a medium of which temperature can be used for other purposes such as nanomaterial synthesis as it will be shown below.

In our experimental setup, the precursors were placed in a glass container **(Figure 2.5 B**) filled with steel balls (25.92 g, Bearing-Quality E52100 Alloy Steel, Hardened Ball, 1/8″ diameter) to allow for uniform heating. The reactor stays within an induction coil that rapidly heats the steel balls producing boiling solvent and decomposition of precursor molecules. In this technique, the heating medium located inside of the reactor, the contact surface area with the solvent is very large (approx. 34 cm^2). The heating of the actual reaction vessel is not necessary to reach the decomposition temperature of the precursor molecules required for fast heating rates. The use of steel balls provides a strongly reducing environment, therefore, removing any trace level of oxygen in typical nanomaterials making it possible to synthesize the reduced state of NPs.[37,78] An optical temperature probe was placed inside the solution. The container was filled with argon to purge out any oxygen for 1 min before heating. The hot steel ball can undergo oxidation and reaction with the water and oxygen present.[78] This can produce an environment for nanomaterial synthesis where there is a minimal amount of oxygen and water is left to react with the precursor, solvent, and the nanomaterial at high temperatures. For example, the hydrothermal method of synthesis of IONPs reported by Ge et al. possesses a serious limitation of requiring the presence of oxygen and water to produce monodispersed IONPs.[79] Under this circumstance, the IH methodology using steel balls can be considered very important as the steel balls provide the reducing atmosphere for NPs synthesis.

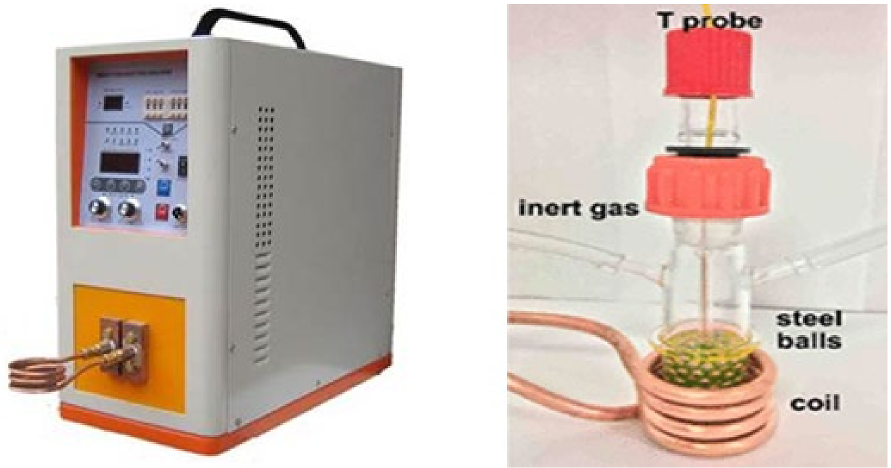

Figure 2.5 (A) Inductive heater used in this dissertation and (B) The reactor setup in the IH system.

2.3 Unique characteristic of IH and its possibility in the scale-up synthesis

The rapid IH method possesses the unique benefit of injecting an enormous amount of heat (approx. 3742 J/s, for 25g of steel ball, 8 mL of solvent, and 300°C rises in temperature) into the reactant solution in a very short period. However, the calculated amount of heat is the only minimum amount of heat as the machine is operating at the lowest limit. The machine can even work faster if we have increased the power to maximum, but we may have the problem of explosion. Induction heating synthesis of nanomaterials can achieve high heating rates(100-300 °C/s) as compared to the conventional heating mantle and recently used microwave heating, thus producing very similar outcomes as expected for HI methods.[38] **Figure 2.6** shows the comparison of heating rates by the different heating methods. At around 12.8 seconds, the temperature of the solvent rises from 28 °C to 186 °C, at a rate of 12 °C/s. However, oleylamine has a boiling point at 367 °C and during actual heating, the solvent was observed to start boiling in under 3 seconds. Due to the limitation of the temperature probe's response time, the actual heating rate could instead be as high as 110 °C/s. In a conventional synthesis, a heating mantle and temperature controller were used to first melt the solvent at 70 °C, followed by raising the temperature to 275 °C in 3 hours and 25 min, or 1 °C /min.[38,63]

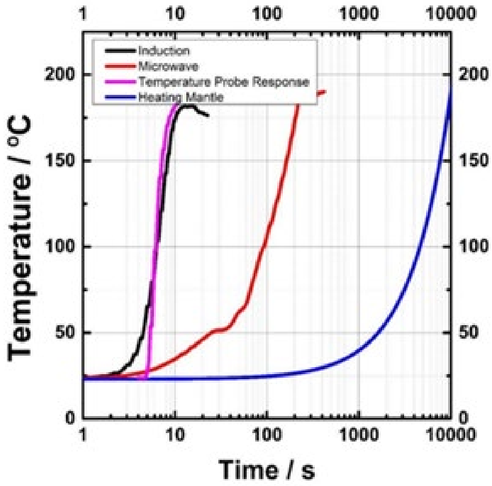

Figure 2.6 A Comparison of heating rate by induction heating, microwave, and heating mantle (from ref. 31)

IH-assisted NPs synthesis has the potential to produce materials rapidly and in industrial quantities by modifying it to drastically increase the amount of product produced in a reproducible manner compared to the conventional method, considering that the ability of cheap, bench-top mass production is one of the key attractions of nanoparticles in industrial application. Such setup consists of a continuous production system utilizing a flow-through tube design. The boiling point of the solvent can be used as built-in temperature control for achieving various final temperatures without the need for annealing and reflux. As soon as the heating starts the precursor molecules decompose thereby forming a huge number of small, monodispersed nuclei before the growth of particles starts. When Ostwald ripening starts, a larger portion of precursor molecules can be depleted. This in turn produces uniformly sized NPs. The faster depletion rate of precursor mix leads to the rapid separation of nucleation and growth. Because of these outstanding characteristics of IH, NPs can be formed within a few seconds or even sub-seconds. The limiting factor becomes the heat transfer from the surface of the steel ball to the solution, which is also assisted by the rapid degassing of the dissolved inert gas (N_2 or Ar)/boiling of the solvent. The size and crystallinity of the NPs can be tuned by varying the concentration of the precursor and heating time, which will be discussed later in this dissertation. To achieve a short heating time, the inductive heater is coupled with an electronic timer to provide second to millisecond precision switching on and off for predetermined time intervals. This setup also insures the reproducibility of the experiment i.e., demonstrated below for IONPs in **Figure 2.7**. The synthesis was done in different batches by Sharma and Holliger individually under the same condition of reaction time and concentration. The synthesized particle size and size distribution results are similar. The comparison data of the NP synthesis from two different batches is shown below in **Figure 2.7**. With the help of magnetic heating techniques, nanomaterials can be produced in a continuous or batch reactor (**Figure 2.8**).

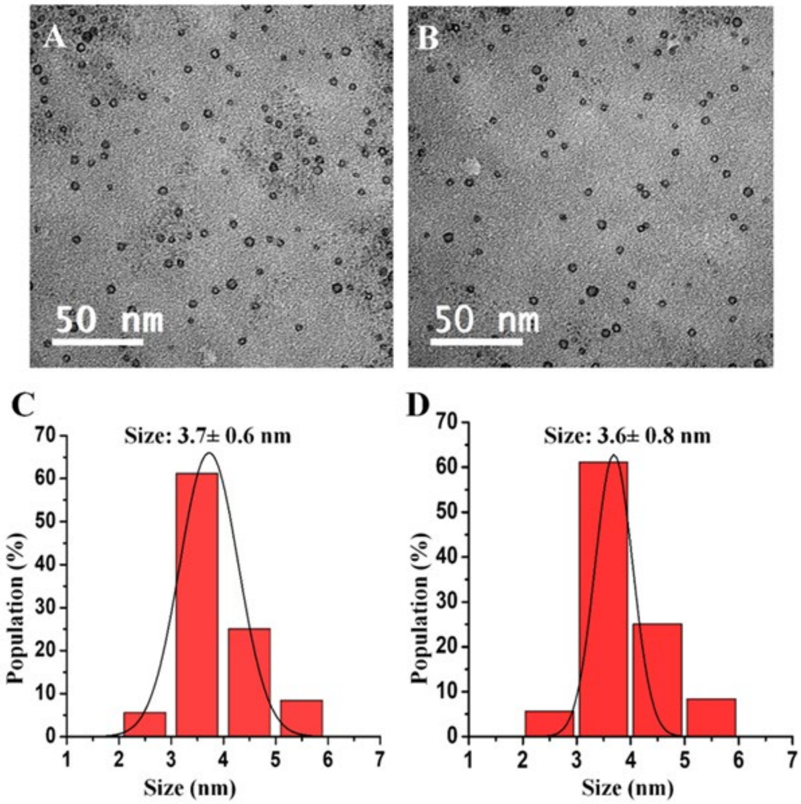

Figure 2.7 TEM images of IONPs produced by using 0.8M Fe $(CO)_5$, and oleylamine at reaction times 5 sec, by a different person (A) Sharma and (B) Holliger. C and D are the particle size distribution plots, respectively

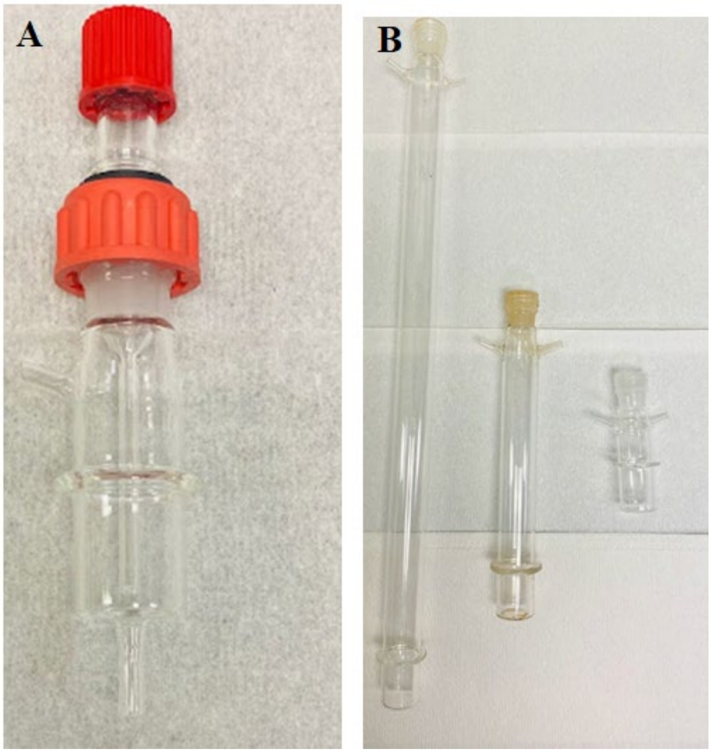

Figure 2.8 Pictures of (A) a continuous reactor and (B) batch reactors used in IH setup at our laboratory. The larger reactor is designed to provide extra space for boiling solvent in case of longer heating times.

A huge number of NPs can be synthesized in a few hours in a continuous reactor. Similarly, ultra-small NPs can be produced in a few seconds or even a millisecond timescale in a batch reactor. The magnetic heating is not only able to produce ultrasmall NPs but can influence the initial nucleation to favor the narrower size distribution of particles during the later stage of growth. For example, with a sufficiently adjusted cooling setup, the system can process 3.6 kg of nanomaterial small-scale setup.[63] The short heating time in batch reaction conditions is replaced with the residence time of the solvent/precursor in the reactor. The flow rate will facilitate to increase or decrease the residence time yielding smaller or larger nanoparticles.[38] Furthermore, this set-up can potentially be modified to increase the yield of the product as compared to the conventional heating methods. A modified setup consists of the continuous production of NPs using a continuous reactor (**Figure 2.9**).

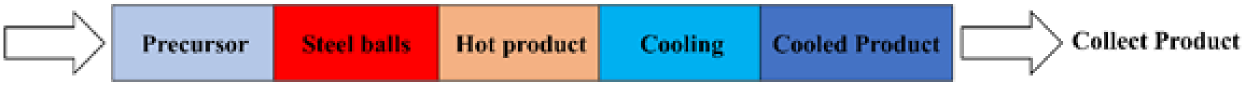

Figure 2.9 Illustration of continuous synthesis setup.

Briefly, a reactant solution is continuously pumped into the narrow tubing which connects to the inductor coil. The part of the tube inside the coil is filled with steel balls and trapped between two filters. As the solution enters the heating chamber, the reaction occurs, and NPs are formed. The solution flows continuously into the passage and external cooling is applied. The cooled product remains in the colloidal form and can be collected under atmospheric conditions in liquid form. The collected product will begin to solidify as the temperature drops down and can be stored for a longer time.

As discussed above the steel balls used in the synthesis provides the reducing atmosphere during the NP synthesis.[37] Additionally, the hot amines (oleylamine and trioctylamine) serve as a surfactant and reducing agent.[80] The literature reports suggest that oleylamine can form complex compounds with the metal ions of the corresponding precursor, leading to metastable compounds that will act as secondary precursors and can be decomposed in a controlled way to yield nanoparticles.[80] The flow rate at continuous set up can be governed by various factors such as (i) changing the medium. For example, glass balls can be mixed with steel balls or ferrofluids can be replaced by steel balls, (ii) controlling the amplitude of the reactor, (iii) reducing the diameter of the steel balls used, etc., The decrease in the diameter of the steel balls will increase the contact surface area which eventually affects the flow rate and the product formation. Therefore, a huge number of NPs can be synthesized in a few hours in a continuous reactor. Similarly, ultra-small NPs can be produced in a few seconds or even a millisecond timescale in a batch reactor. The magnetic heating is not only able to produce ultrasmall NPs but can influence the initial nucleation to favor the narrower size distribution of particles during the later stage of growth.[38,65] Therefore, the IH achieves a faster heating rate, rapid cooling, inert atmosphere, and reducing environment to prepare the reduced state of NPs. This method has an application in the synthesis of diverse types of metals/ metal oxides/ semiconductors and alloy NPs to raise the temperature of solvents to their melting point in a very short time. **Table 2.1** below summarizes how the inductive heating method is employed in the batch synthesis of NPs in this thesis.

Chapter#	NPs Prepared	Precursors	Solvents	Particle size/nm
3	γ-Fe_2O_3 and α-Fe_2O_3 NPs	Acetylferrocen, $Fe(CO)_5$	Oleylamine and Trioctylamine	3-11 nm
4	Fe NPs	$Fe(CO)_5$	1-Octadecane	3-10 nm
5	Ge NPs	GeI_2/GeI_4	Oleylamine	3-21 nm
6	MnO and Fe@MnO NPs	$Mn_2(CO)_{10}$ and $Fe(CO)_5$	Oleylamine, 1-Octadecane	4.4nm

Table 2.1 Table indicating the synthesis of various NPs, precursors, and solvents used, resulting size of NPs that will be discussed in various chapters of this dissertation.

Chapter 3 - Size controlled synthesis of iron oxide nanoparticles by inductive heating

***Chapter 3**, in full, is a reprint of the materials from **ACS Omega**, 2020, https://doi.org/10.1021/acsomega.0c02793 and **Materials Advances**, 2021, https://doi.org/10.1039/D1MA00280E with some modification.*

Abstract

Inductive heating synthesis is an emerging technique with the potential to displace the hot-injection synthesis method to prepare colloidal particles very rapidly with a narrow size distribution, controlled size, and high crystallinity. In this work, the inductive heating synthesis is applied to produce a short-temperature jump to mimic conditions like the hot-injection method to prepare traditional iron and iron oxide nanoparticles (IONPs) in the 3–11 nm size range within various solvents, precursors, and reaction time conditions. Additionally, the direct one-pot synthesis of γ-Fe_2O_3 nanoparticles (NPs) using a solid precursor, acetylferrocene in an inductive heater has been used for the first time to the best of our knowledge during the synthesis. Traditionally, solid precursors have not been used in the hot-injection (HI) technique because of their limited solubility and less likely outcome to produce the high supersaturation needed for diffusion-limited growth of the NPs. Oleylamine and trioctylamine serve as a solvent, a binding ligand, and a reducing agent in the synthesis to produce γ-Fe_2O_3 NPs with relatively narrow size distribution. The structures, morphologies, and magnetic properties of γ-Fe_2O_3 NPs are studied. The phase pure γ-Fe_2O_3 NPs obtained display uniform morphology and good magnetic property. Moreover, this inductive heating technique can be used under unique experimental conditions not available for hot-injection reactions. These conditions include the use of very high initial monomer concentrations. Considering benefits over conventional methods, the inductive heating technique has the potential to provide an industrial-level scale-up synthesis. The magnetization of these particles is consistent

with the magnetization of the particles from the literature. The IH technique has the potential to provide an industrial level scale-up synthesis in continuous reactors, which is not available for the HI method relying on batch synthesis.

3.1 Introduction

Colloidal synthesis is an important tool in the toolbox of chemists to develop new nanomaterials such as iron oxide nanoparticles (IONPs), gold nanoparticles, semiconducting materials, and so forth for the demands of today's industries. Among various nanomaterials, magnetic IONPs have received significant attention because of their numerous advantages such as inexpensive method of synthesis, physical and chemical stability, biocompatibility, and low environmental impact of manufacturing, thereby offering many unique advantages over other materials.[5,81–88] Out of eight different forms of IONPs discovered so far, hematite (α-Fe_2O_3), magnetite (Fe_3O_4), and maghemite (γ-Fe_2O_3) are very common and interesting due to their polymorphism property that involves temperature-induced phase transition.[89] Moreover, $Fe_3O_4$and γ-Fe_2O_3 exhibit many unique features such as superparamagnetism, high coercivity, low Curie temperature, and high magnetic susceptibility.[89,90] These properties make them outstanding candidates in multi-terabit storage, catalysis, biosensors, targeted drug delivery, magnetic hyperthermia, high-sensitivity bimolecular magnetic resonance imaging, bioseparation, and thermoablation.[86,89,90] γ-Fe_2O_3 and Fe_3O_4 are synthesized mainly using the hot-injection (HI) method.[84,91] In this technique, small amounts of precursor molecules are injected into a hot boiling solvent, which results in rapid decomposition of the molecular precursors thus producing inorganic nanomaterials (oxides, and semiconductors). This well-established method is used to synthesize uniformly sized colloidal IONPs in laboratory settings by giving scalable yield with precise size and shape control.[45,67,92] While the HI method for colloidal synthesis is very well-established and useful, there are drawbacks to this methodology.[38,65,93] The rapid injection of the precursor might produce uneven nucleation due to the limited heat and mass transport of the molecules during the application of the HI process in typical batch reactors.[38] In addition, precursor molecules are usually miscible liquids that can ensure high concentration in the solution after injection causing solid precursors to have limited use in the HI method due to solubility limits.[38,65] Furthermore, scaling up in the hot-injection method designed for laboratory scale synthesis is difficult due to low yield and non-uniform heat transport.[38,65] Additionally, this method strictly requires the use of a solid precursor and is difficult to scale up to large amounts of nanomaterials.[94]

There are many examples reported in the literature regarding the use of the HI method to prepare IONPs. For instance, Hyeon et al. showed the non-hydrolytic method to produce monodisperse and highly crystalline γ-Fe_2O_3. The resulting NPs were of size ranging from 4–16 nm diameter.[85] However, these synthetic protocols are complex, requiring a mixture of multiple solvents (octyl ether and oleic acid) and a long heating time followed by refluxing. In addition to this, Das and et.al. reported the solventless synthesis of IONPs through thermal decomposition of acetylferrocene.[95] In their work they used malic anhydride as a co-precursor. The resulting nanoparticle size ranged from 10–20 nm. However, their approach requires a precursor to being heated in a furnace at a higher temperature and longer reaction time i.e., 1300 °K for 4 hours resulting in irregularly shaped NPs.

To address the issues of the HI method, Sun et al. have shown highly uniform magnetite NPs through iron (Fe)–acetylacetonate decomposition by annealing at 320 °C in high-boiling octadecene. The authors have demonstrated as much as 40 g of monodisperse IONPs generated without any size-selection process in a single reaction. [89] On the other hand, the inductive heating (IH) method for the synthesis of colloidal nanomaterials achieves high heating rates (100–200

°C/s), thus producing similar outcomes as expected for hot-injection methods.[38,65,96] This methodology relies on a specialized IH reactor with steel balls placed inside where the reactor sits within an induction coil that rapidly heats the steel balls producing a boiling solvent and decomposition of precursor molecules. The boiling point of the solvent can be used as built-in temperature control for achieving various final temperatures without the need for annealing and reflux. Since the glass reactor itself is not heated, the temperature of the apparatus can drop quickly following the heat-up process, allowing the synthesis of very small nanomaterials or proto nanocrystals. Here, we have explored the use of IH for IONP synthesis proving the techniques' ability to control size and size distribution. In addition, the use of heated steel balls allows creating a reductive environment to reduce oxygen contamination for the preparation of oxygen-sensitive nanomaterials such as iron, as shown in **Chapter 4**

From the synthesis point of view, an important consideration is to prepare nanoparticles (NPs) in shorter reaction times, avoiding aging, and annealing. The motivation for this work comes from the technological need for the rapid single-step, one-pot synthesis of monodisperse and uniform colloidal IONPs using a solid precursor, therefore extending the range of precursors that can be used in the synthesis of monodisperse and uniform IONPs. In this paper, we demonstrate a rapid, relatively safer, and single-step alternative approach to synthesize IONPs within seconds *via* the IH technique. Moreover, we report the phase pure synthesis of γ-Fe_2O_3 NPs from a solid precursor, acetylferrocene which avoids the use of toxic and expensive organometallic compounds like iron pentacarbonyl precursor. To the best of our knowledge, the use of solid precursors for the preparation of IONPs *via* IH has not been reported. The size, magnetic behavior, and crystallinity of the synthesized IONPs using different precursors and solvents at different reaction times are studied. The resulting NPs were γ-Fe_2O_3 NPs confirmed by high-resolution transmission electron microscopy (HRTEM) and powder X-ray diffraction (PXRD) patterns. The average size of the synthesized IONPs ranges from 3 to 11 nm in diameter. Importantly, the size of IONPs is dependent on the reaction time and type of the solvent used. Considering benefits over conventional methods, this method can be considered simple, safer, and has the potential to provide an industrial-level scale-up synthesis.

3.2 Materials and methods

3.2.1 Chemicals

Oleylamine (70%) and trioctylamine (98%) were purchased from Sigma-Aldrich. All solvents were dried and degassed via boiling under a vacuum before use. Iron pentacarbonyl ($Fe(CO)_5$, >99.99%) was also purchased from Sigma-Aldrich and stored inside a nitrogen-filled glovebox. Acetylferrocene was purchased from STREM Chemicals. Methanol, ethanol, chloroform, acetone, and toluene were purchased from Fischer Scientific (ACS grade).

3.2.2 Method of synthesis

The synthesis method for IONPs was based on literature with some modifications.[70] The setup for the inductive heater and reactor with precursor mix is the same as that of previously reported work by Chikan et al. and Luo et al.[38,65] Briefly, in this synthesis, iron pentacarbonyl $Fe(CO)_5$ is used as precursor, and oleylamine (OA) and trioctylamine (TOA) are used as solvents. All of the precursors and solvents were mixed inside nitrogen (N_2)-filled glovebox. In the N_2-filled glovebox, the stock solution was prepared by stirring the mixture until the precursor dissolved into the solvent resulting in a yellowish solution. Then, the reactor was filled with steel balls (25.92 g, Bearing-Quality E52100 Alloy Steel, Hardened Ball, 1/8″ diameter) and transported to the glovebox. Next, 4 mL of 0.8 M precursor was transferred from the stock solution to the reactor. Following this, the reactor was transported to the inductive heater and connected to tubing, which maintains an argon atmosphere throughout the reaction. Then, the reaction mixture was heated in a standard 7 kW inductive heater set at minimum power for 5, 7, 10, and 14 s to see the change in size, crystallinity, and magnetic behavior of synthesized IONPs using varying reaction times, solvents, and precursor molecules. The yellowish solution turns darker black with increasing reaction time, indicating the formation of IONPs.

For a typical synthesis using acetylferrocene, the stock solution was prepared by stirring the mixture of acetylferrocene with the solvent (0.8 M) for 24 hours. The reddish solution turns darker black with increasing reaction time indicating the formation of IONPs. The yellowish solution turns darker black with increasing reaction time, indicating the formation of IONPs. The synthesized NPs were cooled to room temperature, then isolated by centrifuging using various solvents. IONPs synthesized using OA were isolated by centrifuging with methanol (~20–25 mL) at 8000 rpm for 10 min followed by sonication. This process was repeated over three cycles. The colorless supernatant was discarded, and the precipitated NPs were then dispersed in small quantities of toluene (3–4 mL) for glovebox storage until further use. IONPs synthesized using TOA were isolated by centrifuging with ethanol (~20–25 mL) at 8000 rpm for 10 min and repeated for a total of two cycles followed by sonication between each cycle. Then, 2–3 mL of OA was added for ligand transfer, washed with methanol for two cycles, sonicated between cycles, and dispersed in small quantities of toluene (3–4 mL) for glovebox storage until further use. Representative steps of the reactor preparation, product formation, and purification are shown in **Figure 3.1.**

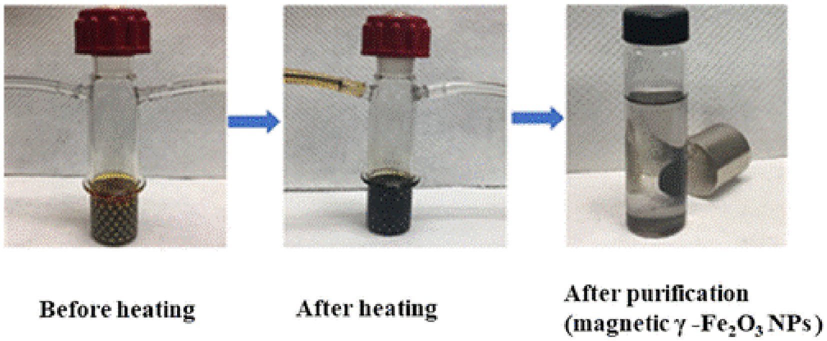

Figure 3.1 Inductive heating reactor filled with the precursor and the solvent (left), the same reactor after the reaction (middle), and magnetic IONPs after purification (right).

3.2.3 Characterization of IONPs

The size and surface morphology of IONPs were analyzed using a transmission electron microscope (TEM) FEI Technai G2 spirit Bio TWIN. The elemental composition of IONPs was measured by energy dispersive spectrum (EDS) using an energy dispersive X-ray analysis (EDAX) detector. The crystal structure of IONPs was analyzed by high-resolution transmission electron microscopy (HRTEM) in an FEI Tecnai F 20X transmission electron microscope at an electron acceleration voltage of 200 kV.

High-resolution transmission electron microscopy (HRTEM) was performed at the University of Kansas's Microscopy and Analytical Imaging (MAI) facility with an FEI Tecnai F 20× transmission electron microscope at an electron acceleration voltage of 200 kV. The TEM samples were prepared by agitating the nanoparticle solution in an ultrasonic bath for 10 min. Five microliters of the sample were placed onto a copper mesh grid with a lacey carbon film. The wet grids were air-dried for several minutes prior to being examined under TEM. The particle size and morphology were examined by bright-field and dark-field scanning transmission electron microscopy (STEM). High-resolution images were captured using a standardized, normative electron dose and a constant defocus value from the carbon-coated surfaces. Results were analyzed using TEM Imaging and Analysis (Thermo Fischer Scientific Company, Waltham, MA). The boundary of each measured domain is indicated with red lines (presented in the Supporting

Information). The lattice plane of each measurement is shown with red lines along the lattice. Measurements were made by the TIA software's diffractogram and verified via calculating the lattice spacing from the Fourier transform of the region. The white labels beside each measured crystal lattice indicate the lattice spacings for the respective lattice. The acquired lattice spacings of each sample were then compared with reference data supported by the Crystallography Open Database to characterize the sample by chemical composition and space group identification. After characterization, Miller indices and space groups were included alongside the lattice spacing measurements.

3.3 Results and discussions

IONPs were synthesized at atmospheric pressure with various heating times, precursors, and solvents to explore how nanoparticles are formed during IH and determine the level of size and size distribution that can be easily achieved under the operating conditions of the inductive heater. Our goal was to focus on short-term heating effects to explore the impact of the heating rates on nanoparticle formation. Due to the rapid heating time of the inductive heater, the solvent temperature quickly rises until it reaches the boiling point of the solvent. The final temperatures of the solution are determined by the boiling point of the solvent, which acts as built-in temperature control during synthesis. Here, we utilize solvents such as oleylamine (Tbp = 350 °C), and trioctylamine (Tbp = 367 °C). In addition, we demonstrate the use of a high concentration of traditional hot-injection precursors such as $Fe(CO)_5$. The concentrations of $Fe(CO)_5$ are almost 44 times higher here than typically used in literature for typical hot-injection methods.[85] This allows the exploration of new synthesis regimes not accessible by the hot-injection method, which could result in exotic structures (not demonstrated here). While in many cases there is an optimal ratio of the solvent to the precursor, the IH technique can achieve these higher concentrations, which would potentially lead to high supersaturation concentrations desirable for the separation of nucleation and growth steps.

3.3.1 Synthesis of IONP from $Fe(CO)_5$ in oleylamine and trioctylamine

The synthesis of IONPs from $Fe(CO)_5$ in the OA solvent is one of the most common combinations used in the typical hot-injection method.[97] The effect of the heating time *via* IH is shown in **Figure 3.2.** The heating time can be easily varied from 1 to 10 s, but beyond this period, the solvent rapidly boils off preventing longer synthesis times. To further increase the exposure of the solution to high temperatures, two times 7 s heating was used with a 2 min break between the additional heating. The resulting sizes of the synthesized IONPs range from 3 to 11 nm, which is dependent on the reaction time and type of the solvent used in synthesis. Although the reaction is performed under argon, the particles are exposed to oxygen during the separation and purification step. The size of IONPs increases from 3.7 ± 0.6 to 6.6 ± 0.7 nm as the reaction time increases from 5 to 7 s. Surprisingly, the size decreases to 5.1 ± 1.3 nm when the reaction mixture was heated to 10 s, which is likely due to the high supersaturation resulting in increased nucleation rates. The fast nucleation rate depletes the precursors from the solution resulting in a smaller average size of the NPs (but larger yield). When the reaction is performed in two steps by heating the reaction mixture for 7 s twice with a break between heating cycles, the size increased to 7.3 ± 1.4 nm, as shown in **Figure 3.2 (D, H)**.

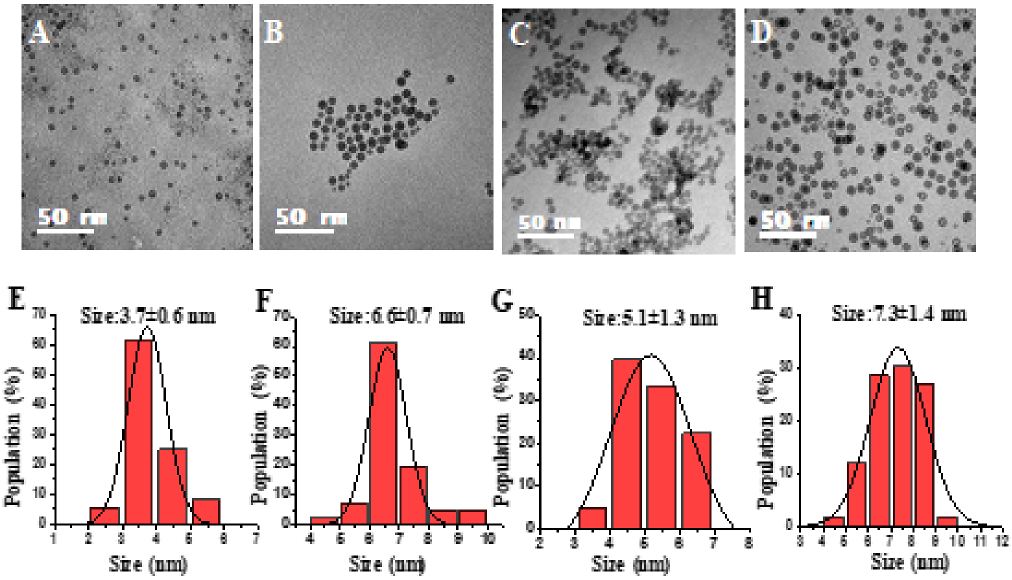

Figure 3.2 Transmission electron microscopy (TEM) images of IONPs produced using 0.8 M Fe $(CO)_5$ and OA at different reaction times (A) 5 s, (B) 7 s, (C) 10 s, and (D) 14 s (7 + 7 s). (E)–(H) are the particle size distribution plots, respectively.

As the reaction time is increased, the crystallinity of the synthesized nanoparticles changed from amorphous to highly crystalline particles, as shown in **Figure 3.3.** The HRTEM images of IONPs **(Figure 3.3 A–C)** indicate (032), (117), and (022) lattice planes of γ-Fe_2O_3 nanoparticles, respectively. These lattice planes are consistent with literature values.[98,99] This is supported by lattice spacing data from the crystallography open database (COD), as well as density functional theory (DFT) calculations as reported by Grau-Crespo et al. While comparing γ-Fe_2O_3 and α-Fe_2O_3 (hematite), diffraction patterns from the COD, show that γ-Fe_2O_3 has characteristic peaks resulting from 2.95, 3.30, and 3.40 Å lattice spacing, whereas α-Fe_2O_3 does not. The HRTEM analysis yields several lattice spacing measurements of 2.95, 3.30, and 3.40 Å, indicating the material must be in the γ phase.[99] It is also observed that with the increase in reaction time, IONPs changed from multidomain to a single domain.

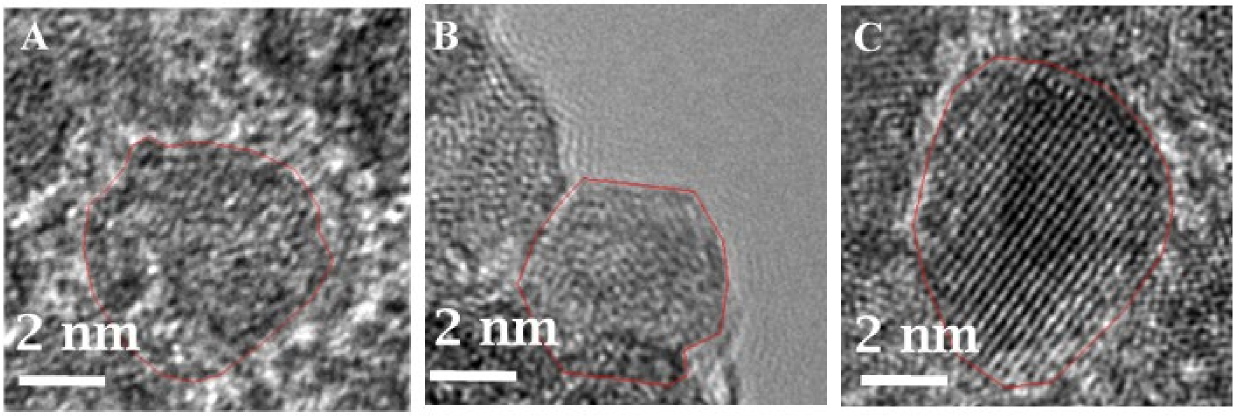

Figure 3.3 High-resolution TEM (HRTEM) images of IONPs produced using 0.8 M $Fe(CO)_5$ and OA at different reaction times (A) 7 s, (B) 10 s, and (C) 14 s (7 + 7 s), indicating (032), (117), and (022) lattice planes of γ-Fe_2O_3 nanoparticles, respectively.

Next, the impact of the monomer concentration on the NP size and size distribution is investigated. The concentration of the monomer was increased from its initial 0.8 to 3.35 M and to 7.5 M that is about 10 times higher than typically used in hot-injection synthesis methods. The average size of IONPs almost doubled after a short period (5 s) of heating time. When the concentration of the precursor molecule is increased by almost four times **(Figure 3.4 C)**, then crystalline nanoparticles were formed even while heating for only 5 s.

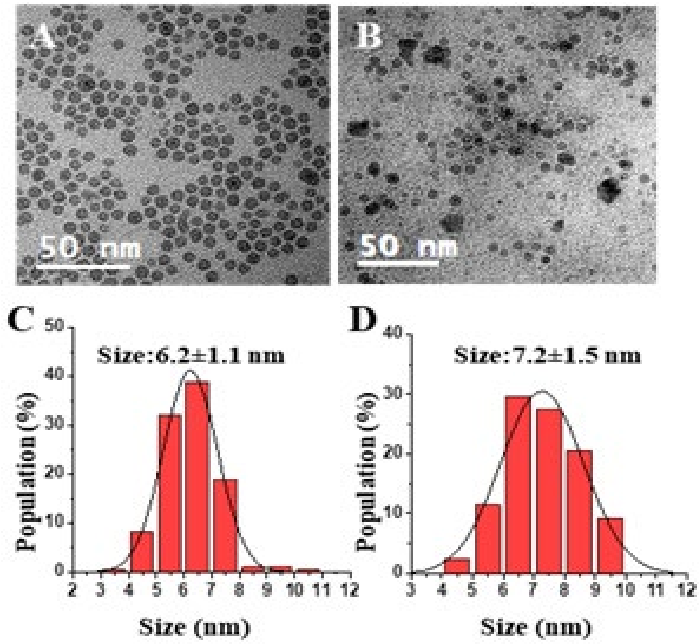

Figure 3.4 TEM images of IONPs produced using 3.35 M $Fe(CO)_5$ and OA at different reaction times (A) 5 s and (B) 10 s. (C) and (D) are the particle size distribution plots, respectively.

The PXRD analysis (**Figure 3.S1**, supporting information) shows the mixture of peaks for maghemite and hematite, which is probably due to the higher concentration of the available oxygen during and post-synthesis purification.[99,100] The increase in size was not so significant as the concentration of the precursor was increased from 3.35 to 7.5 M **(Figure 3.5 A, B)** when the precursor is increased from 0.8 to 3.35 M. The result is not surprising since the nucleation is a stronger function of the supersaturation than the NP growth under diffusion-limited growth conditions.[38] The excess decomposition products from the precursors are likely to interfere with the monomer followed by the decomposition and reduce the available ligands/monomer, which would lead to reduced size distribution as shown below for the higher concentration data.[38,65] The IH method allows exploring synthesis conditions at higher precursor concentrations since a larger portion of the reaction mixture is held above the decomposition temperature of the precursors.[92,97,101]

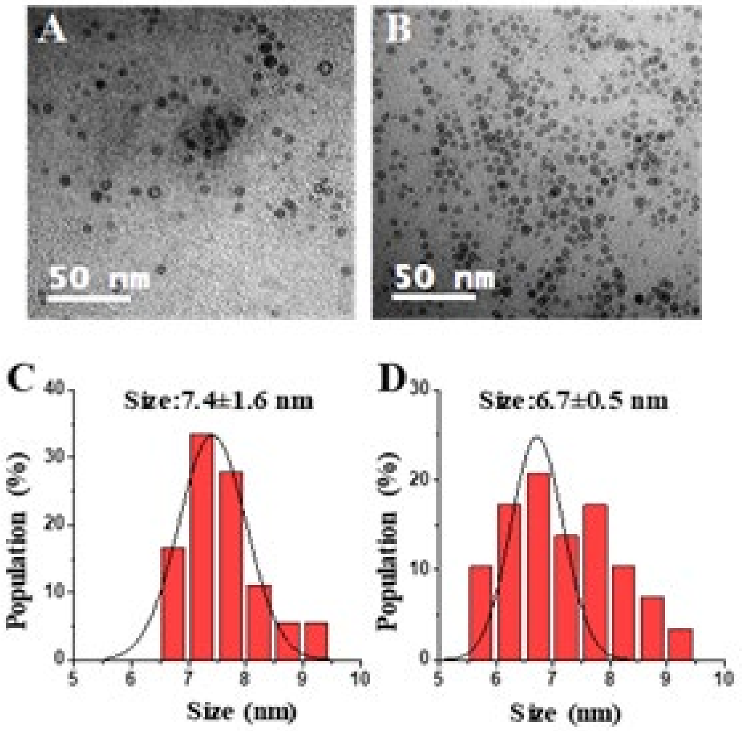

Figure 3.5 TEM images of IONPs produced using 7.5 M $Fe(CO)_5$ and OA at different reaction times (A) 5 s and (B) 10 s. (C) and (D) are the particle size distribution plots, respectively.

A similar experiment was performed using the same precursor under identical conditions of concentration and reaction time but with the different solvent having a higher boiling point than that of oleylamine as shown in **Figure 3.6.** As shown in **Figure 3.6**, larger-sized NPs (5.0 ± 1.3 nm as opposed to 3.7 ± 0.6 nm) were formed using $Fe(CO)_5$ and trioctylamine vs oleylamine even in a shorter healing time (5 s). This increase in size is attributed to the higher boiling point of trioctylamine (bp = 367 °C) compared to oleylamine (bp = 350 °C). Most likely the trioctylamine lowered the decomposition rate of $Fe(CO)_5$; hence, larger nanoparticles were formed as compared to the use of oleylamine in a shorter heating time. The size increased as the heating time increased from 5 to 7 to 10 s. The seed growth method is also used in this experiment, and it resulted in a larger size of NPs (7.1±1.5 nm, **Figure 3.6 D, H**) as compared to the size of nanoparticles produced after heating only 7 s.

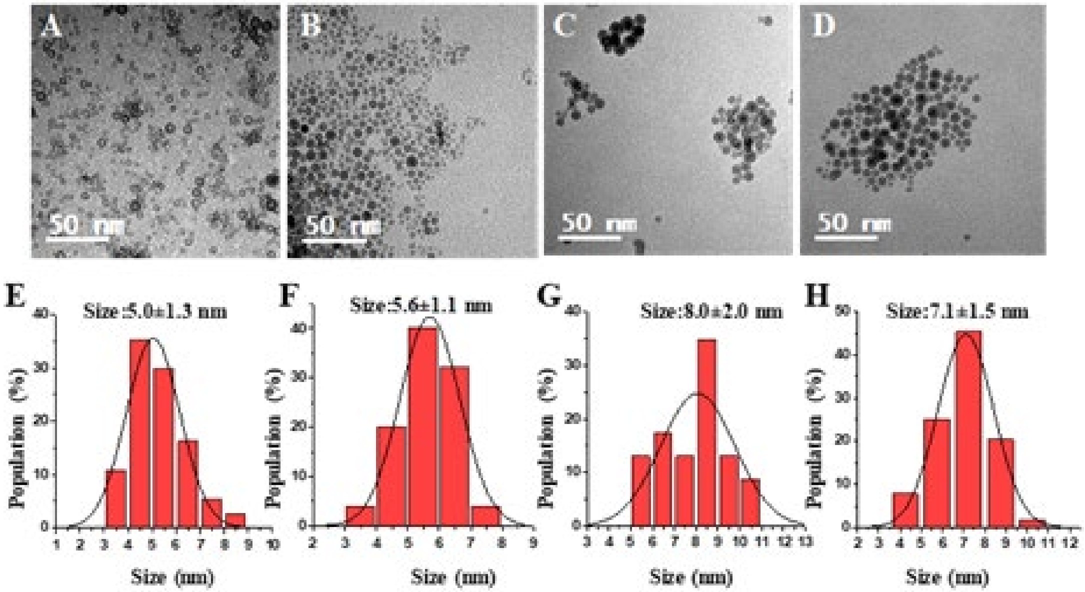

Figure 3.6 TEM images of IONPs produced using 0.8 M $Fe(CO)_5$ and TOA at different reaction times (A) 5 s, (B) 7 s, (C) 10 s, and (D) 14 s (7 + 7 s). (E)–(H) are the particle size distribution plots, respectively.

Park et al. have reported the ultra-large-scale synthesis of 22 nm-sized IONPs using trioctylamine.[83] Thus, synthesized IONPs were prepared by mixing iron oleate complex, oleic acid, and trioctylamine by ramping 340 °C at 3.3 °C/min under reflux for 1 h.[83] However, their approach requires a longer reaction time and multiple precursors for synthesis. In contrast, the IH method used here produced IONPs using a single precursor and ultrashort reaction time. **Figure 3.7 A–C** is the HRTEM image of corresponding NPs indicating (222), (025), and (026) lattice planes of γ-Fe_2O_3 nanoparticles.[99]

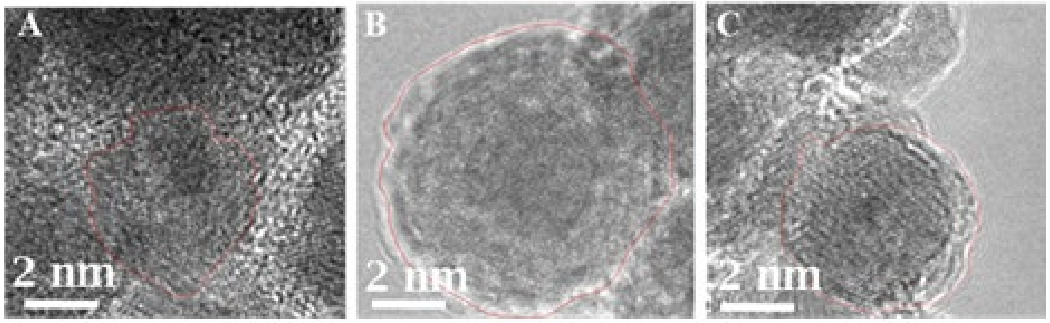

Figure 3.7 HRTEM images of IONPs produced using 0.8 M $Fe(CO)_5$ and TOA at different reaction times (A) 7 s, (B) 10 s, and (C) 14 s (7 + 7 s), indicating (222), (025), and (026) lattice planes of γ-Fe_2O_3 nanoparticles, respectively.

3.3.2 Comparison of magnetic properties of IONPs

The magnetic properties of IONPs and iron NPs were studied using a superconducting quantum interference device (SQUID). Tadic et al. have reported that magnetic properties are directly dependent on size, size distribution, shape, and orientation of IONPs.[102–106] In their work, they reported that hematite with a size around 10 nm produced blocking temperature, and particles with a size around 20 nm produced Morin transition.[102] Furthermore, they have reported the saturation magnetization (Ms) of hematite around 1.93 emu/g.[102] In another study, they concluded that shape anisotropy affected the coercivity of hematite NPs.[105] They observed that ellipsoid three-dimensional (3D) superstructures of hematite are much higher than those for irregularly shaped hematite NPs.[105] Similarly, physical orientation can be used to achieve either superparamagnetic or ferromagnetic maghemite NPs.[104] Superparamagnetic properties in NPs are attributed to the random orientation of particles, whereas ferromagnetism is related to parallel orientation of particles.[103–105] **Figure 3.8** shows the magnetization (emu/g) vs magnetic field, H (Oe) graph for IONPs obtained using $Fe(CO)_5$, and different solvents at different reaction times, at room temperature (298 K).

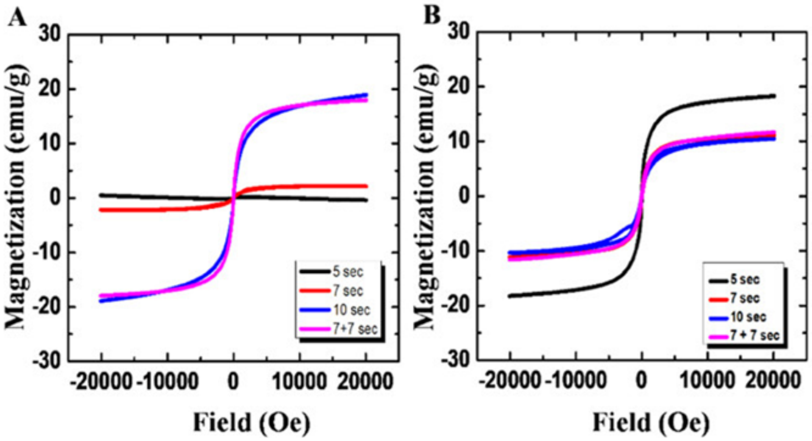

Figure 3.8 Magnetization *vs* magnetic field plot for IONPs produced using 0.8 M (A) $Fe(CO)_5$ and OA (B); $Fe(CO)_5$ and TOA at 5, 7, 10, and 7 +7 s heating time.

Figure 3.8 shows that IONPs with a size of 3.7 ± 0.6 nm have almost zero magnetization. We have observed that with the increasing size from 3.7 ± 0.6 to 7.3 ± 1.4 nm, the shape of M–H loops for IONPs does not change appreciably, but their Ms increases from 0 to 20 emu/g. This value is close to Ms of 11 nm-sized γ-Fe_2O_3 synthesized via thermal decomposition of $Fe(CO)_5$ as reported in the literature.[85] However, it should be noted that the obtained Ms values are much smaller than those expected considering the bulk Ms values (74 emu) of γ-Fe_2O_3.[107] This could be due to the presence of magnetically disordered atoms at the surface of the NPs, which is common in smaller magnetic NPs.[108] As the particle size increases, the particles change from multidomain to a single domain that can be seen from HRTEM images discussed in **Figures 3.3 and 3.7**, and the value of M_s also increases. Furthermore, a similar trend is observed in **Figure 3.8 B**. The increase in M_s with an increase in size is attributed to a decrease in a surface spin in binding ligands oleylamine, trioctylamine, surface with the increase in particle size.[109]

3.3.3 Synthesis of γ-Fe_2O_3 from acetylferrocene

In this section, we have explored the use of a solid precursor acetylferrocene for the synthesis of IONPs. The goal is to demonstrate the diverse range of precursors that can be used to IH to prepare NPs. The γ-Fe_2O_3 NPs were synthesized with a single solid precursor (acetylferrocene) and two different solvents (oleylamine and trioctylamine) at various reaction times. The comparative study on the size, crystallinity, and magnetization of γ-Fe_2O_3 with the change in reaction time and boiling point of solvent is demonstrated. The morphology and structure of the pure γ-Fe_2O_3 NPs are characterized by TEM. The particle size distributions, obtained from TEM micrographs, are shown in **Figure 3.9** and the corresponding mean particle sizes obtained from the Gaussian fit of the histograms are also indicated in **Figure 3.9 E-H**. The histogram demonstrates that as the reaction time increases the size of NPs increases. The reason behind this trend is the nucleation and growth of NPs. Longer reaction time provides more time for the growth of NPs yielding larger sizes. These particle size distribution starts to narrow as the heating time increase from 5 s to 14 s probably due to higher supersaturation as the precursor decomposes. The size of the formed IONPs is close to that reported in the literature which discusses the solventless synthesis of IONPs through thermal decomposition of acetylferrocene and malic anhydride.[95]

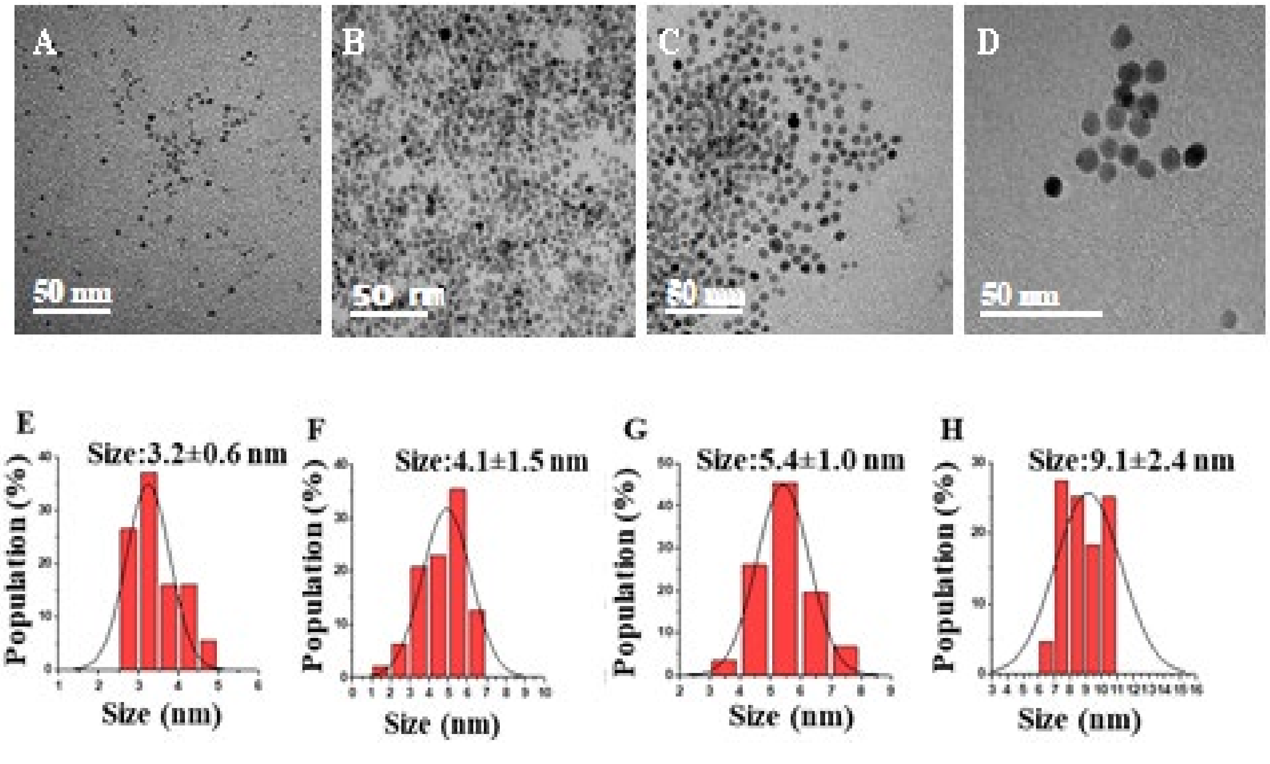

Figure 3.9 TEM images of γ-Fe_2O_3 NPs produced by using 0.8 M acetylferrocene and OA at different reaction times (A) 5 s, (B) 7 s, (C) 10 s, and (D) 14 s. (E–H) are the particle size distribution plots, respectively.

The increase in the heating times from 5 s to 14 s increases the size of γ-Fe_2O_3 NPs from 3.2 ± 0.6 to 9.1 ± 2.4 nm. This is because a longer heating time promotes a faster nucleation rate resulting in larger-sized NPs. Furthermore, as the reaction time is increased, the crystallinity of the synthesized nanoparticles changed from amorphous to highly crystalline particles, as shown in HRTEM images in **Figure 3.10**. HRTEM measurement shows the lattice spacing measurement of 2.93 **(Figure 3.10 A),** 2.95 Å, **(Figure 3.10 B)**, 3.30 Å **(Figure 3.10 C)**, and 3.40 Å **(Figure 3.10 D). Figure 3.10 A** shows (222) lattice plane, **Figure 3.10 B** shows (026), (222) lattice planes, **Figure 3.10 C** shows (026) lattice planes, and **Figure 3.10 D** shows (112) and (222) lattice planes of γ-Fe_2O_3 NPs which indicates that these particles are multidomain. These lattice planes are consistent with literature values.[98,99] This result is consistent with the lattice spacing data from the crystallography open database (COD) and density functional theory (DFT) calculations reported by Grau-Crespo et al.[99]

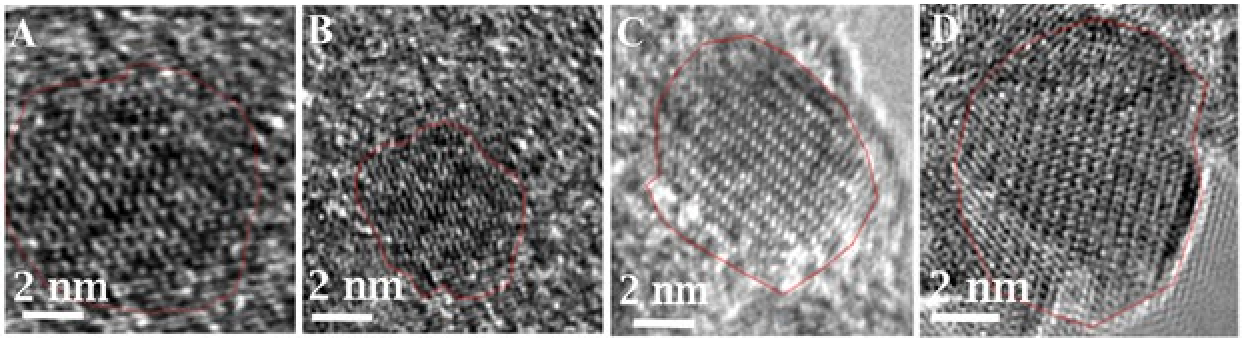

Figure 3.10 HRTEM images of γ-Fe_2O_3 NPs produced by using 0.8 M acetylferrocene, and oleylamine at different reaction times (A) 5 s, (B) 7 s, (C) 10 s, and (D) 14 s. (A) indicates (222) lattice planes, (B) indicates (026), (222) lattice planes, (C) indicates (026) lattice planes, and (D) indicates (112), (222) lattice planes of γ-Fe_2O_3 NPs.

The PXRD patterns are used to determine the structural parameter of the sample. In the corresponding PXRD spectra of **Figure 3.11**, the diffraction peaks at 2θ correspond to (011), (013), (222), (113), and (400) planes which reveal phase pure γ-Fe_2O_3 NPs with cubic crystal system (ICDD#39-1346). These values are closely in agreement with the previously reported work in literature.[99,110–113]

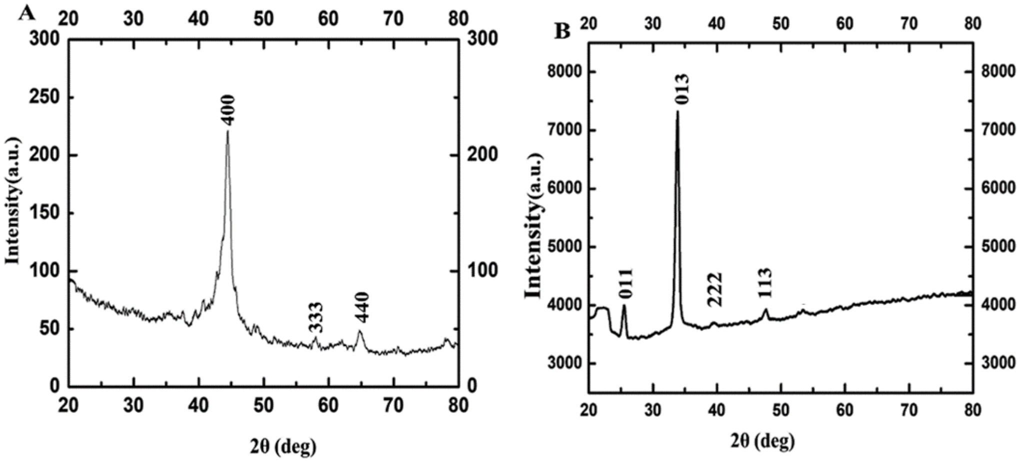

Figure 3.11 PXRD of γ-Fe_2O_3 NPs synthesized using 0.8 M acetylferrocene and OA at A) 10 s, and B) 14 s heating.

Figure 3.12 shows the magnetization (emu/g) vs magnetic field, H (Oe) graph for IONPs obtained by using acetylferrocene and OA, at room temperature (298 K). **Figure 3.12** shows that that γ-Fe_2O_3 NPs showed almost zero magnetization with heating 5 s but the saturation magnetization reaches almost 20 emu/g with the increase in heating time. The increase in M_s with an increase in size is attributed to a decrease in a surface spin in the oleylamine surface with the increase in particle size.[114] This shows that these particles are superparamagnetic at room temperature.[37,106,114]

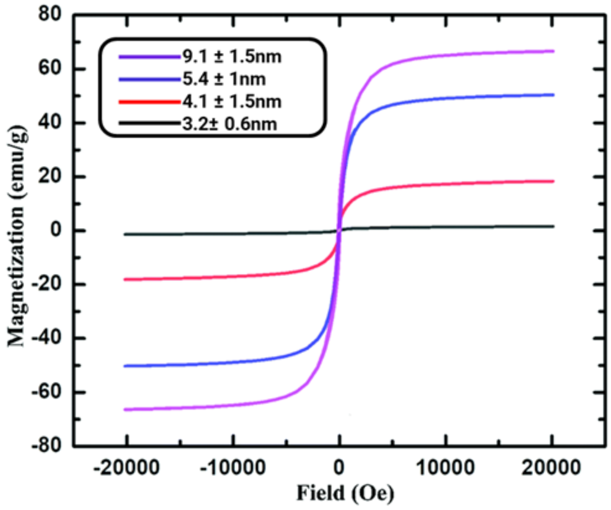

Figure 3.12 Magnetization *vs.* magnetic field plot for γ-Fe_2O_3 NPs produced using 0.8 M acetylferrocene and oleylamine 5 s, 7 s, 10 s, and 14 s heating time.

The saturation magnetization of these particles is very less as compared to that of IONPs synthesized using $Fe(CO)_5$ and atmospheric microwave plasma.[115] It can be noted from **Figure 3.12** that, with the increase in the size from 3.2 ± 0.6 nm to 9.1 ± 2.4 nm, the M_s value also increases from 0 to 70 emu/g. The increase in M_s value with an increase in the size of NPs could be due to the presence of magnetically disordered atoms at the surface of the NPs which is common in smaller magnetic NPs.[108,114] On the other hand, these values are less as compared to the M_s value of bulk γ- Fe_2O_3 (76 emu/g), which is probably attributed to nanoscale dimension and surface effect.[107,116,117]

Similarly, another set of experiments was performed using 0.8 M acetylferrocene and trioctylamine (T_{bp}=367 °C) instead of oleylamine (T_{bp}=350° C) as a solvent to see the effect of the boiling point of solvent on the size of NPs. As shown in **Figure 3.13**, a similar trend in the size was observed with the increase in reaction time. However, the increase in size was very minimal with the increase in the boiling point of solvent under identical conditions of concentration and reaction time. Furthermore, thus synthesized nanoparticles were of very poor crystallinity as can be seen in **Figure 3.14** as compared to those synthesized using acetylferrocene and oleylamine (**Figure 3.10**). To the best of our knowledge, there is not any literature report regarding the

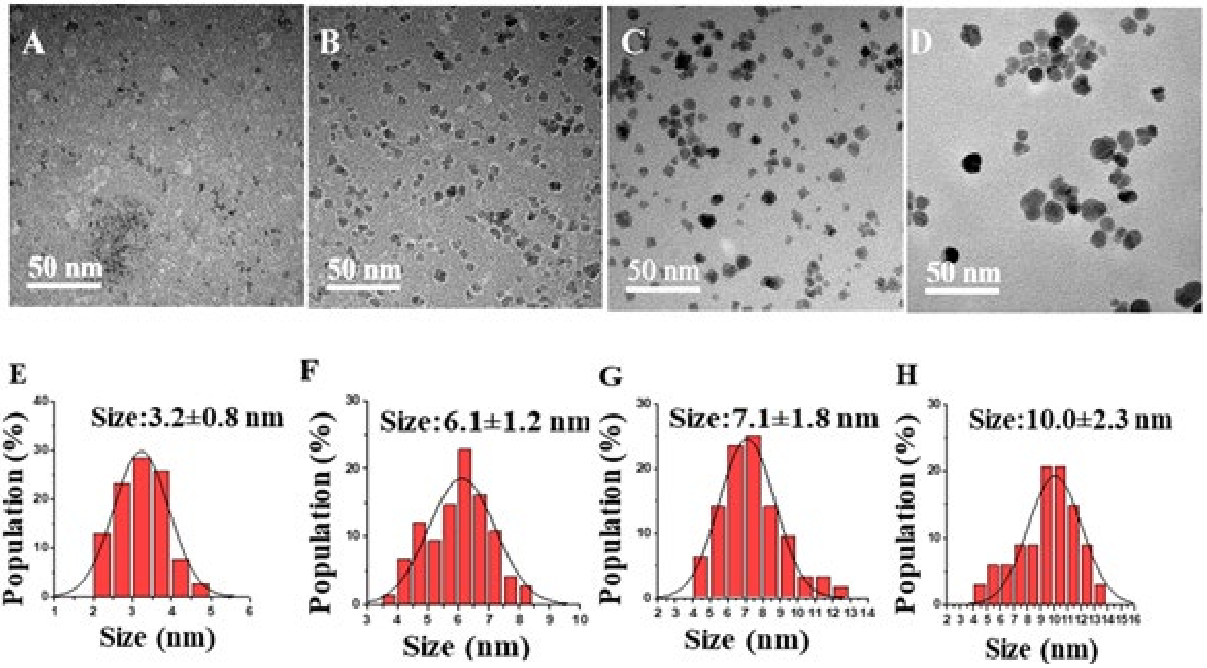

Figure 3.13 TEM images of IONPs produced by using 0.8 M acetylferrocene and trioctylamine at different reaction times A) 5 s, B) 7 s, C) 10 s, and D) 14 s. (E, F, G, and H) are the particle size distribution plots, respectively.

synthesis of γ-Fe_2O_3 NPs using acetylferrocene and trioctylamine, this approach could be a potential alternative way to make γ- Fe_2O_3 NPs using single precursor and single solvent.

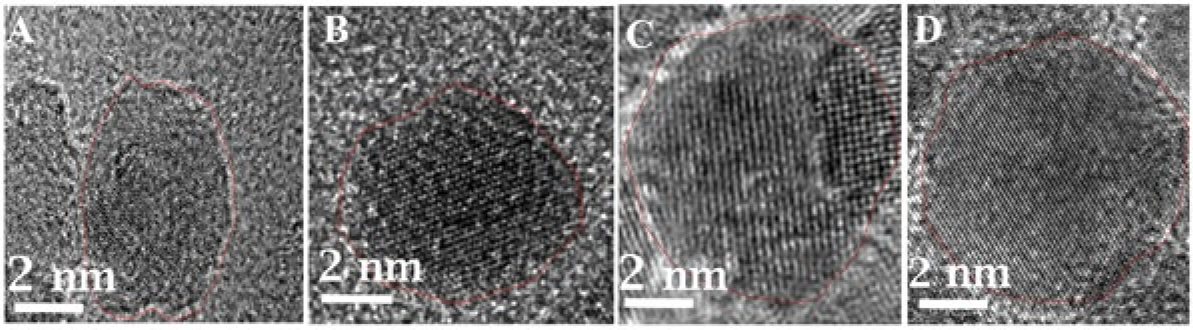

Figure 3.14 HRTEM images of γ-Fe_2O_3 NPs produced by using 0.8M acetylferrocene, and TOA at different reaction times A) 5 s, B) 7 s, C) 10 s and D) 14 s indicating (115), (016), and (022) lattice planes of γ-Fe_2O_3.

The HRTEM images of these nanoparticles confirm the gamma phase of Fe_2O_3. In **Figure 3.14**, HRTEM images of these particles indicate (115), (016), and (022) lattice planes of γ-Fe_2O_3. These values are closely in agreement with the previously reported work.[98,99] In the corresponding PXRD spectra of **Figure 3.14** as shown in **Figure 3.15**, the diffraction peaks at 2θ correspond to (012), (104), and (024) planes which reveal phase pure γ-Fe_2O_3 NPs with cubic crystal system (ICDD#89-2810). These values are closely in agreement with the previously reported work in literature.[118]

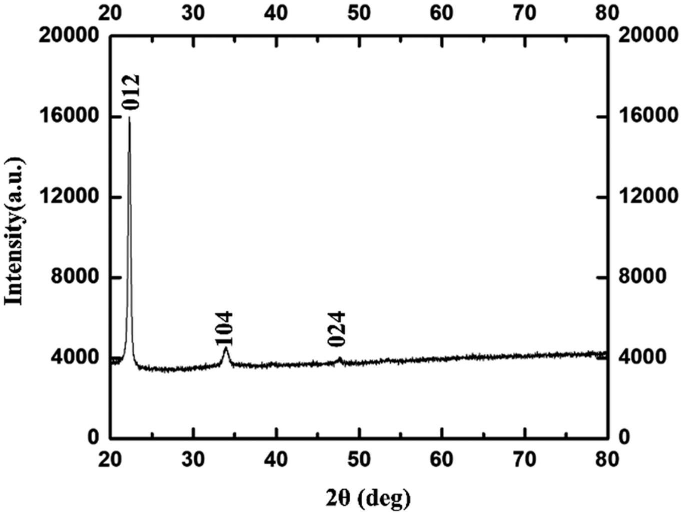

Figure 3.15 PXRD of γ-Fe_2O_3 NPs synthesized using 0.8 M acetylferrocene and trioctylamine at 14 s heating.

3.4 Conclusion

The rapid IH approach used in this study provides a simple, facile, and inexpensive method for direct one-pot synthesis of IONPs. This method offers a great advantage over traditionally established HI as it can be used in the size-controlled synthesis of phase pure γ-Fe_2O_3 using a solid precursor, acetylferrocene. These NPs are in the size of 3–11 nm. The increase in heating times increased the size and magnetization of NPs. The result reveals that the IH method is an efficient method to produce IONPs with size control and it could potentially replace the traditional HI method. We anticipate that this improved, one-pot IH method easily be scaled up to a gram scale.

Chapter 4 - Colloidal synthesis and characterization of air-stable iron nanoparticles

***Chapter 4**, in full, is a reprint of the material from **ACS Omega**, 2020, https://doi.org/10.1021/acsomega.0c02793 with some modification.*

Abstract

The synthesis of colloidal iron nanoparticles has been one of the most attractive goals in magnetic nanomaterial research in past decades due to their superparamagnetic property with a high magnetic moment density thereby allowing diverse applications in catalysis, bioseparation, biosensing, drug delivery, and biomedical imaging. Despite these outstanding applications, Fe nanoparticles have been somewhat shadowed as compared to their oxides. The extreme reactivity of finely divided iron, owing to its pyrophoric nature, has traditionally made Fe NPs difficult to study and inconvenient for practical applications. However, traditional methods used to synthesize Fe NPs are mainly limited by stability, dispersibility, large-scale production, and high economical and environmental burden. Therefore, there is an unmet need for the development of an alternative synthetic method, which is simple, rapid, environmentally benign, cost-effective, and provides an opportunity for large-scale production. Aligned towards this direction, herein, we report a very simple, one-pot reaction that gives monodisperse air-stable Fe nanoparticles using the inductive heating (IH) technique. While investigating for an efficient approach to produce air-stable Fe nanoparticle dispersion, we found that decomposition of $Fe(CO)_5$ in 1-octadecane (1-ODE) in argon atmosphere gave monodisperse Fe NPs. The use of steel balls placed inside the inductive heating reactor provided the reductive atmosphere to obtain Fe NPs. To the best of our knowledge, there is no similar report on the production of Fe NPs by the IH method.

4.1 Introduction

Iron is represented by the symbol ‘Fe’ and is found in nature in three different forms i.e., alpha, beta, and gamma.[119] Fe is one of the most abundant transition metals, the fourth-most plentiful element in the earth’s crust. Fe NPs show excellent reactivity with oxygen and water and readily forms oxides as compared to bulk counterparts.[120] The synthesis of colloidal Fe NPs has been one of the most attractive goals in magnetic nanomaterial research in past decades. It belongs to a class of ferromagnetic material with high magnetic moment density (218 emu/g, or 1713 emu/cc) and is magnetically soft.[119,121] Fe NPs in the size range below 20 nm are in the superparamagnetic regime, and their stable dispersions with high magnetic moment are predicted to have important applications in bioseparation, biosensing, drug delivery, and MRI contrast enhancement.[88,122,123] In addition to this, these nanoparticles have a huge potential for different applications including magnetic fluids, a catalyst for carbon nanotube formation, nickel−iron batteries, and catalysts and sorbents for environmental remediation.[124,125] Extensive laboratory studies have demonstrated that nanoscale iron particles are effective for the transformation of a wide array of environmental contaminants such as chlorinated organic solvents, organochlorine pesticides, polychlorinated biphenyls (PCBs), organic dyes, and various inorganic compounds.[126]

Different forms of iron nanoparticles are required depending upon the applications. For example, for Ni−Fe batteries and environmental remediation, nanosized aggregated iron powder is suitable.[125] However, well-dispersed colloidal iron is required for applications in biological systems such as MRI contrast enhancement and biomaterials separation.[119,127] In another important application, carbon nanotubes can be grown on silicon by chemical vapor deposition (CVD) using iron, cobalt, or nickel nanoparticles as catalysts.[128] To prevent interference between nanotubes, especially in the application of field-emission sources, dispersive separation of nanoparticles on the substrate is very important.[123,128] Spin-coating is an economical and convenient method to disperse the nanoparticles on the substrate over a large area and for this, a suspension of agglomerated iron nanoparticles is needed.[129]

Despite these outstanding applications, Fe has been somewhat less explored as compared to its oxides, as well as other metals such as cobalt, nickel, gold, and platinum.[24,88,130] Its reactivity is important in macroscopic applications (particularly rusting) but is a dominant concern at the nanoscale. Finely divided iron has long been known to be pyrophoric, which is a major reason that Fe NPs have not been more fully studied to date.[126] This extreme reactivity has traditionally made Fe NPs difficult to study and inconvenient for practical applications. However, Fe has a great deal to offer at the nanoscale, including very potent magnetic and catalytic properties.[4,119] Some of the recent work in this field appears to be very exciting yet limited by stability, dispersibility, and large-scale production.[14,122,130]

The Fe NPs can mainly be synthesized using the thermal decomposition of iron pentacarbonyl ($Fe(CO)_5$), reductive decomposition of iron(II) bis(trimethylsilyl)amide ($Fe[NSi(CH_3)_3]_2]_2$), and the chemical reduction of iron(III) acetylacetonate ($Fe(acac)_3$) or other iron salts.[1,131–136] Although the small and uniform iron nanoparticles with high purity can be manufactured, however, it is an uneconomical process since the use of elevated temperatures, expensive, and highly toxic precursors. As a result, materials made by the traditional route are not suitable for applications requiring large quantities of iron nanoparticles, such as environmental remediation or nickel−iron batteries. It is well documented that the synthesized particles are extremely reactive on one side, but facile oxidation of the particles gives various iron oxide nanoparticles. Consequently, the syntheses have difficulty in producing stable Fe nanoparticle dispersions, especially aqueous dispersions, for potential biomedical applications.[1,10,124,130,131]

Here, we report an improved, yet very simple, one-pot reaction that gives monodisperse air-stable Fe nanoparticles using the inductive heating (IH) technique. While investigating for an efficient approach to produce air-stable Fe nanoparticle dispersion, we found that decomposition of $Fe(CO)_5$ in 1-octadecane (1-ODE) in argon atmosphere gave monodisperse Fe NPs. The boiling point of solvent i.e., 1-ODE provides the built-in temperature control for the reaction to form the product. The steel balls placed inside the inductive heating reactor provide the reductive atmosphere to obtain Fe NPs. To the best of our knowledge, there is no similar report on the production of Fe NPs by the IH method. We show that by adjusting the heating time, Fe NPs in several size ranges can be obtained.

4.2 Materials and methods

4.2.1 Chemicals

$Fe(CO)_5$ (>99.99%) and 1-ODE (tech. grade, 90%) were purchased from Sigma-Aldrich and stored inside a N_2-filled glovebox. All solvents were dried and degassed via boiling under a vacuum before use. Methanol, ethanol, chloroform, acetone, and toluene were purchased from Fischer Scientific (ACS grade).

4.2.2 Method of synthesis

The synthesis method for IONPs was based on literature with some modifications.[70] The setup for the inductive heater and reactor with precursor mix is the same as that of previously reported work by Chikan et al. and Luo et al.[38,65] Briefly, in this synthesis, $Fe(CO)_5$ is used as precursor, and 1- ODE is used as solvents. The precursor and solvent were mixed inside nitrogen (N_2)-filled glovebox. In the N_2-filled glovebox, the stock solution was prepared by stirring the mixture until the precursor dissolved into the solvent resulting in a yellowish solution. Then, the reactor was filled with steel balls (25.92 g, Bearing-Quality E52100 Alloy Steel, Hardened Ball, 1/8″

diameter) and transported to the glovebox. Next, 4 mL of 0.8 M precursor was transferred from the stock solution to the reactor. The reactor was then transported to the inductive heater and connected to tubing, which maintains an argon atmosphere throughout the reaction. Then, the reaction mixture was heated in a standard 7 kW inductive heater set at minimum power for 5, 7, 10, and 14 s to see the change in size, crystallinity, and magnetic behavior of synthesized IONPs using varying reaction times, solvents, and precursor molecules. The yellowish solution turns darker black with increasing reaction time, indicating the formation of Fe NPs.

The synthesized NPs were cooled to room temperature, then isolated by centrifuging using various solvents. Fe NPs synthesized using 1-octadecane as the solvent was separated by centrifuging with hexane and acetone in a 1: 4 ratio at 8000 rpm for 10 min followed by bath sonication. The NPs underwent three cycles of this process and then they were dispersed in chloroform for glovebox storage. Thus, synthesized NPs were air-stable in ambient conditions for up to one week.

4.2.3 Characterization of Fe NPs

The details of characterization of Fe NPs are the same as for IONPs discussed in **Chapter 3.**

4.3 Result and discussions

Fe NPs were synthesized at atmospheric pressure with various heating times to explore how nanoparticles are formed during IH and determine the level of size and size distribution that can be easily achieved under the operating conditions of the inductive heater. Our goal was to focus on short-term heating effects to explore the impact of the heating rates on nanoparticle formation. Due to the rapid heating time of the inductive heater, the solvent temperature quickly rises until it reaches the boiling point of the solvent. The final temperatures of the solution are determined by the boiling point of the solvent, which acts as a built-in temperature control during synthesis. Here, we utilize 1-ODE (Tbp = 314 °C) solvents.

The effect of the heating time *via* IH is shown in **Figure 4.1**. The heating time can be easily varied from 1 to 10 s, but beyond this period, the solvent rapidly boils off preventing longer synthesis times. To further increase the exposure of the solution to high temperatures, two times 7 s heating was used with a 2 min break between the additional heating. The resulting sizes of the synthesized Fe NPs range from 3 to 11 nm, which is dependent on the reaction time.

It is clearly seen that the NPs size increases from 7.4 ± 2.5 to 9.4 ± 0.7 nm as the reaction time increases from 5 to 7 s. Surprisingly, the size decreases to 9.1 ± 1.3 nm when the reaction mixture was heated to 10 s, which is likely due to the high supersaturation resulting in increased nucleation rates. The fast nucleation rate depletes the precursors from the solution resulting in a smaller average size of the NPs (but larger yield). When the reaction is performed in two steps by heating the reaction mixture for 7 s twice with a break between heating cycles, the size increased to 11.1 ± 2.2 nm, as shown in **Figure 4.1**.

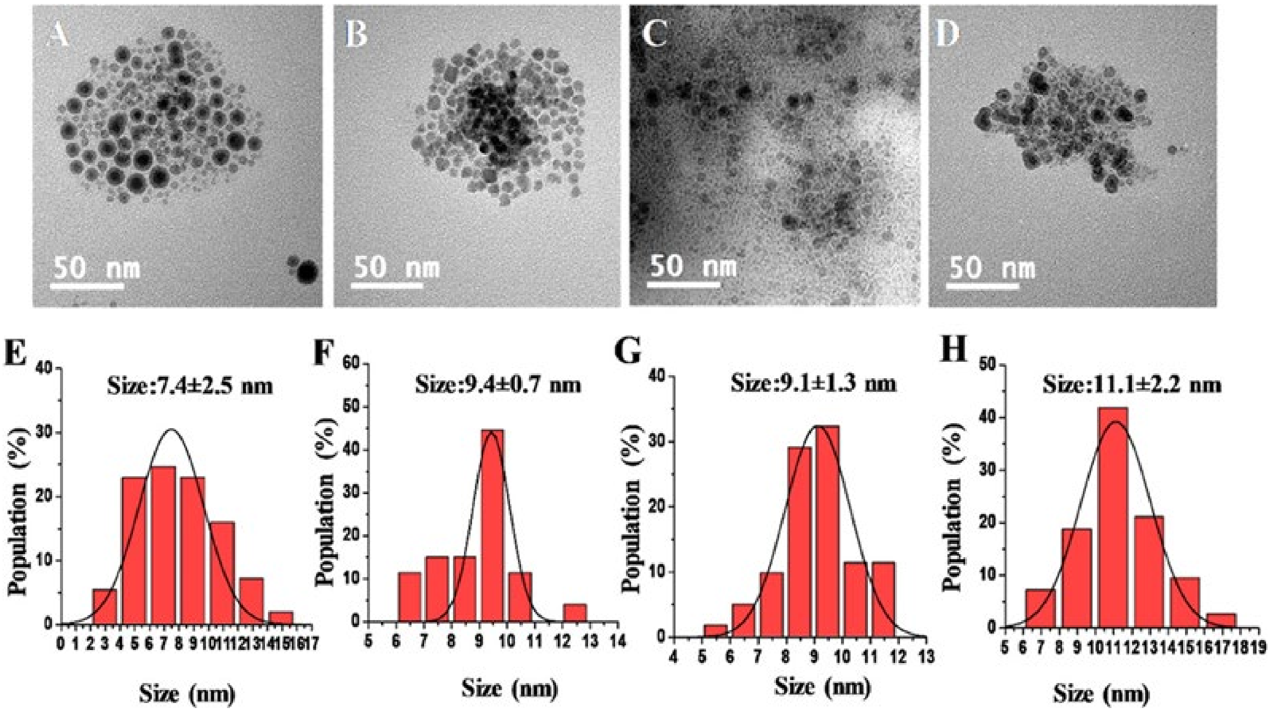

Figure 4.1 TEM images of Fe NPs produced using 0.8 M $Fe(CO)_5$ and 1- ODE at different reaction times (A) 5 s, (B) 7, (C) 10 s, and (D) 14 s (7 + 7 s). (E)–(H) are the particle size distribution plots, respectively.

The HRTEM analysis of these particles shows (011), (011), and (002) lattice planes of iron NPs **(Figure 4.2).**

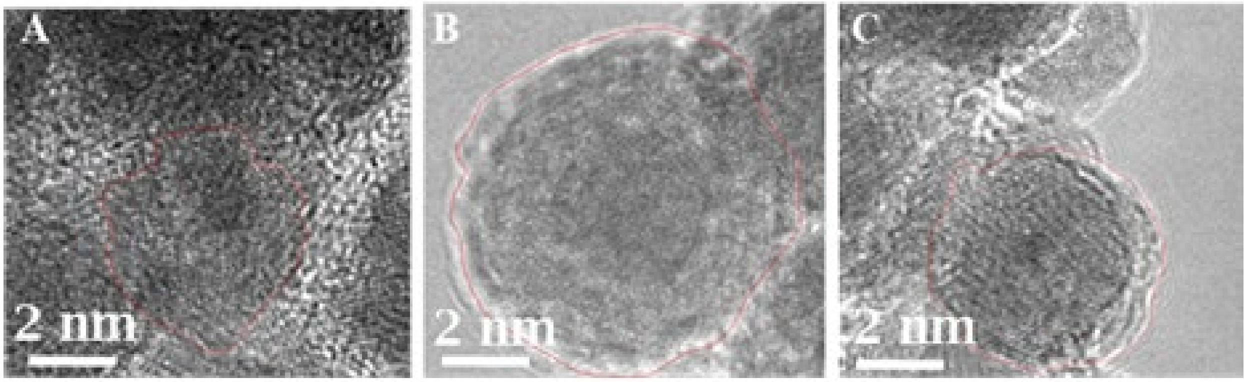

Figure 4.2 HRTEM images of iron NPs produced using 0.8 M $Fe(CO)_5$, and 1-ODE at different reaction times (A) 7 s, (B) 10 s, and (C) 14 s (7 + 7 s), indicating (011), (011), and (002) lattice planes of Fe NPs, respectively.

The PXRD of the NPs can be seen in **Figure 4.3,** the diffraction peaks of 2θ correspond to (011) planes, which confirms the formation of pure iron NPs. Thus, synthesized Fe NPs were heated in an atmospheric oven at 70 °C for a week. Interestingly, the PXRD of these NPs after 1 week also showed diffraction peaks of 2θ corresponding to (011) plane of Fe NPs. This indicates the formation of air-stable iron NPs. This could be explained that 1-octacdecane, being a weaker binding ligand, produced larger-sized NPs. As larger particles have a lower surface-to-volume ratio, they form stable iron NPs instead of oxidizing and forming iron oxides. However, further study is required to support this notion. The crystallinity of iron NPs also changed from amorphous to crystalline with an increase in reaction time (**Figure 4.2**).

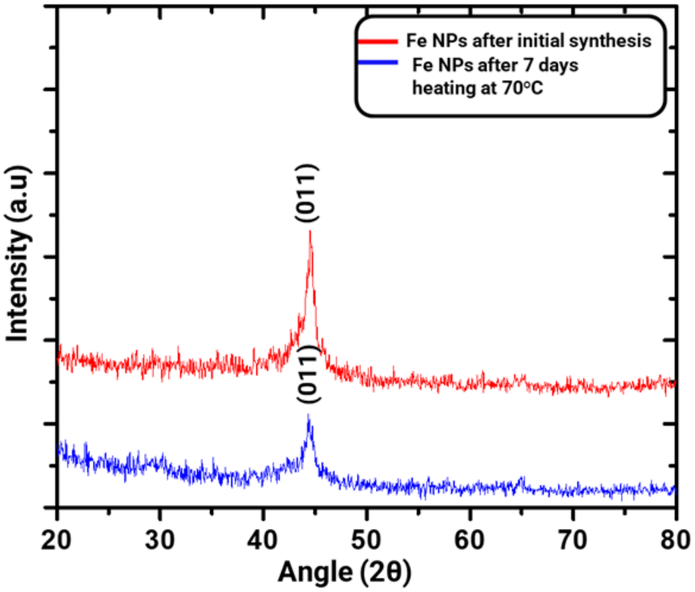

Figure 4.3 PXRD of iron NPs synthesized using 0.8 M $Fe(CO)_5$ and 1- ODE at A) 10 s and B) (7 + 7) s heating time.

The magnetic properties of IONPs and iron NPs were studied using a superconducting quantum interference device (SQUID). Tadic et al. have reported that magnetic properties are directly dependent on size, size distribution, shape, and orientation of IONPs.[102–105] Superparamagnetic properties in NPs are attributed to the random orientation of particles, whereas ferromagnetism is related to the parallel orientation of particles.[116] **Figure 4.4** shows the magnetization (emu/g) vs magnetic field, H (Oe) graph for Fe NPs at different reaction times, at room temperature (298 K) data are summarized in **Table 4.S1** in the Supporting Information.

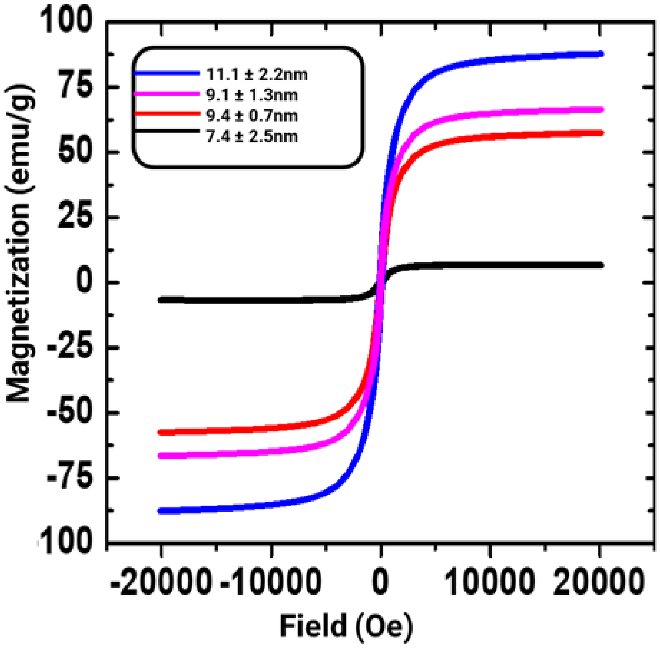

Figure 4.4 Magnetization vs magnetic field plot for Fe NPs produced using 0.8 M Fe (CO)$_5$ and 1-ODE at 5, 7, 10, and 7 +7 s heating time.

As can be seen from **Figure 4.4** shows that IONPs with a size 7.4 ± 2.5 nm have almost 5 emu/g magnetizations. This could be due to the presence of magnetically disordered atoms at the surface of the NPs, which is common in smaller magnetic NPs.[108] We have observed that with the increasing size from 7.4 ± 2.5 to 11.1 ± 2.2 nm, the shape of M–H loops for Fe NPs change appreciably, their Ms increases from 5 to 90 emu/g. The increase in Ms with an increase in size is attributed to a decrease in a surface spin in binding ligands 1-ODE surface with the increase in particle size.[109,137,138] This value is also smaller than bulk iron NPs (221 emu/g), but its data are consistent with the observation from the structural analysis of Fe NPs synthesized using 1-ODE.[103] As the particle size increases, the particles change from multidomain to a single domain that can be seen from HRTEM images discussed in **Figures 4.2**

4.4 Conclusions

A new simple and facile approach have been developed for the preparation of monodispersed air-stable iron NPs by the rapid inductive heating method. The synthesis involved $Fe(CO)_5$ as a precursor and 1-ODE as the solvents. These solvents played the role of binding ligand and reducing agents. The size of the synthesized NPs was dependent on the reaction time. As the reaction time increased, the magnetization of NPs also increased. Also, this method can be used in the synthesis of a range of nanoparticles sizes (as small as 3 nm to as large as 11 nm), Overall, it is expected that the inductive heating method will result in further exploration of the topic due to faster, easier, and safer preparation methodology and could easily be scaled up to a gram scale.

Chapter 5- Colloidal synthesis of air-stable germanium nanoparticles with tunable sizes using the inductive heater

Abstract

Colloidal semiconductor nanoparticles (NPs) or quantum dots (QDs) have the potential to replace their bulk counterparts by eliminating high-temperature, high-energy processes to produce large-area, flexible, and solution-processed thin-film arrays. The narrow and desirable bandgap (0.67 eV at 300 K) makes germanium (Ge) nanomaterials a candidate for IR detectors and as a tandem material for photovoltaics. Ge NPs offer a low-toxicity alternative to semiconductors containing heavy metals, and the large Bohr excitation radius of ∼24 nm results in a wide range of bandgap tunability. However, colloidal synthetic routes to Ge NPs with uniform sizes and shapes are much less mature. Inductive heating synthesis is an emerging technique that has the potential to displace the HI synthesis method to prepare colloidal nanoparticles very rapidly with a narrow size distribution, controlled size, and high crystallinity. Within this work, facile size-controlled synthesis of Ge NPs *via* inductive heating is discussed. Oleylamine acts as a solvent, a binding ligand, and a reducing agent in the synthesis. Germanium iodides (GeI_4, GeI_2) are used as the Ge precursor, and size control will be achieved by controlling the ratio of Ge^{4+}/Ge^{2+} in the precursor mix. It is expected that longer reaction times will influence the nanoparticle size distribution. The second part of the project discusses the spectroscopic characterizations of as-synthesized particles. It is found that the exciton lifetime of these particles increases with an increase in size.

5.1 Introduction

Nanomaterials of the group IV semiconductors have emerged as the very promising nontoxic class of photoluminescent nanomaterials with their applications in solar photoconversion and various optoelectronic devices.[139–141]Although silicon (Si) and germanium (Ge) are both interesting for optoelectronic application, Ge, in particular, is more fascinating because of its unique characteristics such as narrow bulk bandgap (0.67 eV at 300K), high exciton Bohr's radius (~24 nm) as compared to Si (bandgap = 1.12 eV and exciton Bohr's radius = 5 nm).[142–145] The small bandgap of Ge when combined with large exciton Bohr's radius gives rise to quantum confinement effect even for larger nanoparticles (NPs). The large exciton Bohr's radius) along with a high absorption coefficient of $\sim 2 \times 10^5$ cm^{-1} provides a strong motivation for research toward its application of solar cells, field-effect transistors, flash memory devices, photodetectors.[33,145–147] Furthermore, the low cost and relative ease of solution-based processing techniques colloidally stable solutions of Ge NPs can potentially be useful materials for the cost-effective fabrication of optoelectronic devices.[139,140] Additionally, the low toxicity of Ge combined with its ability to be dispersed in solution offers plenty of biological applications like cell imaging and labelling.[139,147] Recently, a diverse range of strategies has been developed for the colloidal synthesis of Ge NPs. Some of the common predominant methods are metathesis reactions using Zintl salts, hydride reduction of Ge halides, thermal decomposition of organogermane precursors.[139,141,142,147] Though, these methods are successful to some extent but there are considerable aspects that need to be improved.[145,147–150] The strong covalent nature of Ge demands a very high crystallization temperature i.e., usually higher than the boiling point of commonly used solvents. Therefore, most of the reported synthetic routes yield amorphous products and are prone to oxidize. To address this, strong reducing agents such as Na, $LiAlH_4$, n-BuLi are required to prepare crystalline Ge NPs which in turn may form toxic byproducts.[33,151,152]

The optical properties of Ge NPs are importantly defined by their size. Therefore, the discovery of a correct approach for synthesizing crystalline, air-stable colloidal Ge NPs with good control over size and shape is essential to advance the applicability of these NPs. Some attempts have been made in the past to control the size by varying the precursor concentration but only limited control oversize has been evidenced and scalability is also an issue with this method.[142,143,153] For example, Prabakar et al. have tuned the size of Ge NPs from 4 to 5.5 nm by varying the hydride reducing agents in their synthesis.[154] Ruddy et al. were able to prepare Ge NPs in the size range of 3-11nm by varying the reduction potential of two different precursors (Ge^{4+} and Ge^{2+}).[143]

Recently, the size-tunable synthesis of Ge NPs by microwave (MW) heating was reported by Kauzlarich and co-workers.[70] They have demonstrated fine control over the size of Ge NPs (3-11nm) by varying the concentration of the precursor mixture. They concluded that MW heating produced Ge NPs with better crystallinity in shorter heating time as compared to the conventional heating methodology.[70] Similarly, Xue et al. established that oleylamine can be used for the successful reduction of Ge^{2+} to Ge^{0}.[155]

In this work, we have adopted a similar idea from the works of Kauzlarich and co-workers and Xue et al. and demonstrated the simple and milder approach for the size-controlled synthesis of Ge NPs by inductive heating (IH) methodology. Here, oleylamine is a triple function of solvent, binding ligand, and reducing agent for both of the Ge^{4+} and Ge^{2+} precursors.[70,156] In the IH method, the reaction mixture is observed to increase the temperature at a rate of 200-300 °C/second, whereas in conventional heating, the reaction mixture is observed to increase in temperature at a rate of 10-20 °C/minute.[157] There are two primary reasons for applying the induction heating method specifically to Ge NPs synthesis is an insightful research endeavor: (i) To our knowledge, the induction heating method has not yet been introduced to the preparation of Ge NPs by Ge halide reduction; (ii) Kauzlarich et al. have shown oleylamine as a favorable reducing agent in the preparation of Ge NPs, but oleylamine is not a good microwave absorber, therefore heating via microwave irradiation is inefficient for rapid production of NPs.[70]

Our research group has successfully developed the IH method for the synthesis of monodisperse, air-stable iron, iron oxide NPs, and CdSe quantum dots in past years.[18,158,159] Recently we reported the use of IH synthesis of phase pure γ-Fe_2O_3 NPs from a solid precursor avoiding the use of toxic and expensive organometallic compounds like iron pentacarbonyl precursor.[158] There has not been any report of nanoscale Ge prepared by IH previously. Herein, for the first time to the best of our knowledge, we have explored it for the preparation of colloidal Ge nanocrystals. The reactor setup is similar to the setup discussed in **Chapter 3** and **Chapter 4**. The size and crystallinity of the synthesized Ge NPs using GeI_2/GeI_4 and solvent oleylamine at different reaction times, and concentration is studied. The resulting NPs Ge NPs confirmed by high-resolution transmission electron microscopy (HRTEM). In addition to this, these particles were subjected to spectroscopic study *via* UV- NIR spectroscopy and transient absorption spectroscopy (TAS) studies.

5.2 Materials and methods

5.2.1 Chemicals

Oleylamine was purchased from Sigma–Aldrich (70%) and was used after degassing under vacuum. Germanium (II) iodide was purchased from Gelest, and germanium (IV) iodide (99.999% Ge) was purchased from STREM Chemicals. Common solvents (i.e., toluene, methanol, hexane) used in the NPs purifications were used as received (Fisher, ACS grade) under ambient conditions.

5.2.2 Inductive heating synthesis

Ge NPs synthesis was carried out in a standard 7KW inductive heater. The reactor setup was based on our recent work for air-stable Fe NPs, IONPs, and CdSe QDs.[37,52,65] In an N_2- filled glovebox, a stock solution was prepared by mixing GeI_2 (0.2 mmol- 0.8 mmol) with 8 mL of degassed oleylamine. The solution was sonicated to completely dissolve the GeI_2 (the sonication time was typically about 20 minutes). The dissolution resulted in a colorless to pale yellowish solution depending upon the concentration of precursor. Then, the solution was transferred back to the glovebox and the reactor was filled with steel balls (25.92 g, Bearing-Quality E52100 Alloy Steel, Hardened Ball, 1/8″ diameter) and 4mL of the stock solution. Following this, the reactor was transported to the inductive heater and connected to tubing to maintain an argon atmosphere throughout the reaction. And the reaction mixture was heated inductive heater at minimum power for 5 s to 15 s to monitor the effect in size, crystallinity with the change in different parameters such as heating time, the concentration of precursor, and the ratio of GeI_2 and GeI_4. The color of the resulting product was observed to vary from orange to brown to black, depending on the NPs size. The schematic of the experimental procedure is shown in Supporting information **Figure 5.S1**

The contents of the IH reactor were transferred into a centrifuge tube and then washed with 2–3 mL of toluene for transferring NPs, and excess methanol (20-25 mL) was added to precipitate the NPs. Centrifugation (8000 rpm) for about 10–15 min for the complete precipitation of the NPs. The colorless supernatant was discarded, and the oleylamine-terminated Ge NPs were dispersed in about 4-5 mL of toluene or hexane and stored in a vial under N_2 atmosphere for future use.

5.2.3 Characterization

The instrumental details for TEM, HRTEM, EDS, and EDX are the same as we discussed in **Chapter 3** and **Chapter 4**. UV-Vis-NIR spectra of diluted Ge nanoparticle dispersions were recorded at room temperature, using a Perkin–Elmer Model Lambda 750 spectrophotometer in the range of 500–1500 nm.

5.3 Result and discussion

5.3.1 Effect of GeI_2 concentration on size of NPs

In a typical synthesis, 4 mL of 0.025 M to 0.1 M precursor mixture (prepared by mixing 0.2-0.8mmol of GeI_2 with 8 mL of oleylamine) was placed into an inductive heating reactor with steel balls in it. The reduction was carried out after heating for 5 s in an IH at minimum power. The final temperature of the reaction is the same as the boiling point of oleylamine (T_{bp}= 367 °C). The reaction typically results in a dark brownish solution, which is indicative of the formation of nanoscale germanium. The literature suggests that the product formation is due to the presence of an amine.[80] Additionally, there are some reports in the literature in which amine is oxidized to imine or nitrile species during the reduction reaction.[160,161]

For 0.025 M GeI_2 quantity, only a few Ge NPs of size are formed (**Figure 5.1A**) it could be due to the insufficient collision between reactant molecules due to the small concentration of reactant. Further increases in precursor quantity (GeI_2) up to 0.8 M formed larger numbers of NPs. (**Figure 5.1D**). It could be attributed to the fact that a higher concentration of monomers provides higher numbers of collisions thereby yielding larger numbers of nanomaterials. The TEM images (**Figures 5.1B** and **Figure 5.1C**) revealed an increase in average NPs size when the precursor quantity was tripled from 0.025 M to 0.075 M, further increases in precursor quantity had a

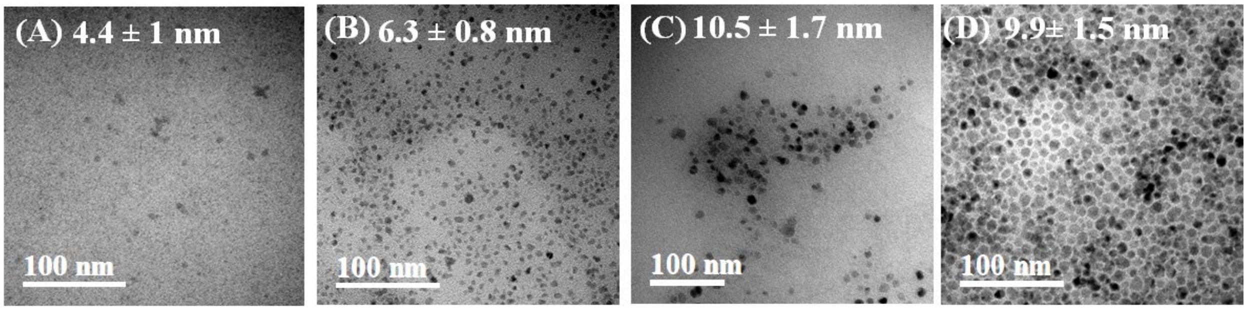

Figure 5.1 TEM images of Ge NPs produced using **(A)** 0.025M GeI_2, **(B)** 0.05M GeI_2, **(C)** 0.075M GeI_2, and **(D)** 0.1M GeI_2 at 5 s heating time. The size distribution plots are presented in supporting information **Figure 5.S2**

minimal effect on the average nanocrystal size, which is consistent with previous reports on Ge NPs wherein variation in precursor quantity resulted in large size differences, this reaction system was observed to respond favorably to changes in precursor quantities in the tested range.[162]

5.3.2 Effect of GeI_2/ GeI_4 concentration on size of NPs

In an effort to apply the multivalent reduction first reported by Neale and co-workers, and utilized by Kauzlarich and co-workers in microwave heating, the possible reduction of the Ge^{4+} precursor (GeI_4) by oleylamine at different ratio of GeI_2/GeI_4 (0 to 1) at fixed heating time of 5 s is investigated.[69,70]

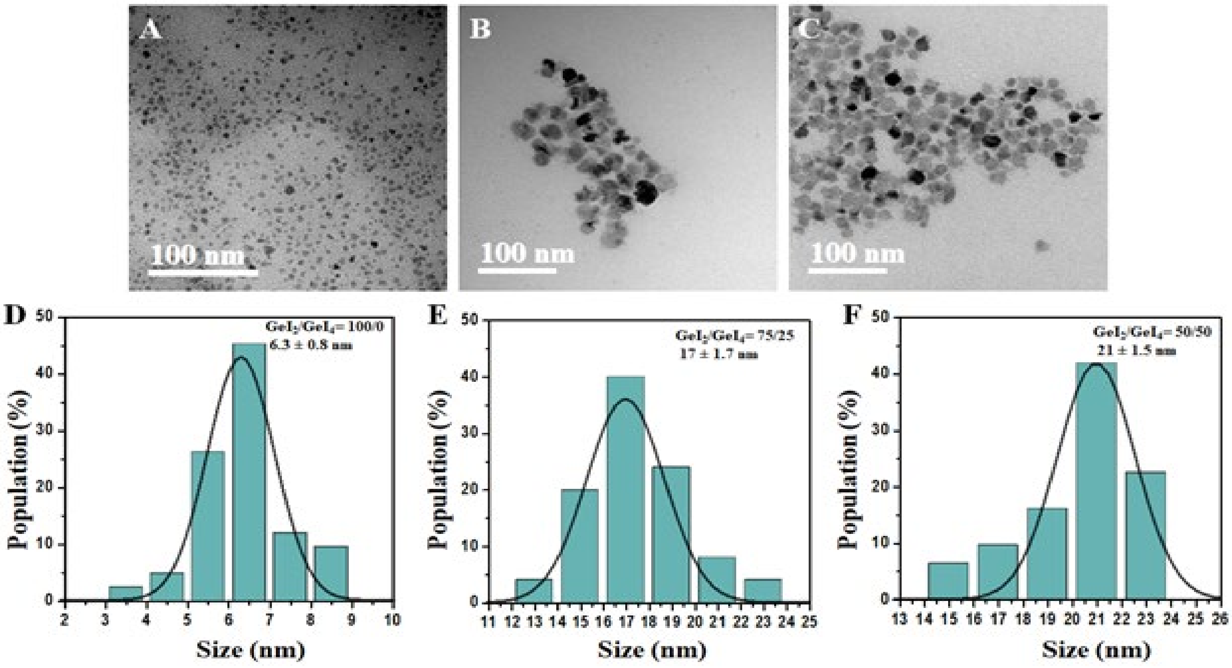

Figure 5.2 Effect of precursor ratio on the size of NPs. (A) GeI_2/GeI_4=100/0, (B) GeI_2/GeI_4=75/25, (C) GeI_2/GeI_4= 50/50. (D-F) are corresponding size distribution plots.

A series of reactions were carried out with precursors composed of GeI_4/GeI_2 in different ratios (ranging from 0.0 to 1.0) for 5 s. When the total Ge concentration in the precursor mix was kept at a constant at 0.4 mmol, the isolated final products indicated a gradual change from amorphous to crystalline with the inclusion of GeI_4 in the precursor mix (Supporting Information, **Figure 5.S3**). TEM analyses again indicated a significant increase (about three times) in average size, corresponding to the gradual addition of GeI_4 to the precursor mix (**Figure 5.2B**). The gradual increase in size clearly indicates that the multivalent reduction approach previously shown for n-BuLi works with oleylamine also.[69] These nanoparticles were not a stable dispersion in toluene (even after sonication), because of their large size and the lack of organic ligands on the surface. However, it is very exciting to know the Ge^{4+} can be reduced by oleylamine. The steel balls used in the reactor setup. It also signified that the controlled addition of GeI_4 would provide fine control over particle size in our reactions. Further experiments made it clear that the Ge^{4+} precursor can indeed be reduced to Ge when taken along with Ge^{2+}, with the Ge^{4+}/Ge^{2+} ratios not exceeding a value of 1. This finding is consistent with the previously reported work by Muthuswamy *et al.*[70]

5.3.3 Effect of reaction time on the size of NPs

The effect of reaction time was also probed for any particle size changes by keeping constant precursor concentration (0.05 M GeI_2) and changing the heating time from 5 s to 3*5 s taking 2 minutes of break time between the cycle. The results indicated an overall increase in the average size of the nanoparticles for each heating time. It is anticipated that the increase in heating time provides an additional time for nucleation and growth of the nanoparticles thereby yielding larger-sized NPs. Furthermore, the increase in the size with the increase in heating time is consistent with Fe and IONPs discussed in **Chapter 3** and **Chapter 4**.

5.3.4 Spectroscopic characterization of NPs

In order to study the spectroscopic properties of NPs, three different sizes i.e. 6.3 nm, 10.5 nm, and 21 nm NPs were taken into considerations. The absorption measurements (**Figure 5.4 A**) were carried out on dilute dispersions of Ge nanoparticles in hexane in the range of 500–1500 nm. The

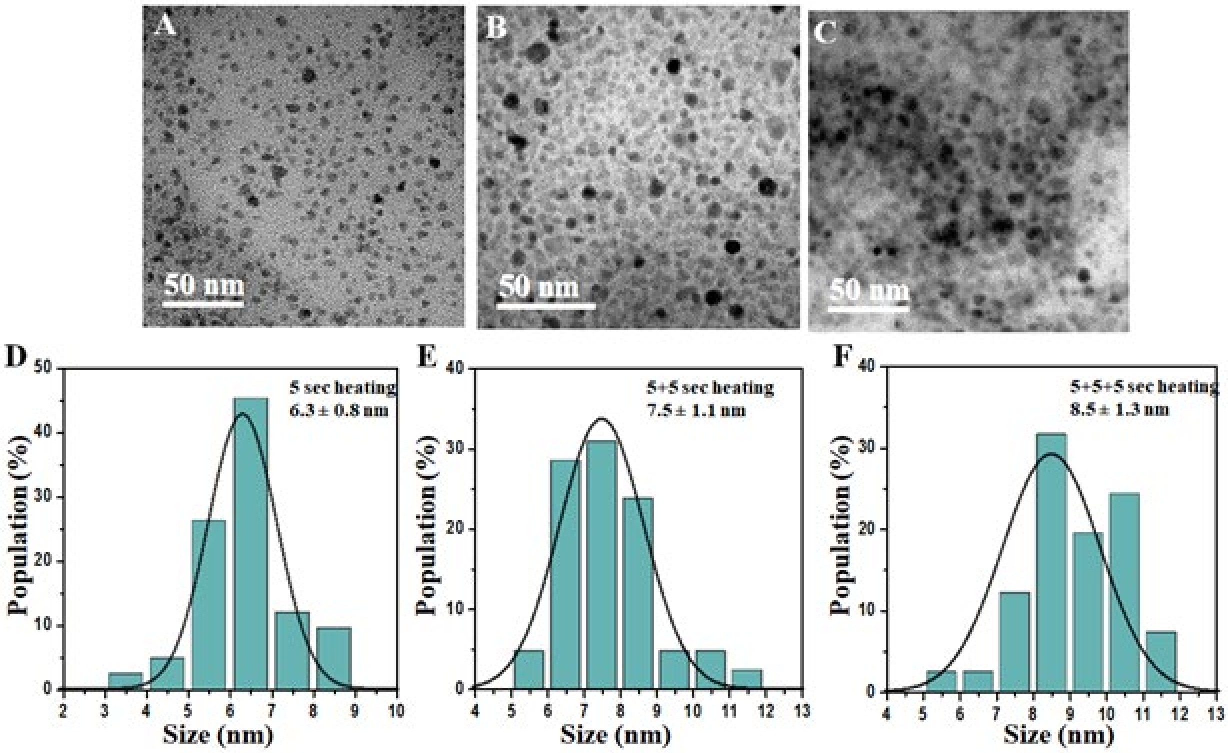

Figure 5.3 Effect of reaction time on the size of NPs. (A) 5 s, (B) 5*2 s, (C) 5*3 s, and (D-F) are corresponding size distribution plots.

dilution was carried out in a glovebox, and the sample was exposed to ambient conditions during the time frame of the measurement for a few minutes. The collected spectra are featureless and are comparable to previously reported measurements on Ge nanoparticles in a similar size range.[70] Emission was not observed in the visible range, or the 800–1600 nm range, and we hypothesize that this may be due to the presence of defects on the surface. Furthermore, the transient absorption spectra (**Figure 5.3 B-D**) of corresponding NPs indicated a very short lifetime of the exciton.[70,141,163,164] This could be attributed to the presence of surface defects. In addition to this, the lifetime of exciton increases with the increase in size from 6.3 to 10.5 nm, however, it decreased when the size increased up to 21 nm. We speculate that the recombination of exciton takes place at a larger size thereby decreasing the lifetime.

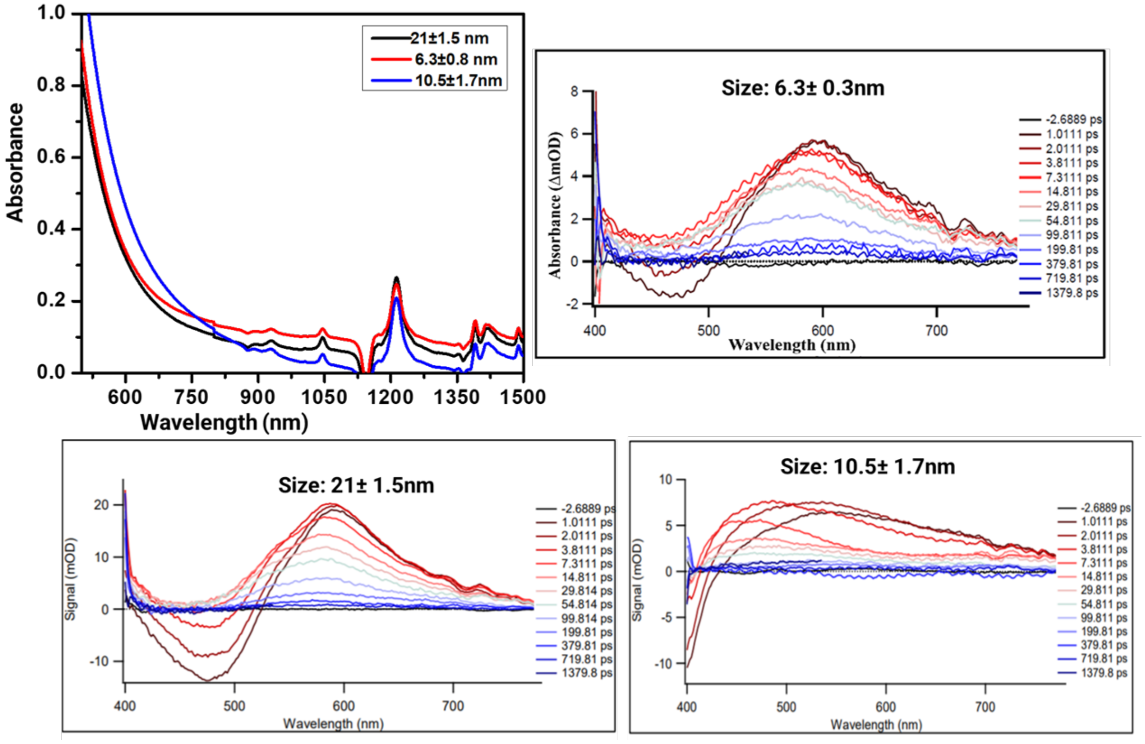

Figure 5.4 Spectroscopic characterization of Ge NPs. (A) UV-Vis-NIR absorption and (B-D) are transient absorption spectra of corresponding NPs

5.4 Conclusions

In summary, we have developed a simple approach for the preparation of crystalline germanium nanoparticles by induction heating. Nanoparticles in the range 5-21 nm have been prepared by varying Ge precursor ratios and time. The reduction of Ge precursors has been achieved under milder operating conditions and the method avoids the use of highly reactive reducing agents and etching agents. Compared to the conventional heating and microwave heating, induction heating was shown to result in crystalline nanoparticles at a shorter heating time. Literature indicates that Group IV nanoparticle synthesis has been a challenge and we expect that this new facile approach will result in further exploration of IH methods, resulting in easier preparation methods for Group IV semiconducting nanoparticles. The induction heating method leads to a more rapid synthesis of nanomaterials, which may result in industrial feasibility, and an establishment of efficient capitalization.

Chapter 6- Synthesis of manganese oxide and iron/manganese alloy nanoparticles by magnetic heating

Abstract

Herein, manganese oxide and iron/manganese alloy nanoparticles (~4 nm and~3 nm) were synthesized *via* easy, one-pot, non-sophisticated, and quicker magnetic induction heating technique for the first time. Two types i.e., manganese oxide and iron/manganese alloy nanoparticles were prepared by the decomposition of manganese carbonyl ($Mn_2(CO)_{10}$) in the reducing agent oleylamine in an induction heating reactor filled with the steel balls. As preliminary experiments, the structural and morphological properties of as-prepared NPs were investigated by energy-dispersive x-ray spectroscopy (EDX). It is hoped that upon successful optimization of the synthetic protocol, produced NPs could be used as a catalyst to produce ammonia by step catalysis which could open up a new opportunity for more economical and fossil-fuel-free conditions.

6.1 Introduction

It is well known that the nanomaterials having the same composition as known materials in bulk form possesses significantly different physicochemical properties.[165,166] This unique feature of nanoparticles and their large surface-area-to-volume ratio has been extensively exploited for their potential applications in electrical, magnetic, and catalytic properties.[10] Among various nanoparticles, manganese (Mn) based nanoparticles, including MnO, MnO_2, and Mn_3O_4, are fascinating compounds and have been used in catalysis, supercapacitors, alkaline and rechargeable batteries, adsorbent, sensors, and imaging.[8,167–170] Of particular interest to catalysis, MnO and MnO_2 nanoparticles such as MnO_2/NaY, MnO_x/TiO_2, have attracted great interest as a catalyst due to their high catalytic activity for NH_3-selective catalytic reduction, theoretical capacity, low cost, and environmental benignity.[171–173] Also, it has been reported that the amalgamation of transition metals can increase the catalytic activities of the Mn-based catalysts.[157] Aligned to this direction, various Mn-based nanoparticles catalysts including Ce–Mn, Cu–Mn, Fe–Mn, Cr–Mn, and Nb–Mn mixed oxide catalysts for NH_3-selective catalytic reduction were synthesized using conventional methods such as hydrothermal, sol-gel, oxidation-reduction, wet chemical reaction, and pulsed laser deposition techniques.[174–177] However, less attention has been given to their potential application in the activation of dinitrogen (N_2), which is the prerequisite, in ammonia synthesis. Transition metals play a very important role in heterogeneous catalysis including ammonia synthesis.[178] For example, Fe, Mn, and Rh have moderate nitrogen adsorption energies, and therefore exhibit excellent NH_3 synthesis performances and have been explored.[179,180] Similarly, nitride-enabled step catalysis for NH_3 synthesis has been reported by Pfromm and co-workers.[179–183] These works appeared to be very promising. After successful study of these materials and their behaviors for the overall process, a trade-off of N_2 vs NH_3 synthesis for pure nitride materials can be considered as a fascinating solution to overcome the limitation experienced for pure materials.[179,181]

For the successful execution of the above-discussed applications, we need to be able to synthesize air-stable Mn and Mn-based alloy NPs. But studies of Mn NPs have been limited because of difficulties involving synthesis and stability.[184] Most of the manganese salts used in the synthesis possess large negative reduction potentials (e.g., $E°Mn_2+/Mn = -1.185$ eV vs SHE) thereby making it difficult to generate zerovalent Mn in solution using standard reducing agents which are frequently used in colloidal syntheses.[14] Furthermore, the oxyphilic nature of Mn also renders Mn NPs highly reactive in air.[184] Only a few examples of Mn NPs are known such as ball milling, inert gas condensation, and arc discharge.[185–187] Most of these methods resulted in the formation of significant crystalline oxide impurities resulting in the complexities in magnetic measurements.[184] Chemical routes to Mn-containing NPs, such as MnP, MnPt, and $MnPt_3$ have incorporated Mn using thermal decomposition of $Mn_2(CO)_{10}$.[188–190] Attempts to prepare elemental Mn NPs using similar methods have yielded oxides as other chemical routes to early transition metal systems.[184]

Herein, we have utilized the colloidal synthesis of Mn and Fe-Mn alloy NPs using the improved IH method by using the decomposition of manganese carbonyl ($Mn_2(CO)_{10}$) in the reducing agent OA in an IH reactor filled with the steel balls. We hypothesize that the ferromagnetic steel ball used in the reaction provides the reductive atmosphere to produce zerovalent Mn NPs as demonstrated for Fe NPs in **Chapter 3**. But the resulting NPs were found to be MnO instead of Mn, however, the optimization of the synthetic condition is still in progress. It is hoped that upon successful optimization of the synthetic protocol, produced NPs could be used to produce ammonia by step catalysis which could open alternative routes with much more economical and fossil-fuel-free conditions.

6.2 Materials and methods

Method of synthesis

Manganese nanoparticles were synthesized using the bottom-up method following our previously reported inductive heating protocol with some modifications.[37,38,52,65] The setup for the inductive heater and reactor with precursor mixture is similar to work previously reported for the synthesis of Fe, IONPs, and QDs by our group. Briefly, $Mn_2(CO)_{10}$ powder was used as a precursor while OA was used as the solvent. The precursor and solvent were mixed inside the N2- filled glovebox and the stock solution was prepared (0.3M) by stirring the mixture until the precursor was completely dissolved resulting in a yellowish color solution (the mixing time is approximately 24 hr). The reactor system (**Figure 2.5, Chapter 2**) filled with steel balls was placed into the nitrogen-filled glovebox. Then, about 4 mL precursor solution was transferred from the stock solution to the reactor which is followed by the insertion of reactor vessel into the coil of the inductive heater (standard 7 kW inductive heater) fitted with tubes to maintain an argon atmosphere during the reaction. The yellowish color solution turned darker black with increasing reaction time indicating the formation of NPs. The synthesized NP solution was cooled to room temperature, then isolated by centrifuging using methanol (~20–25 mL) at 8000 rpm for 10 minutes followed by three-times sonication for 5 minutes per solvent system used. The colorless supernatant was discarded, and the precipitated NPs were then dispersed in small quantities of hexanes (3–4 mL), sealed, and stored in a glovebox maintained inert atmosphere until further use.

6.3 Result and discussion

The size and morphology of as-synthesized particles were studied by the TEM and the elemental composition of these particles was examined by EDX. The TEM images of as-synthesized particles are shown in **Figure 6.1.** These particles are of average size 6.5 ± 1.4 nm (**Figure 6.S1**, supporting information), and the elemental study by EDX (**Figure 6.2**) indicated the formation of MnO.

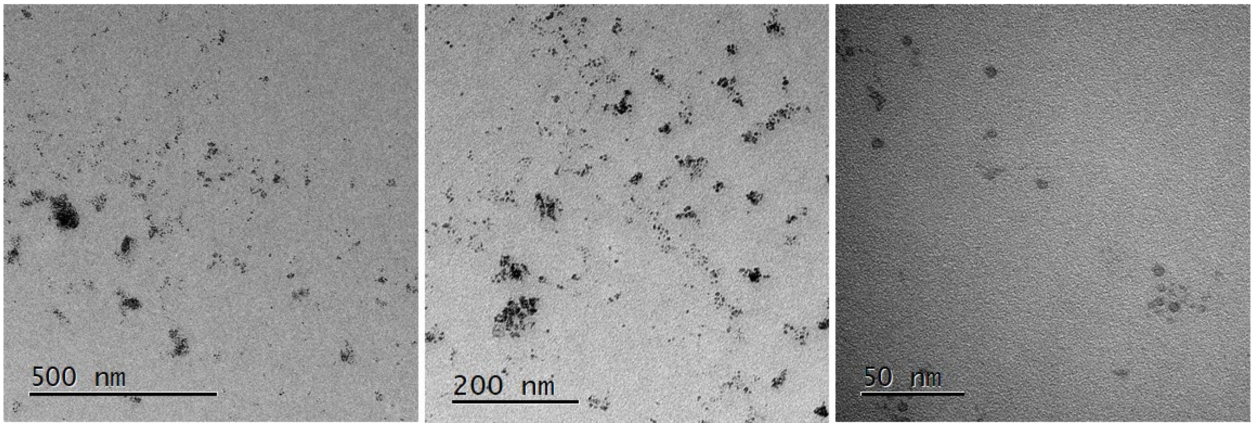

Figure 6.1 TEM images of MnO produced using 0.3M $Mn_2(CO)_{10}$ and oleylamine at 5 s heating time at different scale bars.

The EDX spectra also showed the presence of Cu which is expected from Cu- coated TEM grid.

As we could not reach our goal of preparing zerovalent Mn NPs by heating $Mn_2(CO)_{10}$ and oleylamine, then, we tried to make Mn NPs by mixing 2/2 mL of OA and 1-ODE consequently this also yielded the formation of MnO NPs as revealed by elemental composition data and TEM as shown in **Figures 6.3** and **Figure 6.4.**

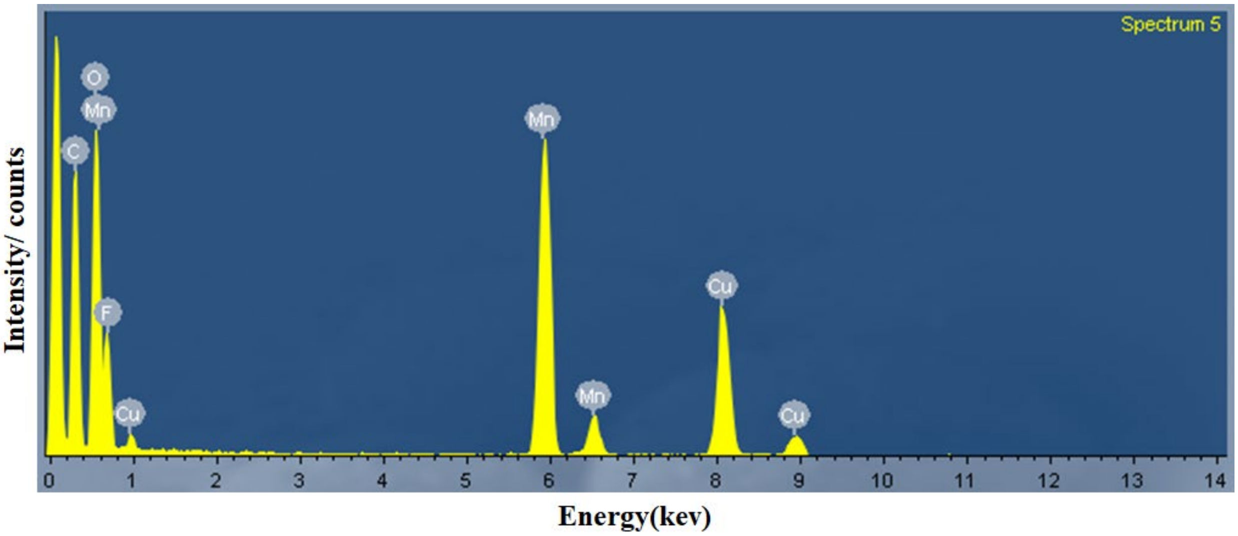

Figure 6.2 EDX spectra of MnO produced by 0.3M $Mn_2(CO)_{10}$ and oleylamine at 5 s heating.

Furthermore, aiming to achieve our goal, we used the same approach used by Bondi *et al.*to prepare air-stable Mn NPs now using the IH technique instead of their heat-up method .[184] Bondi et al. have used manganese (II) chloride powder as a precursor while diphenyl ether and oleic acid as solvents and n-BuLi as a reducing agent to prepare 13 nm-sized α-Mn nanoparticles. However, the result NPs were still showing MnO, indicating the maintenance of an oxygen-free environment is very challenging. The HRTEM images (**Figure 6.5**) of these particles suggested the presence of crystalline MnO at the center of the NPs with an amorphous MnO shell.

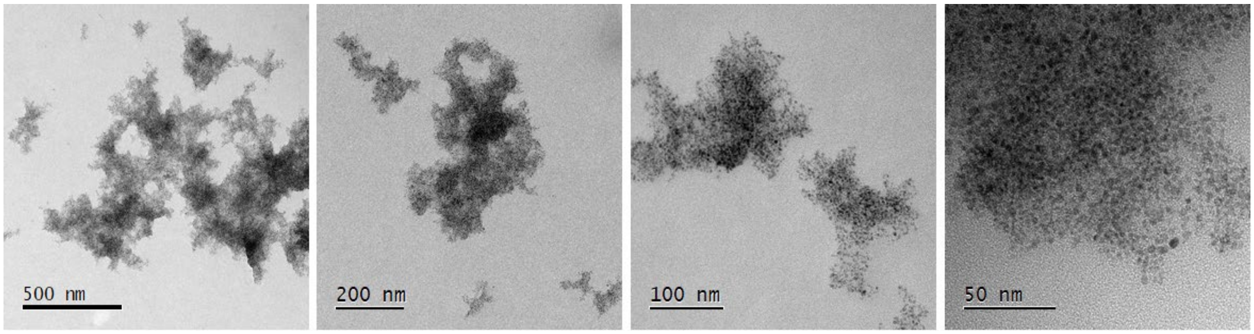

Figure 6.3 TEM images of MnO produced using 0.3M $Mn_2(CO)_{10}$, OA, and 1-ODE at 5 sec heating time at different scale bars.

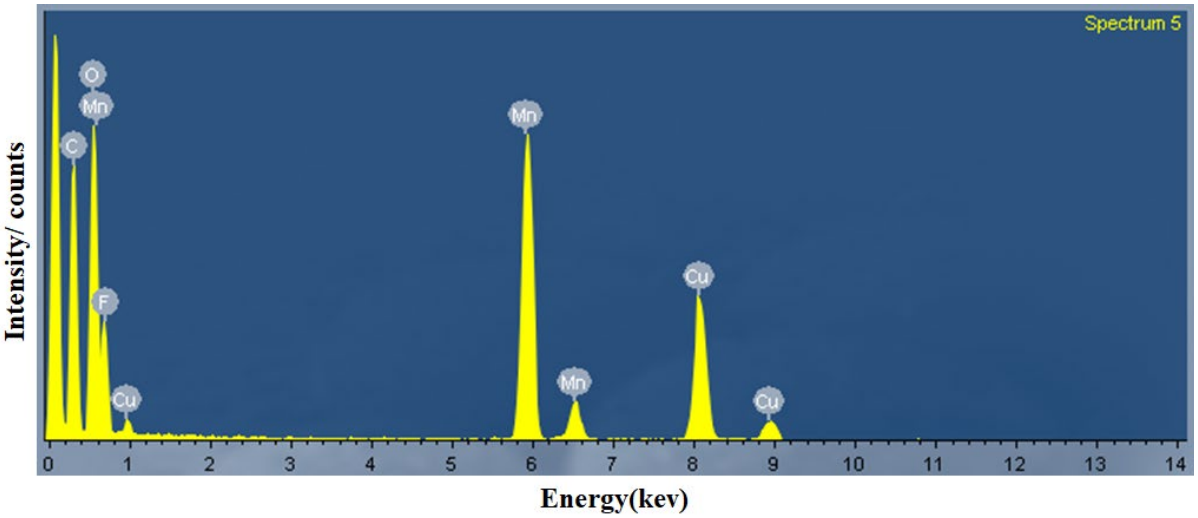

Figure 6.4 EDX spectra of MnO produced using 0.3M $Mn_2(CO)_{10}$, OA, and 1-ODE at 5 s heating time.

All the approaches discussed above did not yield air-stable Mn NPs. Now, we tried to coat Mn with a Fe shell to see if that could be a possible way to avoid oxygen. For this, we used the mixture of $Mn_2(CO)_{10}$ powder and $Fe(CO)_5$ as the precursor and 1-ODE as the solvent and heated in IH for 7 s. These particles were then subjected to TEM and EDX (**Figures 6.5** and **Figure 6.6**). The elemental composition analysis indicated the formation of iron-manganese oxide NPs.

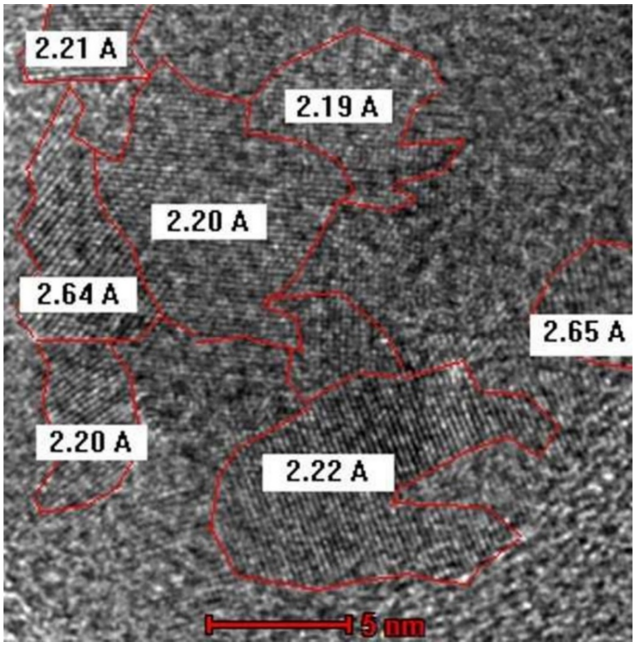

Figure 6.5 HRTEM images of single MnO NPs. Individual crystal domains are outlined in red along with their respective calculated d-spacings.

As these multiple approaches resulted from Mn oxide particles instead of air-stable Mn particles, we anticipate the purification ambient condition might have resulted in the formation of the oxide. However, further characterizations of as-synthesized NPs are required before making any discrete conclusion.

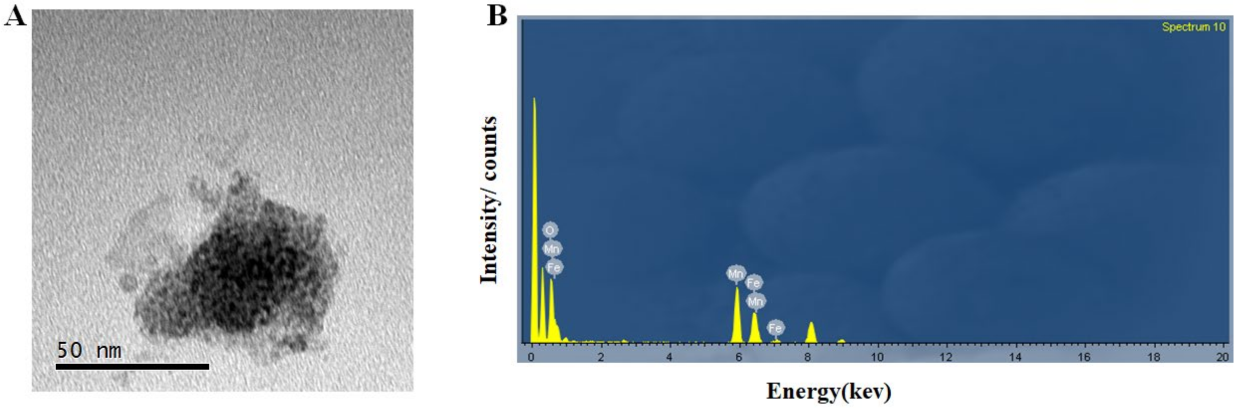

Figure 6.6 (A) TEM images of Fe/Mn Oxide NPs produced using $Mn_2(CO)_{10}$ powder and Fe (CO_5) and 1-ODE at 7 s heating time (B) Corresponding EDX spectra.

6.4 Conclusion and outlook

In summary, we showed a simple and versatile inductive heating technology for the synthesis of core-shell structured manganese oxide nanoparticles having a crystalline core with amorphous shells from the bottom-up technique. However, further investigation for optimizing the reaction condition to yield air-stable Mn and Fe-Mn NPs is required to achieve our goal. Upon successful synthesis of these particles, they will be further tested for ammonia production.

Chapter 7- Summary and outlook

This dissertation demonstrated a robust and rapid methodology for colloidal synthesis. Syntheses and characterization of air-stable metal nanoparticles, their oxides, and semiconductor nanoparticles are discussed, including their magnetic properties are studied. It was found that inductive heating methodology would be an efficient way to prepare colloidal NPs thereby giving a similar outcome as the traditional HI method. Additionally, the use of a high concentration of precursor than typically used in literature for conventional hot-injection methods was demonstrated to produce monodispersed NPs. This allows the exploration of new synthesis regimes not accessible by the hot-injection method. A facile method to prepare air-stable Fe NPs with size control is shown. Furthermore, the use of solid precursor which was limited by the traditional HI method is presented. Strong evidence of the formation of superparamagnetic IONPs with size control is described. The size dependence magnetic properties have been highlighted in different chapters of this dissertation. The increase in the saturation magnetization with the increase in the size of NPs and boiling point of solvent is well demonstrated in Chapter 3 and Chapter 4. Then, induction heating syntheses of colloidal Ge NPs are reported which focused on the effects of heating time and concentration on the size control are discussed. Also, facile one-pot synthesis of MnO and Mn@Fe oxide NPs is described. Experimental results and analyses show that IH not only has proven to be an effective way of achieving the preparation of nanoparticles but could also provide a way of separating the nucleation and growth process, which could facilitate the development of a more accurate theory describing such processes. The improved one-pot IH method will open a new pathway for rapid and scalable synthesis of colloidal NPs with size control which is difficult to achieve by conventional heating methods. Additionally, it demonstrates the possibility of new compositions of NPs from colloidal routes.

As we continue to learn more about the synthesis of colloidal NPs with IH methodology, new opportunities in IH-assisted routes emerge. This method offers more scalability than HI and other methods thereby resulting in more industrial feasibility and an establishment of efficient capitalization. One-pot IH-assisted method promises a scalable and low-cost production of highly crystalline NPs by overcoming the traditional disadvantages of long reaction times, high temperature and pressure, complicated precursor preparation, and exhaustive post-synthetic purification steps. With these exciting developments as well as the rich advantages exhibited by IH methodology, it is hoped that this methodology will be used in the n-type doping of Ge NPs in future as demonstrated in **Figure 7.1** and **Figure 7.2**. Not limited to this, IH methodology could be extended by using ferrofluid in colloidal synthesis by replacing the use of steel balls in the specialized reactor.

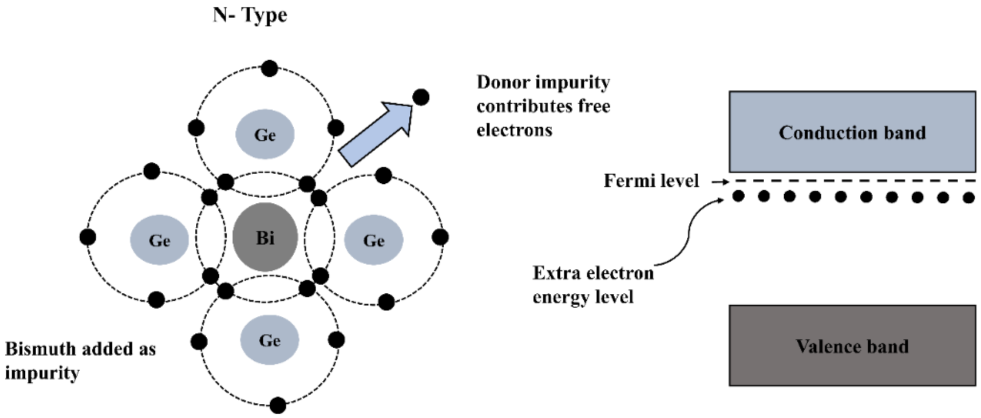

Figure 7.1 Illustration of n-type Bi doping in Ge NPs

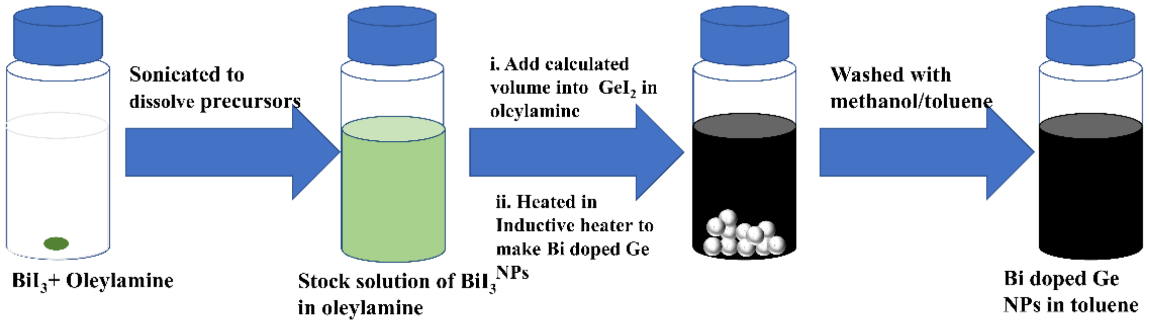

Figure 7.2 Schematic illustration of the inductive heating assisted Bi doping of Ge NPs**.**

References

(1) Xu, X.; Friedman, G.; Humfeld, K. D.; Majetich, S. A.; Asher, S. A. Synthesis and Utilization of Monodisperse Superparamagnetic Colloidal Particles for Magnetically Controllable Photonic Crystals. *Chem. Mater.* **2002**, *14* (3), 1249–1256. https://doi.org/10.1021/cm010811h.

(2) Yu, H.-D.; Regulacio, M. D.; Ye, E.; Han, M.-Y. Chemical Routes to Top-down Nanofabrication. *Chem. Soc. Rev.* **2013**, *42* (14), 6006–6018. https://doi.org/10.1039/C3CS60113G.

(3) Biswas, A.; Bayer, I. S.; Biris, A. S.; Wang, T.; Dervishi, E.; Faupel, F. Advances in Top–down and Bottom–up Surface Nanofabrication: Techniques, Applications & Future Prospects. *Adv. Colloid Interface Sci.* **2012**, *170* (1), 2–27. https://doi.org/10.1016/j.cis.2011.11.001.

(4) Marasini, R. Design Strategies and Application of Stimuli-Responsive Nanoparticles for Cancer Diagnosis and Therapy, Kansas State University, Manhattan, KS, USA, 2020.

(5) Marasini, R.; Pitchaimani, A.; Thanh Nguyen, T. D.; Comer, J.; Aryal, S. The Influence of Polyethylene Glycol Passivation on the Surface Plasmon Resonance Induced Photothermal Properties of Gold Nanorods. *Nanoscale* **2018**, *10* (28), 13684–13693. https://doi.org/10.1039/C8NR03026J.

(6) Huo, D.; Kim, M. J.; Lyu, Z.; Shi, Y.; Wiley, B. J.; Xia, Y. One-Dimensional Metal Nanostructures: From Colloidal Syntheses to Applications. *Chem. Rev.* **2019**, *119* (15), 8972–9073. https://doi.org/10.1021/acs.chemrev.8b00745.

(7) Cai, S.; Fu, Z.; Xiao, W.; Xiong, Y.; Wang, C.; Yang, R. Zero-Dimensional/Two-Dimensional AuxPd100–x Nanocomposites with Enhanced Nanozyme Catalysis for Sensitive Glucose Detection. *ACS Appl. Mater. Interfaces* **2020**, *12* (10), 11616–11624. https://doi.org/10.1021/acsami.9b21621.

(8) Tan, Y.; Meng, L.; Peng, Q.; Li, Y. One-Dimensional Single-Crystalline Mn3O4 Nanostructures with Tunable Length and Magnetic Properties of Mn3O4 Nanowires. *Chem. Commun.* **2011**, *47* (4), 1172–1174. https://doi.org/10.1039/C0CC00978D.

(9) NACK_U3_Maeder_Nanoparticle_Synthesis.Pdf.

(10) Burda, C.; Chen, X.; Narayanan, R.; El-Sayed, M. A. Chemistry and Properties of Nanocrystals of Different Shapes. *Chem. Rev.* **2005**, *105* (4), 1025–1102. https://doi.org/10.1021/cr030063a.

(11) Baig, N.; Kammakakam, I.; Falath, W. Nanomaterials: A Review of Synthesis Methods, Properties, Recent Progress, and Challenges. *Mater. Adv.* **2021**, *2* (6), 1821–1871. https://doi.org/10.1039/D0MA00807A.

(12) Khan, I.; Saeed, K.; Khan, I. Nanoparticles: Properties, Applications and Toxicities. *Arab. J. Chem.* **2019**, *12* (7), 908–931. https://doi.org/10.1016/j.arabjc.2017.05.011.

(13) Ealia, A. M. A Review on the Classification, Characterisation, Synthesis of Nanoparticles and Their Application. 16.

(14) Cushing, B. L.; Kolesnichenko, V. L.; O'Connor, C. J. Recent Advances in the Liquid-Phase Syntheses of Inorganic Nanoparticles. *Chem. Rev.* **2004**, *104* (9), 3893–3946. https://doi.org/10.1021/cr030027b.

(15) Synthesis and characterization of a tumor-seeking LyP-1 peptide integrated lipid–polymer composite nanoparticle - Materials Advances (RSC Publishing) DOI:10.1039/D0MA00203H

https://pubs.rsc.org/en/content/articlehtml/2020/ma/d0ma00203h (accessed 2021 -11 -09).
(16) Polte, J. Fundamental Growth Principles of Colloidal Metal Nanoparticles – a New Perspective. *CrystEngComm* **2015**, *17* (36), 6809–6830. https://doi.org/10.1039/C5CE01014D.
(17) Dahal, N. SYNTHESIS AND CHARACTERIZATIONS OF NOVEL MAGNETIC AND PLASMONIC NANOPARTICLES. **2010**, 175.
(18) Ma, X.; Wu, F.; Kauzlarich, S. M. Alkyl-Terminated Crystalline Ge Nanoparticles Prepared from NaGe: Synthesis, Functionalization and Optical Properties. *J. Solid State Chem.* **2008**, *181* (7), 1628–1633. https://doi.org/10.1016/j.jssc.2008.06.018.
(19) Dhand, C.; Dwivedi, N.; Loh, X. J.; Ying, A. N. J.; Verma, N. K.; Beuerman, R. W.; Lakshminarayanan, R.; Ramakrishna, S. Methods and Strategies for the Synthesis of Diverse Nanoparticles and Their Applications: A Comprehensive Overview. *RSC Adv.* **2015**, *5* (127), 105003–105037. https://doi.org/10.1039/C5RA19388E.
(20) Nanofabrication: Conventional and Nonconventional Methods. **2001**, 21.
(21) Bellah, M. M.; Christensen, S. M.; Iqbal, S. M. Nanostructures for Medical Diagnostics. *J. Nanomater.* **2012**, *2012*, e486301. https://doi.org/10.1155/2012/486301.
(22) Xia, D.; Li, D.; Ku, Z.; Luo, Y.; Brueck, S. R. J. Top-Down Approaches to the Formation of Silica Nanoparticle Patterns. *Langmuir* **2007**, *23* (10), 5377–5385. https://doi.org/10.1021/la7005666.
(23) Stern, E.; Klemic, J. F.; Routenberg, D. A.; Wyrembak, P. N.; Turner-Evans, D. B.; Hamilton, A. D.; LaVan, D. A.; Fahmy, T. M.; Reed, M. A. Label-Free Immunodetection with CMOS-Compatible Semiconducting Nanowires. *Nature* **2007**, *445* (7127), 519–522. https://doi.org/10.1038/nature05498.
(24) Murray, C. B.; Kagan, C. R.; Bawendi, M. G. Synthesis and Characterization of Monodisperse Nanocrystals and Close-Packed Nanocrystal Assemblies. *Annu. Rev. Mater. Sci.* **2000**, *30* (1), 545–610. https://doi.org/10.1146/annurev.matsci.30.1.545.
(25) Jeevanandam, J.; Barhoum, A.; Chan, Y. S.; Dufresne, A.; Danquah, M. K. Review on Nanoparticles and Nanostructured Materials: History, Sources, Toxicity and Regulations. *Beilstein J. Nanotechnol.* **2018**, *9*, 1050–1074. https://doi.org/10.3762/bjnano.9.98.
(26) Chen, B.; Li, D.; Wang, F. InP Quantum Dots: Synthesis and Lighting Applications. *Small* **2020**, *16* (32), 2002454. https://doi.org/10.1002/smll.202002454.
(27) Zhang, L.; Niu, W.; Xu, G. Synthesis and Applications of Noble Metal Nanocrystals with High-Energy Facets. *Nano Today* **2012**, *7* (6), 586–605. https://doi.org/10.1016/j.nantod.2012.10.005.
(28) Roduner, E. Size Matters: Why Nanomaterials Are Different. *Chem. Soc. Rev.* **2006**, *35* (7), 583–592. https://doi.org/10.1039/B502142C.
(29) Alivisatos, A. P. Perspectives on the Physical Chemistry of Semiconductor Nanocrystals. *J. Phys. Chem.* **1996**, *100* (31), 13226–13239. https://doi.org/10.1021/jp9535506.
(30) Donegá, C. de M. Synthesis and Properties of Colloidal Heteronanocrystals. *Chem. Soc. Rev.* **2011**, *40* (3), 1512–1546. https://doi.org/10.1039/C0CS00055H.
(31) Carbone, L.; Cozzoli, P. D. Colloidal Heterostructured Nanocrystals: Synthesis and Growth Mechanisms. *Nano Today* **2010**, *5* (5), 449–493. https://doi.org/10.1016/j.nantod.2010.08.006.

(32) Lohse, S. E.; Murphy, C. J. Applications of Colloidal Inorganic Nanoparticles: From Medicine to Energy. *J. Am. Chem. Soc.* **2012**, *134* (38), 15607–15620. https://doi.org/10.1021/ja307589n.

(33) Talapin, D. V.; Lee, J.-S.; Kovalenko, M. V.; Shevchenko, E. V. Prospects of Colloidal Nanocrystals for Electronic and Optoelectronic Applications. *Chem. Rev.* **2010**, *110* (1), 389–458. https://doi.org/10.1021/cr900137k.

(34) Park, Y.-S.; Roh, J.; Diroll, B. T.; Schaller, R. D.; Klimov, V. I. Colloidal Quantum Dot Lasers. *Nat. Rev. Mater.* **2021**, *6* (5), 382–401. https://doi.org/10.1038/s41578-020-00274-9.

(35) Groeneveld, E.; de Mello Donegá, C. The Challenge of Colloidal Nanoparticle Synthesis. In *Nanoparticles: Workhorses of Nanoscience*; de Mello Donegá, C., Ed.; Springer: Berlin, Heidelberg, 2014; pp 145–189. https://doi.org/10.1007/978-3-662-44823-6_6.

(36) Nie, Z.; Petukhova, A.; Kumacheva, E. Properties and Emerging Applications of Self-Assembled Structures Made from Inorganic Nanoparticles. *Nat. Nanotechnol.* **2010**, *5* (1), 15–25. https://doi.org/10.1038/nnano.2009.453.

(37) Sharma, P.; Holliger, N.; Pfromm, P. H.; Liu, B.; Chikan, V. Size-Controlled Synthesis of Iron and Iron Oxide Nanoparticles by the Rapid Inductive Heating Method. *ACS Omega* **2020**, *5* (31), 19853–19860. https://doi.org/10.1021/acsomega.0c02793.

(38) Chikan, V.; McLaurin, E. J. Rapid Nanoparticle Synthesis by Magnetic and Microwave Heating. *Nanomaterials* **2016**, *6* (5). https://doi.org/10.3390/nano6050085.

(39) Shevchenko, E. V.; Talapin, D. V.; Schnablegger, H.; Kornowski, A.; Festin, Ö.; Svedlindh, P.; Haase, M.; Weller, H. Study of Nucleation and Growth in the Organometallic Synthesis of Magnetic Alloy Nanocrystals: The Role of Nucleation Rate in Size Control of CoPt3 Nanocrystals. *J. Am. Chem. Soc.* **2003**, *125* (30), 9090–9101. https://doi.org/10.1021/ja029937l.

(40) Gude, K. Synthesis Characterization and Applications of Colloidal Supported Metal Nanoparticles, University of Rhode Island, Kingston, RI, 2013. https://doi.org/10.23860/diss-gude-kalyani-2013.

(41) Peng, X.; Wickham, J.; Alivisatos, A. P. Kinetics of II-VI and III-V Colloidal Semiconductor Nanocrystal Growth: "Focusing" of Size Distributions. *J. Am. Chem. Soc.* **1998**, *120* (21), 5343–5344. https://doi.org/10.1021/ja9805425.

(42) Marqusee, J. A.; Ross, J. Kinetics of Phase Transitions: Theory of Ostwald Ripening. *J. Chem. Phys.* **1983**, *79* (1), 373–378. https://doi.org/10.1063/1.445532.

(43) Finney, E. E.; Finke, R. G. Nanocluster Nucleation and Growth Kinetic and Mechanistic Studies: A Review Emphasizing Transition-Metal Nanoclusters. *J. Colloid Interface Sci.* **2008**, *317* (2), 351–374. https://doi.org/10.1016/j.jcis.2007.05.092.

(44) Talapin, D. V.; Rogach, A. L.; Haase, M.; Weller, H. Evolution of an Ensemble of Nanoparticles in a Colloidal Solution: Theoretical Study. *J. Phys. Chem. B* **2001**, *105* (49), 12278–12285. https://doi.org/10.1021/jp012229m.

(45) Murray, C. B.; Norris, D. J.; Bawendi, M. G. Synthesis and Characterization of Nearly Monodisperse CdE (E = Sulfur, Selenium, Tellurium) Semiconductor Nanocrystallites. *J. Am. Chem. Soc.* **1993**, *115* (19), 8706–8715. https://doi.org/10.1021/ja00072a025.

(46) Prasad, B. L. V.; Stoeva, S. I.; Sorensen, C. M.; Klabunde, K. J. Digestive Ripening of Thiolated Gold Nanoparticles: The Effect of Alkyl Chain Length. *Langmuir* **2002**, *18* (20), 7515–7520. https://doi.org/10.1021/la020181d.

(47) Zhang, S.; Zhang, L.; Liu, K.; Liu, M.; Yin, Y.; Gao, C. Digestive Ripening in the Formation of Monodisperse Silver Nanospheres. *Mater. Chem. Front.* **2018**, *2* (7), 1328–1333. https://doi.org/10.1039/C8QM00077H.

(48) Leff, D. V.; Ohara, P. C.; Heath, J. R.; Gelbart, W. M. Thermodynamic Control of Gold Nanocrystal Size: Experiment and Theory. *J. Phys. Chem.* **1995**, *99* (18), 7036–7041. https://doi.org/10.1021/j100018a041.

(49) Herron, N.; Calabrese, J. C.; Farneth, W. E.; Wang, Y. Crystal Structure and Optical Properties of Cd32S14(SC6H5)36. DMF4, a Cluster with a 15 Angstrom CdS Core. *Science* **1993**, *259* (5100), 1426–1428. https://doi.org/10.1126/science.259.5100.1426.

(50) Kwon, S. G.; Piao, Y.; Park, J.; Angappane, S.; Jo, Y.; Hwang, N.-M.; Park, J.-G.; Hyeon, T. Kinetics of Monodisperse Iron Oxide Nanocrystal Formation by "Heating-Up" Process. *J. Am. Chem. Soc.* **2007**, *129* (41), 12571–12584. https://doi.org/10.1021/ja074633q.

(51) Williams, J. V.; Kotov, N. A.; Savage, P. E. A Rapid Hot-Injection Method for the Improved Hydrothermal Synthesis of CdSe Nanoparticles. *Ind. Eng. Chem. Res.* **2009**, *48* (9), 4316–4321. https://doi.org/10.1021/ie8007067.

(52) Sharma, P.; Pfromm, P. H.; Liu, B.; Chikan, V. Facile One-Pot Synthesis of γ-Fe_2O_3 Nanoparticles by Inductive Heating. *Mater. Adv.* **2021**, 10.1039.D1MA00280E. https://doi.org/10.1039/D1MA00280E.

(53) Razgoniaeva, N.; Acharya, A.; Sharma, N.; Adhikari, P.; Shaughnessy, M.; Moroz, P.; Khon, D.; Zamkov, M. Measuring the Time-Dependent Monomer Concentration during the Hot-Injection Synthesis of Colloidal Nanocrystals. *Chem. Mater.* **2015**, *27* (17), 6102–6108. https://doi.org/10.1021/acs.chemmater.5b02676.

(54) Enright, M. J.; Ritchhart, A.; Cossairt, B. M. Nucleation and Growth of Colloidal Semiconductor Nanoparticles. In *Encyclopedia of Inorganic and Bioinorganic Chemistry*; American Cancer Society, 2020; pp 1–11. https://doi.org/10.1002/9781119951438.eibc2723.

(55) Zacharaki, E.; Kalyva, M.; Fjellvåg, H.; Sjåstad, A. O. Burst Nucleation by Hot Injection for Size Controlled Synthesis of ε-Cobalt Nanoparticles. *Chem. Cent. J.* **2016**, *10*, 10. https://doi.org/10.1186/s13065-016-0156-1.

(56) van Embden, J.; Sader, J. E.; Davidson, M.; Mulvaney, P. Evolution of Colloidal Nanocrystals: Theory and Modeling of Their Nucleation and Growth. *J. Phys. Chem. C* **2009**, *113* (37), 16342–16355. https://doi.org/10.1021/jp9027673.

(57) Thanh, N. T. K.; Maclean, N.; Mahiddine, S. Mechanisms of Nucleation and Growth of Nanoparticles in Solution. *Chem. Rev.* **2014**, *114* (15), 7610–7630. https://doi.org/10.1021/cr400544s.

(58) Mer, V. K. L. Nucleation in Phase Transitions. **1952**, *44* (6), 8.

(59) LaMer, V. K.; Dinegar, R. H. Theory, Production and Mechanism of Formation of Monodispersed Hydrosols. *J. Am. Chem. Soc.* **1950**, *72* (11), 4847–4854. https://doi.org/10.1021/ja01167a001.

(60) Dunne, P. W.; Munn, A. S.; Starkey, C. L.; Huddle, T. A.; Lester, E. H. Continuous-Flow Hydrothermal Synthesis for the Production of Inorganic Nanomaterials. *Philos. Trans. R. Soc. Math. Phys. Eng. Sci.* **2015**, *373* (2057), 20150015. https://doi.org/10.1098/rsta.2015.0015.

(61) Karthika, S.; Radhakrishnan, T. K.; Kalaichelvi, P. A Review of Classical and Nonclassical Nucleation Theories. *Cryst. Growth Des.* **2016**, *16* (11), 6663–6681. https://doi.org/10.1021/acs.cgd.6b00794.
(62) Sugimoto, T. Preparation of Monodispersed Colloidal Particles. *Adv. Colloid Interface Sci.* **1987**, *28*, 65–108. https://doi.org/10.1016/0001-8686(87)80009-X.
(63) Luo, H. UNDERSTANDING AND CONTROLLING DEFECTS IN QUANTUM CONFINED SEMICONDUCTOR SYSTEMS. **2016**, 128.
(64) Kulpa-Greszta, M.; Tomaszewska, A.; Dziedzic, A.; Pązik, R. Rapid Hot-Injection as a Tool for Control of Magnetic Nanoparticle Size and Morphology. *RSC Adv.* **2021**, *11* (34), 20708–20719. https://doi.org/10.1039/D1RA02977K.
(65) Luo, H.; Kebede, B. A.; McLaurin, E. J.; Chikan, V. Rapid Induction and Microwave Heat-Up Syntheses of CdSe Quantum Dots. *ACS Omega* **2018**, *3* (5), 5399–5405. https://doi.org/10.1021/acsomega.8b00096.
(66) Li, W. Connecting Thermodynamics and Kinetics of Ligand Controlled Colloidal Pd Nanoparticle Synthesis. 298.
(67) Hyeon, T. Chemical Synthesis of Magnetic Nanoparticles. *Chem. Commun.* **2003**, No. 8, 927–934. https://doi.org/10.1039/B207789B.
(68) Best Research-Cell Efficiency Chart https://www.nrel.gov/pv/cell-efficiency.html (accessed 2021 -10 -13).
(69) Ruddy, D. A.; Johnson, J. C.; Smith, E. R.; Neale, N. R. Size and Bandgap Control in the Solution-Phase Synthesis of Near-Infrared-Emitting Germanium Nanocrystals. *ACS Nano* **2010**, *4* (12), 7459–7466. https://doi.org/10.1021/nn102728u.
(70) Muthuswamy, E.; Iskandar, A. S.; Amador, M. M.; Kauzlarich, S. M. Facile Synthesis of Germanium Nanoparticles with Size Control: Microwave *versus* Conventional Heating. *Chem. Mater.* **2013**, *25* (8), 1416–1422. https://doi.org/10.1021/cm302229b.
(71) ACFAA5C.Pdf.
(72) Induction Heating : Circuit Diagram, Working and Applications https://www.elprocus.com/induction-heating-principle-and-its-applications/ (accessed 2021 -03 -24).
(73) Hysteresis - Definition, Meaning, Hysteresis Loop, Loss, Curve https://byjus.com/jee/hysteresis/ (accessed 2021 -10 -12).
(74) Brandon. What Is Magnetic Hysteresis and Why Is It Important? *Materials Science & Engineering Student*.
(75) Induction Heating: What Is It & How Does It Work? | RDO Induction L.L.C. https://rdoinduction.com/fundamentals-of-induction-heating.html (accessed 2021 -10 -12).
(76) CEIA_InductionHeatingPrinciples_FC040K0068v1uk.Pdf.
(77) Skin Effect. *Wikipedia*; 2021.
(78) He, B.; Xu, G.; Zhou, M.; Yuan, Q. Effect of Oxidation Temperature on the Oxidation Process of Silicon-Containing Steel. *Metals* **2016**, *6* (6), 137. https://doi.org/10.3390/met6060137.
(79) Ge, S.; Shi, X.; Sun, K.; Li, C.; Baker, J. R.; Banaszak Holl, M. M.; Orr, B. G. A Facile Hydrothermal Synthesis of Iron Oxide Nanoparticles with Tunable Magnetic Properties. *J. Phys. Chem. C Nanomater. Interfaces* **2009**, *113* (31), 13593–13599. https://doi.org/10.1021/jp902953t.

(80) Mourdikoudis, S.; Liz-Marzán, L. M. Oleylamine in Nanoparticle Synthesis. *Chem. Mater.* **2013**, *25* (9), 1465–1476. https://doi.org/10.1021/cm4000476.

(81) Teja, A. S.; Koh, P.-Y. Synthesis, Properties, and Applications of Magnetic Iron Oxide Nanoparticles. *Prog. Cryst. Growth Charact. Mater.* **2009**, *55* (1), 22–45. https://doi.org/10.1016/j.pcrysgrow.2008.08.003.

(82) Ali, A.; Zafar, H.; Zia, M.; ul Haq, I.; Phull, A. R.; Ali, J. S.; Hussain, A. Synthesis, Characterization, Applications, and Challenges of Iron Oxide Nanoparticles. *Nanotechnol. Sci. Appl.* **2016**, *9*, 49–67. https://doi.org/10.2147/NSA.S99986.

(83) Park, J.; An, K.; Hwang, Y.; Park, J.-G.; Noh, H.-J.; Kim, J.-Y.; Park, J.-H.; Hwang, N.-M.; Hyeon, T. Ultra-Large-Scale Syntheses of Monodisperse Nanocrystals. *Nat. Mater.* **2004**, *3* (12), 891–895. https://doi.org/10.1038/nmat1251.

(84) Vidal-Vidal, J.; Rivas, J.; López-Quintela, M. A. Synthesis of Monodisperse Maghemite Nanoparticles by the Microemulsion Method. *Colloids Surf. Physicochem. Eng. Asp.* **2006**, *288* (1), 44–51. https://doi.org/10.1016/j.colsurfa.2006.04.027.

(85) Hyeon, T.; Lee, S. S.; Park, J.; Chung, Y.; Na, H. B. Synthesis of Highly Crystalline and Monodisperse Maghemite Nanocrystallites without a Size-Selection Process. *J. Am. Chem. Soc.* **2001**, *123* (51), 12798–12801. https://doi.org/10.1021/ja016812s.

(86) Aslam, M.; Schultz, E. A.; Sun, T.; Meade, T.; Dravid, V. P. Synthesis of Amine-Stabilized Aqueous Colloidal Iron Oxide Nanoparticles. *Cryst. Growth Des.* **2007**, *7* (3), 471–475. https://doi.org/10.1021/cg060656p.

(87) Gupta, A. K.; Gupta, M. Synthesis and Surface Engineering of Iron Oxide Nanoparticles for Biomedical Applications. *Biomaterials* **2005**, *26* (18), 3995–4021. https://doi.org/10.1016/j.biomaterials.2004.10.012.

(88) Peng, S.; Wang, C.; Xie, J.; Sun, S. Synthesis and Stabilization of Monodisperse Fe Nanoparticles. *J. Am. Chem. Soc.* **2006**, *128* (33), 10676–10677. https://doi.org/10.1021/ja063969h.

(89) Wu, W.; Wu, Z.; Yu, T.; Jiang, C.; Kim, W.-S. Recent Progress on Magnetic Iron Oxide Nanoparticles: Synthesis, Surface Functional Strategies and Biomedical Applications. *Sci. Technol. Adv. Mater.* **2015**, *16* (2). https://doi.org/10.1088/1468-6996/16/2/023501.

(90) Lam, U. T.; Mammucari, R.; Suzuki, K.; Foster, N. R. Processing of Iron Oxide Nanoparticles by Supercritical Fluids. *Ind. Eng. Chem. Res.* **2008**, *47* (3), 599–614. https://doi.org/10.1021/ie070494+.

(91) Perez De Berti, I.; Cagnoli, M.; Pecchi, G.; L Alessandrini, J.; Stewart, S.; Bengoa, F.; Marchetti, S. Alternative Low-Cost Approach to the Synthesis of Magnetic Iron Oxide Nanoparticles by Thermal Decomposition of Organic Precursors. *Nanotechnology* **2013**, *24*, 175601. https://doi.org/10.1088/0957-4484/24/17/175601.

(92) Lu, A.-H.; Salabas, E. L.; Schüth, F. Magnetic Nanoparticles: Synthesis, Protection, Functionalization, and Application. *Angew. Chem. Int. Ed.* **2007**, *46* (8), 1222–1244. https://doi.org/10.1002/anie.200602866.

(93) van Embden, J.; Chesman, A. S. R.; Jasieniak, J. J. The Heat-Up Synthesis of Colloidal Nanocrystals. *Chem. Mater.* **2015**, *27* (7), 2246–2285. https://doi.org/10.1021/cm5028964.

(94) Sun, S.; Zeng, H. Size-Controlled Synthesis of Magnetite Nanoparticles. *J. Am. Chem. Soc.* **2002**, *124* (28), 8204–8205. https://doi.org/10.1021/ja026501x.

(95) Das, B.; Kusz, J.; Reddy, V. R.; Zubko, M.; Bhattacharjee, A. Solventless Synthesis, Morphology, Structure and Magnetic Properties of Iron Oxide Nanoparticles. *Solid State Sci.* **2017**, *74*, 62–69. https://doi.org/10.1016/j.solidstatesciences.2017.10.010.

(96) Sharma, P. Colloidal Synthesis of Fe, Mn and Fe-Mn Alloy Nanoparticles by Rapid Inductive Heating Technique; AMER CHEMICAL SOC, 2018; Vol. 255.

(97) Laurent, S.; Forge, D.; Port, M.; Roch, A.; Robic, C.; Vander Elst, L.; Muller, R. N. Magnetic Iron Oxide Nanoparticles: Synthesis, Stabilization, Vectorization, Physicochemical Characterizations, and Biological Applications. *Chem. Rev.* **2008**, *108* (6), 2064–2110. https://doi.org/10.1021/cr068445e.

(98) Greaves, C. A Powder Neutron Diffraction Investigation of Vacancy Ordering and Covalence in γ-Fe2O3. *J. Solid State Chem.* **1983**, *49* (3), 325–333. https://doi.org/10.1016/S0022-4596(83)80010-3.

(99) Grau-Crespo, R.; Al-Baitai, A. Y.; Saadoune, I.; De Leeuw, N. H. Vacancy Ordering and Electronic Structure of γ - Fe $_2$ O $_3$ (Maghemite): A Theoretical Investigation. *J. Phys. Condens. Matter* **2010**, *22* (25), 255401. https://doi.org/10.1088/0953-8984/22/25/255401.

(100) Finger, L. W.; Hazen, R. M. Crystal Structure and Isothermal Compression of Fe2O3, Cr2O3, and V2O3 to 50 Kbars. *J. Appl. Phys.* **1980**, *51* (10), 5362–5367. https://doi.org/10.1063/1.327451.

(101) Wu, W.; He, Q.; Jiang, C. Magnetic Iron Oxide Nanoparticles: Synthesis and Surface Functionalization Strategies. *Nanoscale Res. Lett.* **2008**, *3* (11), 397–415. https://doi.org/10.1007/s11671-008-9174-9.

(102) Tadic, M.; Panjan, M.; Tadic, B. V.; Lazovic, J.; Damnjanovic, V.; Kopani, M.; Kopanja, L. Magnetic Properties of Hematite (α − Fe2O3) Nanoparticles Synthesized by Sol-Gel Synthesis Method: The Influence of Particle Size and Particle Size Distribution. *J. Electr. Eng.* **2019**, *70* (7), 71–76. https://doi.org/10.2478/jee-2019-0044.

(103) Tadic, M.; Kralj, S.; Jagodic, M.; Hanzel, D.; Makovec, D. Magnetic Properties of Novel Superparamagnetic Iron Oxide Nanoclusters and Their Peculiarity under Annealing Treatment. *Appl. Surf. Sci.* **2014**, *322*, 255–264. https://doi.org/10.1016/j.apsusc.2014.09.181.

(104) Tadic, M.; Kralj, S.; Lalatonne, Y.; Motte, L. Iron Oxide Nanochains Coated with Silica: Synthesis, Surface Effects and Magnetic Properties. *Appl. Surf. Sci.* **2019**, *476*, 641–646. https://doi.org/10.1016/j.apsusc.2019.01.098.

(105) Tadic, M.; Trpkov, D.; Kopanja, L.; Vojnovic, S.; Panjan, M. Hydrothermal Synthesis of Hematite (α-Fe2O3) Nanoparticle Forms: Synthesis Conditions, Structure, Particle Shape Analysis, Cytotoxicity and Magnetic Properties. *J. Alloys Compd.* **2019**, *792*, 599–609. https://doi.org/10.1016/j.jallcom.2019.03.414.

(106) Tadic, M.; Kralj, S.; Kopanja, L. Synthesis, Particle Shape Characterization, Magnetic Properties and Surface Modification of Superparamagnetic Iron Oxide Nanochains. *Mater. Charact.* **2019**, *148*, 123–133. https://doi.org/10.1016/j.matchar.2018.12.014.

(107) Nemati, Z.; Alonso, J.; Khurshid, H.; Phan, M. H.; Srikanth, H. Core/Shell Iron/Iron Oxide Nanoparticles: Are They Promising for Magnetic Hyperthermia? *RSC Adv.* **2016**, *6* (45), 38697–38702. https://doi.org/10.1039/C6RA05064F.

(108) Rath, C.; Mishra, N. C.; Anand, S.; Das, R. P.; Sahu, K. K.; Upadhyay, C.; Verma, H. C. Appearance of Superparamagnetism on Heating Nanosize Mn0.65Zn0.35Fe2O4. *Appl. Phys. Lett.* **2000**, *76* (4), 475–477. https://doi.org/10.1063/1.125792.

(109) Berkowitz, A. E.; Kodama, R. H.; Makhlouf, S. A.; Parker, F. T.; Spada, F. E.; McNiff, E. J.; Foner, S. Anomalous Properties of Magnetic Nanoparticles. *J. Magn. Magn. Mater.* **1999**, *196–197*, 591–594. https://doi.org/10.1016/S0304-8853(98)00845-2.

(110) Pecharromán, C.; González-Carreño, T.; Iglesias, J. E. The Infrared Dielectric Properties of Maghemite, γ-Fe2O3, from Reflectance Measurement on Pressed Powders. *Phys. Chem. Miner.* **1995**, *22* (1), 21–29. https://doi.org/10.1007/BF00202677.

(111) Woodward, P. M.; Suard, E.; Karen, P. Structural Tuning of Charge, Orbital, and Spin Ordering in Double-Cell Perovskite Series between NdBaFe2O5 and HoBaFe2O5. 11.

(112) Zhong, L.-S.; Hu, J.-S.; Liang, H.-P.; Cao, A.-M.; Song, W.-G.; Wan, L.-J. Self-Assembled 3D Flowerlike Iron Oxide Nanostructures and Their Application in Water Treatment. *Adv. Mater.* **2006**, *18* (18), 2426–2431. https://doi.org/10.1002/adma.200600504.

(113) Two-in-One Strategy for Effective Enrichment of Phosphopeptides Using Magnetic Mesoporous γ-Fe2O3 Nanocrystal Clusters | ACS Applied Materials & Interfaces https://pubs.acs.org/doi/abs/10.1021/am3019806 (accessed 2020 -11 -10).

(114) Kamali, S.; Chen, C. J.; Bates, B.; Johnson, C. E.; Chiang, R. K. Size-Dependent Magnetic Properties of γ -Fe $_2$ O $_3$ Nanocrystallites. *J. Phys. Condens. Matter* **2020**, *32* (1), 015302. https://doi.org/10.1088/1361-648X/ab41be.

(115) Zhang, B.; Wang, Q.; Zhang, G.; Liao, S.; Wang, Z.; Li, G. Preparation of Iron Nanoparticles from Iron Pentacarbonyl Using an Atmospheric Microwave Plasma. *Plasma Sci. Technol.* **2015**, *17* (10), 876–880. https://doi.org/10.1088/1009-0630/17/10/11.

(116) Naik, R.; Senaratne, U.; Powell, N.; Buc, E. C.; Tsoi, G. M.; Naik, V. M.; Vaishnava, P. P.; Wenger, L. E. Magnetic Properties of Nanosized Iron Oxide Particles Precipitated in Alginate Hydrogels. *J. Appl. Phys.* **2005**, *97* (10), 10J313. https://doi.org/10.1063/1.1853016.

(117) Jing, Z.; Wu, S. Synthesis, Characterization and Magnetic Properties of γ-Fe2O3 Nanoparticles via a Non-Aqueous Medium. *J. Solid State Chem.* **2004**, *177* (4), 1213–1218. https://doi.org/10.1016/j.jssc.2003.10.034.

(118) Suresh, S.; Karthikeyan, S.; Jayamoorthy, K. Effect of Bulk and Nano-Fe2O3 Particles on Peanut Plant Leaves Studied by Fourier Transform Infrared Spectral Studies. *J. Adv. Res.* **2016**, *7* (5), 739–747. https://doi.org/10.1016/j.jare.2015.10.002.

(119) Marasini, R.; Rayamajhi, S.; Moreno-Sanchez, A.; Aryal, S. Iron(Iii) Chelated Paramagnetic Polymeric Nanoparticle Formulation as a next-Generation T 1 -Weighted MRI Contrast Agent. *RSC Adv.* **2021**, *11* (51), 32216–32226. https://doi.org/10.1039/D1RA05544E.

(120) Wu, K. T.; Yao, Y. D.; Wang, C. R. C.; Chen, P. F.; Yeh, E. T. Magnetic Field Induced Optical Transmission Study in an Iron Nanoparticle Ferrofluid. *J. Appl. Phys.* **1999**, *85* (8), 5959–5961. https://doi.org/10.1063/1.370004.

(121) Marasini, R.; Nguyen, T. D. T.; Aryal, S. Integration of Gadolinium in Nanostructure for Contrast Enhanced-Magnetic Resonance Imaging. *WIREs Nanomedicine Nanobiotechnology* **2020**, *12* (1), e1580. https://doi.org/10.1002/wnan.1580.

(122) Huang, K.-C.; Ehrman, S. H. Synthesis of Iron Nanoparticles via Chemical Reduction with Palladium Ion Seeds. *Langmuir* **2007**, *23* (3), 1419–1426. https://doi.org/10.1021/la0618364.

(123) Pankhurst, Q. A.; Connolly, J.; Jones, S. K.; Dobson, J. Applications of Magnetic Nanoparticles in Biomedicine. *J. Phys. Appl. Phys.* **2003**, *36* (13), R167–R181. https://doi.org/10.1088/0022-3727/36/13/201.

(124) Li, F.; Vipulanandan, C.; Mohanty, K. K. Microemulsion and Solution Approaches to Nanoparticle Iron Production for Degradation of Trichloroethylene. *Colloids Surf. Physicochem. Eng. Asp.* **2003**, *223* (1), 103–112. https://doi.org/10.1016/S0927-7757(03)00187-0.

(125) Zhang, W. Nanoscale Iron Particles for Environmental Remediation: An Overview. *J. Nanoparticle Res.* **2003**, *5* (3), 323–332. https://doi.org/10.1023/A:1025520116015.

(126) Li, X.; Zhang, W. Iron Nanoparticles: The Core−Shell Structure and Unique Properties for Ni(II) Sequestration. *Langmuir* **2006**, *22* (10), 4638–4642. https://doi.org/10.1021/la060057k.

(127) Marasini, R.; Thanh Nguyen, T. D.; Rayamajhi, S.; Aryal, S. Synthesis and Characterization of a Tumor-Seeking LyP-1 Peptide Integrated Lipid–Polymer Composite Nanoparticle. *Mater. Adv.* **2020**, *1* (3), 469–480. https://doi.org/10.1039/D0MA00203H.

(128) Teo, K. B. K.; Chhowalla, M.; Amaratunga, G. a. J.; Milne, W. I.; Hasko, D. G.; Pirio, G.; Legagneux, P.; Wyczisk, F.; Pribat, D. Uniform Patterned Growth of Carbon Nanotubes without Surface Carbon. *Appl. Phys. Lett.* **2001**, *79* (10), 1534–1536. https://doi.org/10.1063/1.1400085.

(129) Cho, Y.-S.; Choi, G.-S.; Hong, S.-Y.; Kim, D. Carbon Nanotube Synthesis Using a Magnetic Fluid via Thermal Chemical Vapor Deposition. *J. Cryst. Growth* **2002**, *243* (1), 224–229. https://doi.org/10.1016/S0022-0248(02)01496-3.

(130) Huber, D. L. Synthesis, Properties, and Applications of Iron Nanoparticles. *Small* **2005**, *1* (5), 482–501. https://doi.org/10.1002/smll.200500006.

(131) Chen, M.; Yamamuro, S.; Farrell, D.; Majetich, S. A. Gold-Coated Iron Nanoparticles for Biomedical Applications. *J. Appl. Phys.* **2003**, *93* (10), 7551–7553. https://doi.org/10.1063/1.1555312.

(132) Farrell, D.; Majetich, S. A.; Wilcoxon, J. P. Preparation and Characterization of Monodisperse Fe Nanoparticles. *J. Phys. Chem. B* **2003**, *107* (40), 11022–11030. https://doi.org/10.1021/jp0351831.

(133) Huber, D. L.; Venturini, E. L.; Martin, J. E.; Provencio, P. P.; Patel, R. J. Synthesis of Highly Magnetic Iron Nanoparticles Suitable for Field Structuring Using a β-Diketone Surfactant. *J. Magn. Magn. Mater.* **2004**, *278* (3), 311–316. https://doi.org/10.1016/j.jmmm.2003.12.1317.

(134) Synthesis of Highly Crystalline and Monodisperse Maghemite Nanocrystallites without a Size-Selection Process | Journal of the American Chemical Society https://pubs.acs.org/doi/10.1021/ja016812s (accessed 2021 -09 -30).

(135) Direct Synthesis of Highly Crystalline and Monodisperse Manganese Ferrite Nanocrystals | The Journal of Physical Chemistry B https://pubs.acs.org/doi/10.1021/jp049041y (accessed 2021 -09 -30).

(136) Nikitenko, S. I.; Koltypin, Y.; Markovich, V.; Rozenberg, E.; Gorodetsky, G.; Gedanken, A. Synthesis of Air-Stable Iron-Iron Carbide Nanocrystalline Particles Showing Very High Saturation Magnetization. *IEEE Trans. Magn.* **2002**, *38* (5), 2592–2594. https://doi.org/10.1109/TMAG.2002.803222.

(137) Berkowitz, A. E.; Takano, K. Exchange Anisotropy — a Review. *J. Magn. Magn. Mater.* **1999**, *200* (1), 552–570. https://doi.org/10.1016/S0304-8853(99)00453-9.

(138) Smolensky, E. D.; Park, H.-Y. E.; Zhou, Y.; Rolla, G. A.; Marjańska, M.; Botta, M.; Pierre, V. C. Scaling Laws at the Nano Size: The Effect of Particle Size and Shape on the Magnetism and Relaxivity of Iron Oxide Nanoparticle Contrast Agents. *J. Mater. Chem. B Mater. Biol. Med.* **2013**, *1* (22), 2818–2828. https://doi.org/10.1039/C3TB00369H.

(139) Pillarisetty, R. Academic and Industry Research Progress in Germanium Nanodevices. *Nature* **2011**, *479* (7373), 324–328. https://doi.org/10.1038/nature10678.

(140) Nataraj, L.; Xu, F.; Cloutier, S. G. Direct-Bandgap Luminescence at Room-Temperature from Highly-Strained Germanium Nanocrystals. *Opt. Express* **2010**, *18* (7), 7085–7091. https://doi.org/10.1364/OE.18.007085.

(141) Kamata, Y. High-k/Ge MOSFETs for Future Nanoelectronics. *Mater. Today* **2008**, *11* (1), 30–38. https://doi.org/10.1016/S1369-7021(07)70350-4.

(142) Ii, D. D. V.; Schaak, R. E. Synthesis, Properties and Applications of Colloidal Germanium and Germanium-Based Nanomaterials. *Chem. Soc. Rev.* **2013**, *42* (7), 2861–2879. https://doi.org/10.1039/C2CS35364D.

(143) Vörös, M.; Wippermann, S.; Somogyi, B.; Gali, A.; Rocca, D.; Galli, G.; T. Zimanyi, G. Germanium Nanoparticles with Non-Diamond Core Structures for Solar Energy Conversion. *J. Mater. Chem. A* **2014**, *2* (25), 9820–9827. https://doi.org/10.1039/C4TA01543F.

(144) Fan, J.; Chu, P. K. Group IV Nanoparticles: Synthesis, Properties, and Biological Applications. *Small* **2010**, *6* (19), 2080–2098. https://doi.org/10.1002/smll.201000543.

(145) Cardoso, J.; Marom, S.; Mayer, J.; Modi, R.; Podestà, A.; Xie, X.; Huis, M. A. van; Vece, M. D. Germanium Quantum Dot Grätzel-Type Solar Cell. *Phys. Status Solidi A* **2018**, *215* (24), 1800570. https://doi.org/10.1002/pssa.201800570.

(146) Lee, D. C.; Pietryga, J. M.; Robel, I.; Werder, D. J.; Schaller, R. D.; Klimov, V. I. Colloidal Synthesis of Infrared-Emitting Germanium Nanocrystals. *J. Am. Chem. Soc.* **2009**, *131* (10), 3436–3437. https://doi.org/10.1021/ja809218s.

(147) Tanke, R. S.; Kauzlarich, S. M.; Patten, T. E.; Pettigrew, K. A.; Murphy, D. L.; Thompson, M. E.; Lee, H. W. H. Synthesis of Germanium Nanoclusters with Irreversibly Attached Functional Groups: Acetals, Alcohols, Esters, and Polymers. *Chem. Mater.* **2003**, *15* (8), 1682–1689. https://doi.org/10.1021/cm021778h.

(148) Henderson, E. J.; Hessel, C. M.; Veinot, J. G. C. Synthesis and Photoluminescent Properties of Size-Controlled Germanium Nanocrystals from Phenyl Trichlorogermane-Derived Polymers. *J. Am. Chem. Soc.* **2008**, *130* (11), 3624–3632. https://doi.org/10.1021/ja710286a.

(149) Dai, F.; Zai, J.; Yi, R.; Gordin, M. L.; Sohn, H.; Chen, S.; Wang, D. Bottom-up Synthesis of High Surface Area Mesoporous Crystalline Silicon and Evaluation of Its Hydrogen Evolution Performance. *Nat. Commun.* **2014**, *5* (1), 3605. https://doi.org/10.1038/ncomms4605.

(150) Chiu, H. W.; Chervin, C. N.; Kauzlarich, S. M. Phase Changes in Ge Nanoparticles. *Chem. Mater.* **2005**, *17* (19), 4858–4864. https://doi.org/10.1021/cm050674e.

(151) Chiu, H. W.; Kauzlarich, S. M. Investigation of Reaction Conditions for Optimal Germanium Nanoparticle Production by a Simple Reduction Route. *Chem. Mater.* **2006**, *18* (4), 1023–1028. https://doi.org/10.1021/cm0521222.

(152) Lee, H.; Kim, M. G.; Choi, C. H.; Sun, Y.-K.; Yoon, C. S.; Cho, J. Surface-Stabilized Amorphous Germanium Nanoparticles for Lithium-Storage Material. *J. Phys. Chem. B* **2005**, *109* (44), 20719–20723. https://doi.org/10.1021/jp052620y.

(153) Taylor, B. R.; Kauzlarich, S. M.; Lee, H. W. H.; Delgado, G. R. Solution Synthesis of Germanium Nanocrystals Demonstrating Quantum Confinement. *Chem. Mater.* **1998**, *10* (1), 22–24. https://doi.org/10.1021/cm970576w.

(154) Prabakar, S.; Shiohara, A.; Hanada, S.; Fujioka, K.; Yamamoto, K.; Tilley, R. D. Size Controlled Synthesis of Germanium Nanocrystals by Hydride Reducing Agents and Their Biological Applications. *Chem. Mater.* **2010**, *22* (2), 482–486. https://doi.org/10.1021/cm9030599.

(155) Yang, C.-S.; Kauzlarich, S. M.; Wang, Y. C. Synthesis and Characterization of Germanium/Si−Alkyl and Germanium/Silica Core−Shell Quantum Dots. *Chem. Mater.* **1999**, *11* (12), 3666–3670. https://doi.org/10.1021/cm9905949.

(156) Sharma, Pratikshya. Synthesis of Germanium Nanoparticles by Rapid Inductive Heating; AMER CHEMICAL SOC, 2019; Vol. 257.

(157) Holliger, Noah, N. Developing Effective Catalysts: Sustainable Fossil-Free Ammonia Synthesis at Atmospheric Pressure; AMER CHEMICAL SOC, 2019; Vol. 257.

(158) Wilcoxon, J. P.; Samara, G. A. Strong Quantum-Size Effects in a Layered Semiconductor: MoS 2 Nanoclusters. *Phys. Rev. B* **1995**, *51* (11), 7299–7302. https://doi.org/10.1103/PhysRevB.51.7299.

(159) Fok, E.; Shih, M.; Meldrum, A.; C. Veinot, J. G. Preparation of Alkyl-Surface Functionalized Germanium Quantum Dots via Thermally Initiated Hydrogermylation. *Chem. Commun.* **2004**, *0* (4), 386–387. https://doi.org/10.1039/B314887D.

(160) Kanetkar, V. R.; Zope, D. D.; Subrahmanyam, Y. V. V. Acetonitrile: A Convenient Reagent for the One-Pot Preparation of Perfumery Nitriles from Aldehydes. *ChemInform* **2005**, *36* (44). https://doi.org/10.1002/chin.200544103.

(161) Chen, M.; Feng, Y.-G.; Wang, X.; Li, T.-C.; Zhang, J.-Y.; Qian, D.-J. Silver Nanoparticles Capped by Oleylamine: Formation, Growth, and Self-Organization. *Langmuir ACS J. Surf. Colloids* **2007**, *23* (10), 5296–5304. https://doi.org/10.1021/la700553d.

(162) Vaughn, D. D.; Bondi, J. F.; Schaak, R. E. Colloidal Synthesis of Air-Stable Crystalline Germanium Nanoparticles with Tunable Sizes and Shapes. *Chem. Mater.* **2010**, *22* (22), 6103–6108. https://doi.org/10.1021/cm1015965.

(163) Xue, D.-J.; Wang, J.-J.; Wang, Y.-Q.; Xin, S.; Guo, Y.-G.; Wan, L.-J. Facile Synthesis of Germanium Nanocrystals and Their Application in Organic–Inorganic Hybrid Photodetectors. *Adv. Mater.* **2011**, *23* (32), 3704–3707. https://doi.org/10.1002/adma.201101436.

(164) Tuinenga, C.; Jasinski, J.; Iwamoto, T.; Chikan, V. In Situ Observation of Heterogeneous Growth of CdSe Quantum Dots: Effect of Indium Doping on the Growth Kinetics. *ACS Nano* **2008**, *2* (7), 1411–1421. https://doi.org/10.1021/nn700377q.

(165) El-Sayed, M. A. Small Is Different: Shape-, Size-, and Composition-Dependent Properties of Some Colloidal Semiconductor Nanocrystals. *Acc. Chem. Res.* **2004**, *37* (5), 326–333. https://doi.org/10.1021/ar020204f.

(166) Wood, D. M.; Ashcroft, N. W. Quantum Size Effects in the Optical Properties of Small Metallic Particles. *Phys. Rev. B* **1982**, *25* (10), 6255–6274. https://doi.org/10.1103/PhysRevB.25.6255.

(167) Cao, J.; Mao, Q.; Shi, L.; Qian, Y. Fabrication of γ-MnO2/α-MnO2 Hollow Core/Shell Structures and Their Application to Water Treatment. *J. Mater. Chem.* **2011**, *21* (40), 16210–16215. https://doi.org/10.1039/C1JM10862J.

(168) Yan, D.; Cheng, S.; Zhuo, R. F.; Chen, J. T.; Feng, J. J.; Feng, H. T.; Li, H. J.; Wu, Z. G.; Wang, J.; Yan, P. X. Nanoparticles and 3D Sponge-like Porous Networks of Manganese Oxides and Their Microwave Absorption Properties. *Nanotechnology* **2009**, *20* (10), 105706. https://doi.org/10.1088/0957-4484/20/10/105706.

(169) Zhang, X.; Xing, Z.; Yu, Y.; Li, Q.; Tang, K.; Huang, T.; Zhu, Y.; Qian, Y.; Chen, D. Synthesis of Mn3O4 Nanowires and Their Transformation to LiMn2O4 Polyhedrons, Application of LiMn2O4 as a Cathode in a Lithium-Ion Battery. *CrystEngComm* **2012**, *14* (4), 1485–1489. https://doi.org/10.1039/C1CE06289A.

(170) Ma, R.; Bando, Y.; Zhang, L.; Sasaki, T. Layered MnO2 Nanobelts: Hydrothermal Synthesis and Electrochemical Measurements. *Adv. Mater.* **2004**, *16* (11), 918–922. https://doi.org/10.1002/adma.200306592.

(171) Wu, Z.; Jiang, B.; Liu, Y.; Wang, H.; Jin, R. DRIFT Study of Manganese/Titania-Based Catalysts for Low-Temperature Selective Catalytic Reduction of NO with NH3. *Environ. Sci. Technol.* **2007**, *41* (16), 5812–5817. https://doi.org/10.1021/es0700350.

(172) Bentrup, U.; Brückner, A.; Richter, M.; Fricke, R. NOx Adsorption on MnO2/NaY Composite: An in Situ FTIR and EPR Study. *Appl. Catal. B Environ.* **2001**, *32* (4), 229–241. https://doi.org/10.1016/S0926-3373(01)00142-4.

(173) Cheng, F.; Zhao, J.; Song, W.; Li, C.; Ma, H.; Chen, J.; Shen, P. Facile Controlled Synthesis of MnO2 Nanostructures of Novel Shapes and Their Application in Batteries. *Inorg. Chem.* **2006**, *45* (5), 2038–2044. https://doi.org/10.1021/ic051715b.

(174) Qi, G.; Yang, R. T. A Superior Catalyst for Low-Temperature NO Reduction with NH3. *Chem. Commun.* **2003**, No. 7, 848–849. https://doi.org/10.1039/B212725C.

(175) Long, R. Q.; Yang, R. T.; Chang, R. Low Temperature Selective Catalytic Reduction (SCR) of NO with NH3 over Fe–Mn Based Catalysts. *Chem. Commun.* **2002**, No. 5, 452–453. https://doi.org/10.1039/B111382H.

(176) Xiao, W.; Wang, D.; Lou, X. W. Shape-Controlled Synthesis of MnO2 Nanostructures with Enhanced Electrocatalytic Activity for Oxygen Reduction. *J. Phys. Chem. C* **2010**, *114* (3), 1694–1700. https://doi.org/10.1021/jp909386d.

(177) Wang, X.; Li, Y. Synthesis and Formation Mechanism of Manganese Dioxide Nanowires/Nanorods. *Chem. – Eur. J.* **2003**, *9* (1), 300–306. https://doi.org/10.1002/chem.200390024.

(178) Michalsky, R.; Peterson, B. A.; Pfromm, P. H. Rapid Synthesis of Nanocrystalline Magnesium Chromite and Ferrite Ceramics with Concentrated Sunlight. *Thermochim. Acta* **2014**, *582*, 10–16. https://doi.org/10.1016/j.tca.2014.02.018.

(179) Michalsky, R.; Pfromm, P. H. Thermodynamics of Metal Reactants for Ammonia Synthesis from Steam, Nitrogen and Biomass at Atmospheric Pressure. *AIChE J.* **2012**, *58* (10), 3203–3213. https://doi.org/10.1002/aic.13717.

(180) Michalsky, R.; Avram, A. M.; Peterson, B. A.; Pfromm, P. H.; Peterson, A. A. Chemical Looping of Metal Nitride Catalysts: Low-Pressure Ammonia Synthesis for Energy Storage. *Chem. Sci.* **2015**, *6* (7), 3965–3974. https://doi.org/10.1039/C5SC00789E.

(181) Michalsky, R.; Pfromm, P. H. An Ionicity Rationale to Design Solid Phase Metal Nitride Reactants for Solar Ammonia Production. *J. Phys. Chem. C* **2012**, *116* (44), 23243–23251. https://doi.org/10.1021/jp307382r.

(182) Michalsky, R.; Pfromm, P. H. Chromium as Reactant for Solar Thermochemical Synthesis of Ammonia from Steam, Nitrogen, and Biomass at Atmospheric Pressure. *Sol. Energy* **2011**, *85* (11), 2642–2654. https://doi.org/10.1016/j.solener.2011.08.005.

(183) Michalsky, R.; Parman, B. J.; Amanor-Boadu, V.; Pfromm, P. H. Solar Thermochemical Production of Ammonia from Water, Air and Sunlight: Thermodynamic and Economic Analyses. *Energy* **2012**, *42* (1), 251–260. https://doi.org/10.1016/j.energy.2012.03.062.

(184) Bondi, J. F.; Oyler, K. D.; Ke, X.; Schiffer, P.; Schaak, R. E. Chemical Synthesis of Air-Stable Manganese Nanoparticles. *J. Am. Chem. Soc.* **2009**, *131* (26), 9144–9145. https://doi.org/10.1021/ja901372q.

(185) Abdul-Razzaq, W.; Wu, M. Magnetic Properties of Ball-Milled Mn Nanoparticles. *Superlattices Microstruct.* **2001**, *29* (4), 273–279. https://doi.org/10.1006/spmi.2000.0970.

(186) Ward, M. B.; Brydson, R.; Cochrane, R. F. Mn Nanoparticles Produced by Inert Gas Condensation. *J. Phys. Conf. Ser.* **2006**, *26*, 296–299. https://doi.org/10.1088/1742-6596/26/1/071.

(187) Si, P. Z.; Brück, E.; Zhang, Z. D.; Tegus, O.; Zhang, W. S.; Buschow, K. H. J.; Klaasse, J. C. P. Structural and Magnetic Properties of Mn Nanoparticles Prepared by Arc-Discharge. *Mater. Res. Bull.* **2005**, *40* (1), 29–37. https://doi.org/10.1016/j.materresbull.2004.09.010.

(188) Gregg, K. A.; Perera, S. C.; Lawes, G.; Shinozaki, S.; Brock, S. L. Controlled Synthesis of MnP Nanorods: Effect of Shape Anisotropy on Magnetization. *Chem. Mater.* **2006**, *18* (4), 879–886. https://doi.org/10.1021/cm052080h.

(189) Ono, K.; Okuda, R.; Ishii, Y.; Kamimura, S.; Oshima, M. Synthesis of Ferromagnetic Mn−Pt Nanoparticles from Organometallic Precursors. *J. Phys. Chem. B* **2003**, *107* (9), 1941–1942. https://doi.org/10.1021/jp026898r.

(190) Lee, D. C.; Ghezelbash, A.; Stowell, C. A.; Korgel, B. A. Synthesis and Magnetic Properties of Colloidal MnPt3 Nanocrystals. *J. Phys. Chem. B* **2006**, *110* (42), 20906–20911. https://doi.org/10.1021/jp064050n.

Appendix A - Supporting information from Chapter 3

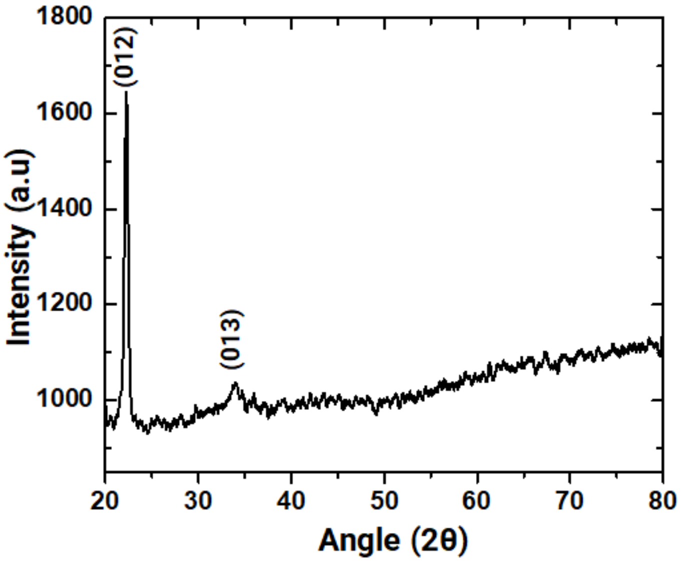

Figure 3.S1. PXRD of IONPs synthesized using 3.35 M $Fe(CO)_5$ and oleylamine at 5 s heating time.

Appendix B - Supporting information from Chapter 4

Size (nm)	Magnetization (emu/g)
7.4 ± 2.5	5
9.1 ±1.3	75
9.4 ±0.7	62
11.1 ±2.2	90

Table 4.S1. Table summarizing size and the magnetization of iron NPs.

Appendix C - Supporting information from Chapter 5

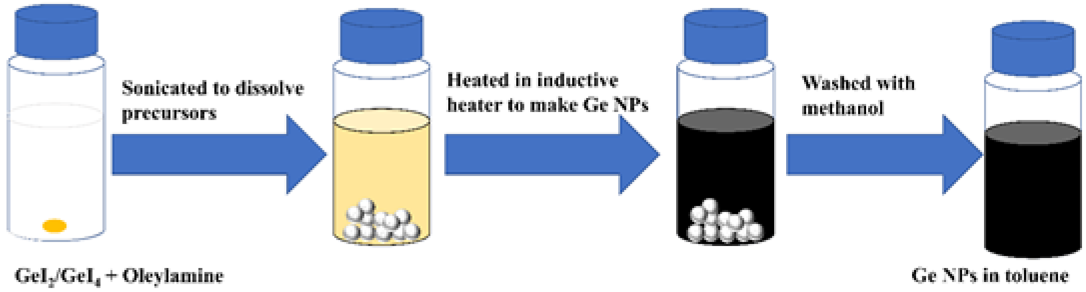

Figure 5.S1. Schematics showing steps of inductive heating assisted synthesis of Ge NPs

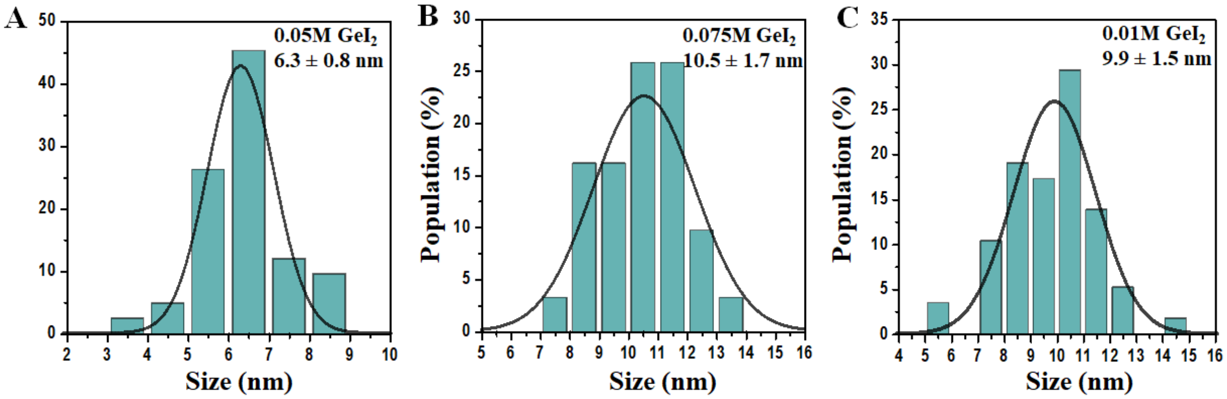

Figure 5.S2. Size distribution plots for Ge NPs given in **Figure 5.1.** (A) 0.05 M GeI_2, (B) 0.075 M GeI_2, (C) 0.1 M GeI_2

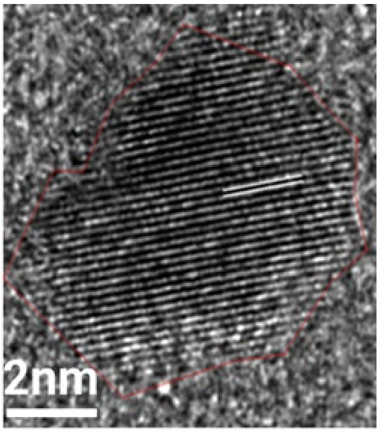

Figure 5.S3. HRTEM images of Ge NPs corresponding to **Figure 5.2 B** indicating 111 lattice planes of cubic Ge NPs.

Appendix D - Supporting information from Chapter 6

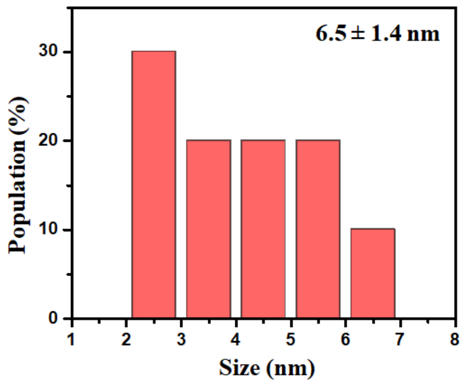

Figure 5.S1. Size distribution plot of MnO NPs corresponding to **Figure 6.1**.

Appendix E - List of publications

1. **Sharma P,** Holliger N*, Pfromm P, Liu B, Chikan V. Size controlled synthesis of iron and iron oxide nanoparticles by rapid inductive heating technique. ***ACS Omega,*** 2020, 5, 31, 19853–19860 **(Chapter 3 and Chapter 4)**

2. **Sharma P,** Chikan V. Facile one-pot synthesis of γ-Fe_2O_3 nanoparticles by inductive heating. ***Mater. Adv.****,* 2021,**2**, 5616-5621**(Chapter 3)**